Chapter 2
Sea Surface Microlayer

Abstract The top few millimeters of the ocean surface, where properties are most altered relative to deeper water, are often referred to as the sea surface microlayer. Physics, chemistry, and biology of the sea surface microlayer are the subject of this chapter. Very close to the air–sea interface, turbulent mixing is suppressed and molecular diffusion appears to dominate the vertical property transport. The viscous, thermal, and diffusive sublayers close to the ocean surface that exist as characteristic features of the air–sea momentum, heat, and mass transport are considered. Their dynamics are quite complex due to the presence of surface waves, capillary effects, penetrating solar radiation, rainfall, and surface films due to the presence of surfactants. The existing theories of the sea surface microlayer, numerical model parameterizations, available observations and new approaches, including computational fluid dynamics modeling and DNA analysis of the bacterial content of the sea surface microlayer, are critically analyzed in this chapter.

Keywords Sea surface microlayer • Viscous sublayer • Thermal sublayer • Diffusion sublayer • Neuston • Surfactant • Surface • Film • Slick • DNA analysis • SAR • Microscale wave breaking • Whitecapping • Coherent structures • Streaks • SST • Dimensional analysis • Renewal model • Renewal time • Cool skin • Solar radiation • Rain • Freshwater skin • Diurnal mixed layer • Diurnal thermocline • Gravity-capillary waves

2.1 Introduction

The microlayer is involved in the heat and momentum transfer between the ocean and atmosphere and plays a vital role in the uptake of greenhouse gases by the ocean. A striking variety of physical, biological, chemical, and photochemical interactions and feedbacks occur in the ocean surface microlayer. There is a widely held presumption that the microlayer is a highly efficient and selective micro-reactor, effectively concentrating and transforming materials brought to the interface from the atmosphere and oceans by physical processes (Liss and Duce 1997). These processes are very intriguing and potentially of great importance for remote sensing of sea surface temperature (SST) and salinity, climate change, and many other practical applications still waiting for their time to come.

A. Soloviev, R. Lukas, *The Near-Surface Layer of the Ocean,* Atmospheric and Oceanographic Sciences Library 48, DOI 10.1007/978-94-007-7621-0_2,

Direct measurement of the sea surface microlayer is still a challenge. As a result, surprisingly little experimental information exists on the structure of the sea surface microlayer. The majority of microlayer results have been obtained from laboratory studies.

The physics of the sea surface microlayer is related to fundamental properties of turbulent boundary layers, such as intermittency (Kline et al. 1967) and quasi-periodic repeating patterns of coherent motion (Robinson 1991). While in the bulk of the water, turbulence largely controls the transport, molecular diffusion takes over the transfer of momentum, heat, and mass from the upper ocean to the sea surface because the vertical component of turbulent velocity is suppressed close to the surface. Surface organic and inorganic films formed as a result of complex interplay between biological, chemical, and physical processes can interfere with air–sea interaction (for instance, by modifying properties of capillary-gravity waves) and affect the properties of molecular sublayers.

Under very high wind-speed conditions, the sea surface can be defined only in the topological sense; as a result, the viscous sublayers is replaced with a two-phase transition layer, which consists of air bubbles, spray droplets, and the overhang of plunging waves (Chap. 6)

As a first approximation, the thickness of the viscous, thermal, and diffusion molecular sublayers at the ocean surface, outside of whitecaps and white outs, can be linked to the Kolmogorov's (1942) internal length scale of turbulence,

$$\eta_\nu = (\nu^3 / \varepsilon)^{1/4}, \tag{2.1}$$

where ν is the molecular kinematic viscosity and ε is the dissipation rate of the turbulent kinetic energy. Similar length scales also exist for thermal and diffusive turbulent processes,

$$\eta_T = \mathrm{Pr}^{-1/2}(\nu^3 / \varepsilon)^{1/4} \tag{2.2}$$

and

$$\eta_D = Sc^{-1/2}(\nu^3 / \varepsilon)^{1/4} \tag{2.3}$$

where $\mathrm{Pr} = \nu / \kappa_T$ is the Prandtl number ($\mathrm{Pr} = 7.1$ for water at 20 °C), $Sc = \nu / \mu$ is the Schmidt number (Sc~10^3), κ_T is the molecular coefficient of kinematic thermal diffusivity, and μ is the molecular coefficient of kinematic molecular diffusivity. The latter equation is applicable to tracer gases, passive contaminants, or sea salts.

An instructive schematic diagram is shown in Fig. 2.1. The logarithmic scale ranges from the diameter of a molecule to the maximum depth of the world ocean emphasizing the top millimeter of the ocean. Molecular sublayers extend from the surface to typical depths of about 1,500 μm (viscous sublayer), 500 μm (thermal sublayer), and 50 μm (diffusion sublayer). There are also organic films on the sea surface, of natural or anthropogenic origin, starting from a few nanometers thickness.

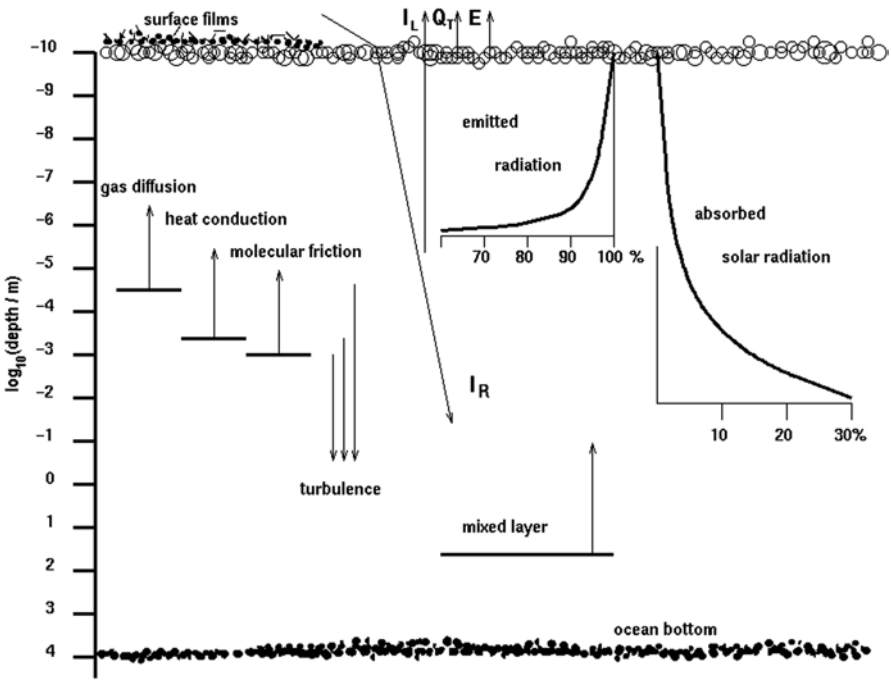

Fig. 2.1 Schematic representation of the vertical structure of physical processes related to the sea surface microlayer. (courtesy of Peter Schlüssel)

These are of course only nominal values. The thickness of molecular sublayers depends substantially on the air–sea interaction regime. In fact, the structure of the molecular sublayers are quite complex. It depends on wind stress acting on the sea surface, on turbulence and coherent motions, on shortwave radiation absorbed in the upper millimeters of the ocean, on heat, salt, freshwater, and gas fluxes crossing these sublayers, and on gravity and capillary waves and surface films. We will consider many of these factors in detail throughout this chapter.

Section 2.2 describes the phenomenology of the viscous, thermal, and diffusion sublayers at the waterside of the air–sea interface. Intimately linked to the physical processes are the complex chemical, photochemical, and biological metamorphoses that take place in the ocean microlayer. The physics of the microlayer, and even the regime of air–sea exchanges, depend on the organics and chemical composition of surface films, and, to some extent, on the sea surface microlayer ecosystem.

The physics of the microlayer are discussed in detail in Sect. 2.3. Renewal and boundary-layer models of the aqueous molecular sublayers are introduced in Sect. 2.4. The renewal model results in a coupled set of parameterizations describing the surface wind-drift current, cool skin, and interfacial gas-transfer velocity. In Sect. 2.5, we discuss the effect of solar radiation absorption on molecular sublayers. Section 2.6 is devoted to the effect of precipitation on the microlayer.

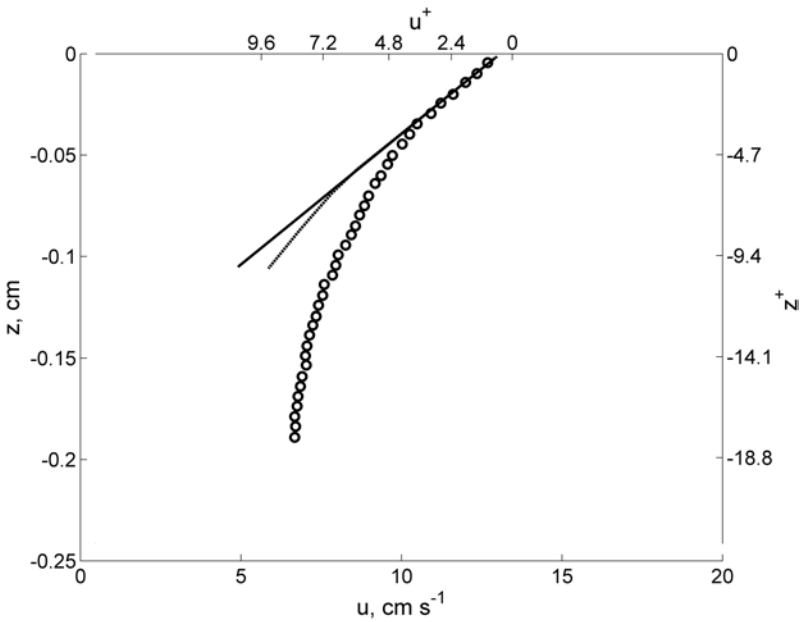

Fig. 2.2 Velocity profile below the free water surface measured in a laboratory tank (circles). The straight line fits the near-surface slope, and the curved line follows the mean profile at a solid boundary. The solid boundary dependence is derived from nondimensional values by Kline et al. (1967). The nondimensional coordinates are as follows: $z^+ = zu_* / \nu$ and $u^+ = (u_0 - u)/u_*$, u_* is the friction velocity in water, ν is the molecular kinematic viscosity of water, u is the downwind water velocity, and u_0 is the downwind water velocity at the surface. (After McLeish and Putland 1975)

2.2 Phenomenology

2.2.1 Viscous Sublayer

Viscous sublayers develop on both sides of the air–sea interface. To our knowledge, direct measurements of the viscous sublayer either from the oceanic or atmospheric side of the air–sea interface have never been made in real oceanic conditions. Information about the aqueous viscous sublayer of the ocean has been mainly obtained from theoretical considerations (for instance, Csanady 1978) or laboratory studies (McLeish and Putland 1975; Wu 1975; and others).

Figure 2.2 shows the velocity profile below the water surface measured at a 0.07 N m^{-2} wind stress in the laboratory experiment of McLeish and Putland (1975). The slope of the near-surface velocity profile is fit with a straight line. The linear vertical profile of velocity is a distinctive feature of the viscous sublayer. The departure of the velocity profile from its linear fit can therefore serve as an indicator of the viscous sublayer depth. It is remarkable that in dimensionless coordinates, the thickness of the viscous sublayer near the free surface is approximately half of

what it would be near a rigid wall. This is explained by the fact that only the vertical component of turbulent fluctuation is effectively suppressed near the free surface; as a result, turbulent eddies can penetrate closer to a free boundary than to a wall. However, this is not the only possible explanation. Another plausible explanation is that microscale wave breaking (see Banner and Phillips 1974; Csanady 1990) increases turbulent mixing near the surface, which reduces the thickness of aqueous viscous sublayer.

2.2.2 Thermal Sublayer

The SST may differ from the temperature of the underlying mixed layer due to the presence of the aqueous thermal molecular sublayer. This sublayer is also referred to as the *cool skin* of the ocean (Saunders 1967b). During daytime, the temperature difference across this aqueous sublayer due to absorption of solar radiation may change sign, turning into the *warm skin* (Soloviev and Schlüssel 1996).

Above the interface, there is a millimeter-thick atmospheric boundary layer, where the vertical transport is also dominated by the molecular diffusion. The largest temperature difference across the air–sea interface is observed in the air rather than water (Volkov and Soloviev 1986).

Figure 2.3 gives an example of the temperature profile in the upper 10 m of the ocean obtained with a *free-rising profiler* (Soloviev 1992). For this measurement, the profiler was equipped with a high-resolution temperature probe (5 μm diameter wire sensing element). The shunting of the micro-wire probe by seawater was small due to the fact that its internal resistance was only 7 Ω, while the surface area of the micro-wire was extremely small (Azizjan et al. 1984).

The vertical temperature profile shown in Fig. 2.3 was taken during night time. The upper part of the profile reveals an abrupt temperature change in the upper few millimeters due to the cool skin. The temperature difference across the cool skin in the example shown in Fig. 2.3 is $\Delta T = T_0 - T_b \approx -0.3°\mathrm{C}$, where T_0 is the SST and T_b is the temperature of the bulk (diurnal mixed layer) water. The temperature gradient below 2 m represents the remnants of the diurnal thermocline formed during the previous daylight hours.

The temperature difference across the cool skin depends on the local regime of air–sea interaction and thus varies in space and time. Historically, much effort has been devoted to the cool-skin parameterization. Saunders (1967b) initially parameterized the average temperature difference across the cool skin $\overline{\Delta T}$ by ascribing a constant value to the nondimensional coefficient, $\lambda_s = c_p \rho u_* \overline{\Delta T} / (\mathrm{Pr} Q_0)$. Grassl (1976) found that λ_s varied with wind speed. The parameter λ_s increased from zero for calm weather conditions to approximately five at moderate wind speeds. Kudryavtsev and Soloviev (1985) explained this dependence of λ_s on wind speed by the transition from convection to a wind–wave regime.

The typical temperature difference across the cool skin is from –0.2 to –0.3 °C increasing approximately two times under calm weather conditions (Horrocks et al.

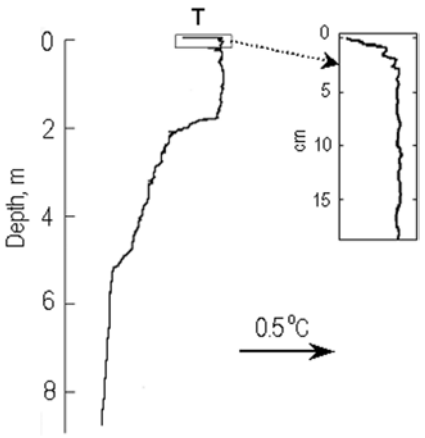

Fig. 2.3 An "instantaneous" vertical profile of temperature in the upper ocean taken under low wind speed conditions. (After Soloviev 1992)

2003). Under strong insolation and/or air temperature exceeding water temperature, the interfacial layer can become slightly warmer than the underlying water.

Collecting high-quality measurements of the cool skin in the open ocean is still a challenge, requiring very specialized techniques. In the oceanographic literature, there are only a few reports of direct profile measurements in the cool skin in the open ocean (Mammen and von Bosse 1990; Soloviev 1992; Ward and Minnett 2001). At the same time, infrared measurement techniques have been under intensive development (Saunders 1967b; McAlister and McLeish 1969; Hasse 1971; Grassl 1976; Paulson and Simpson 1981; Schlüessel et al. 1990; Minnett 2003; and others). As a result, most of the open-ocean data on the cool skin come from infrared SST measurements. A problem of interpretation of the infrared SST measurements is that the longwave radiation reflected from clouds produces strong disturbance of the SST measurement. In order to address this problem, Grassl (1976) constructed an infrared radiometer moving the beam between the sea surface and a seawater bath, which substantially reduced the error due to the signal reflected from clouds. The Tropical Ocean Global-Atmosphere Coupled Ocean-Atmosphere Response Experiment (TOGA COARE) exploited an advanced version of Grassl's method: From 30 January to 24 February 1993, measurements were taken from the R/V *Vickers* in the western equatorial Pacific Ocean (156°E, 2°S). The skin temperature measured with this setup was accurate to 0.05 °C.

Fiedler and Bakan (1997) and Minnett et al. (2001) have developed a multichannel infrared interferometer, which does not require a reference seawater bath. This approach has provided large high-quality data sets of SST of the ocean.

For calculating the temperature difference across the cool skin from the infrared SST measurement, it is also necessary to know the bulk-water temperature below the cool skin. Unfortunately, measurements with sensors towed behind or near the ship are disturbed by the ship's wake, which may introduce substantial errors. The alternative approach is to derive the bulk-water temperature from a ship's thermosalinograph, which takes in water from 3 to 5 m depth, although, a shallow diurnal or rain-formed thermocline may result in a vertical temperature gradient between the

depth of the thermosalinograph intake and the cool-skin layer. An appropriate temperature correction can be calculated with a diurnal mixed layer model forced with the air–sea momentum, heat, and precipitation fluxes, assuming these are available. This correction, however, may introduce outliers by itself due to errors of the model and atmospheric forcing data.

2.2.3 Diffusion Sublayer

The near-surface molecular diffusion sublayer is a crucial element in air–sea gas exchange. The resistance to air–sea gas transfer is mainly due to the diffusion sublayer in water, which is of the order of 50 μm thick (Bolin 1960).

The diffusion sublayer associated with salinity transport has approximately the same thickness as the gas diffusion sublayer (Fedorov et al. 1979). Under evaporative conditions, the sea surface salinity is higher than in the bulk of water, while during rainy conditions, a *freshwater skin* of the ocean is formed (Schluessel et al. 1997).

There are no direct observations of the diffusion molecular sublayer in the open ocean because of the complexity of the microscale measurements near the moving air–sea interface. Some parameters of the aqueous diffusion sublayer can be evaluated from data on the gas-transfer velocity because practically all gas concentration difference is in the ocean rather than the atmospheric diffusion sublayer. In particular, the thickness of the diffusion sublayer is defined as follows:

$$\delta_\mu = \mu \Delta C / G_0 \tag{2.4}$$

where μ is the kinematic molecular diffusion coefficient of gas, G_0 is the flux of property C at the air–sea interface, $\Delta C = C_w - C_0$ is the ensemble averaged air–sea gas concentration difference in property C across the diffusion sublayer, and C_0 and C_b are the averaged concentrations of property C at the water surface and in the bulk (mixed layer) water, respectively. Taking into account (1.50), we obtain the following relationship connecting the gas exchange coefficient and the thickness of the diffusion sublayer:

$$\delta_\mu = \mu / K_\mu. \tag{2.5}$$

2.2.4 Sea Surface Microlayer Ecosystem

The sea surface is a highly productive, metabolically active interface (Hardy et al. 1997). Due to extreme conditions at the air–sea interface, the sea surface is believed to be the place where life on the Planet originated (a competing theory is that of extraterrestrial origin for life on the Earth).

Phytoplankton in the water column produces an abundance of particulate and dissolved organic material, some of which is transported to the surface either passively by buoyancy or actively by upwelling, turbulence, and bubble transport. The natural and anthropogenic compounds deposited from the atmosphere often accumulate on the ocean surface in relatively high concentrations compared to those in the water column. The abundance of organic matter at the sea surface provides a substrate for the growth of the surface-dwelling organisms, the marine *neuston*, which inhabits the sea surface microlayer (Zaitsev 1997).

Neuston realm is a vast habitat. The distinctive physical and chemical characteristics of the sea surface can explain a highly diverse and abundant assemblage of species in the microlayer. Organisms from most major divisions of the plant and animal kingdoms either live or reproduce or feed in the surface layers (Zaitsev 1971). Many of these species are of commercial and ecological importance. The *microneuston*, which may be involved in biogeochemical cycling, and neustonic eggs and larvae of commercially important fish and shellfish, are of particular interest.

Figure 2.4 shows Hardy's (1982) conceptual model of the sea surface microlayer ecosystem. Permanent inhabitants of the surface layer often reach much higher densities than similar organisms found in subsurface waters. The communities of bacteria, phytoplankton, and zooplankton present within this neuston layer are named the bacterioneuston, phytoneuston, and zooneuston, respectively.

There are also numerous temporary inhabitants of the neuston. These are particularly the eggs and larvae of a great number of fish and invertebrate species. The latter utilize the surface during a portion of their embryonic and larval development. Some neuston can remain in the microlayer until turbulence created by breaking waves at winds exceeding 10–15 m s^{-1} disperses them (Zaitsev 1971).

An alternative conceptual model of the sea surface microlayer is schematically shown in Fig. 2.5. In this model, the sea surface microlayer is a gelatinous biofilm, which is formed by transparent exopolymer particles (TEPs). This model is based on the Wurl and Holmes (2008) experimental result suggesting that some TEPs float up to the surface microlayer, forming a gelatinous film. TEPs are a result of the coagulation of biogenic polysaccharides, particularly those produced by phytoplankton. TEPs are critical in the formation of marine aggregates, acting as the binding matrix or "glue" that holds the aggregate together (Verdugo et al. 2004).

TEPs are also readily colonized by microorganisms, including surfactant-producing bacterium. The presence of surfactants may have important impact on dynamics of the sea surface (see Sect. 2.3).

2.2.5 Surfactants and Surface Films

Following Liss and Duce (1997), here we use the following terminology: A film refers to surfactant-influenced surface and a *slick* refers to a visibly surfactant-influenced surface.

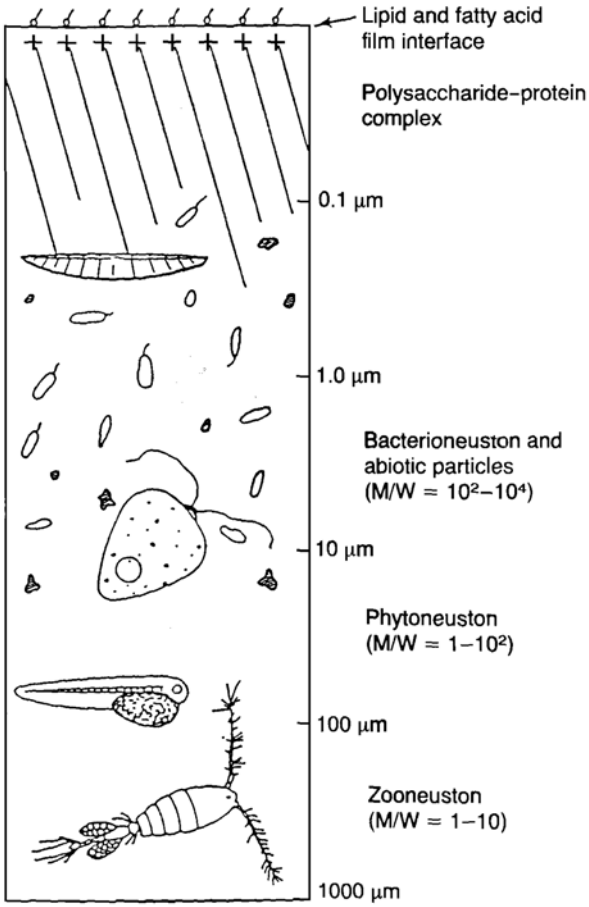

Fig. 2.4 Conceptual model of the sea surface microlayer ecosystem. M/W = typical microlayer to water concentration ratios based on a number of studies. (Reproduced from Hardy (1982) by permission of Elsevier)

Sea surface films are derived from multiple, sea- and land-based sources, including bulk seawater dissolved organic matter, terrestrial sources (natural and anthropogenic), and petroleum seeps and spills (Liss et al. 1997). Surface films dissipate due to loss of material at the surface, including microbial degradation, chemical and photochemical processes, and loss due to absorption and adsorption onto particulates.

Under favorable physical conditions, the concentration of dissolved organic matter is sufficient to produce surface enrichments of organic matter even in oligotrophic waters, where biological productivity is low. Lifecycles of neuston organisms and phytoplankton blooms also lead to the production of the surface-active substances.

The source contribution primarily controls the chemical composition of surface films. A variety of biological, chemical, and physical processes may, nevertheless, change composition, concentration, and spatial structure of the surface films and thus modify physical properties of the air–sea interface. Turbulence and diffusion,

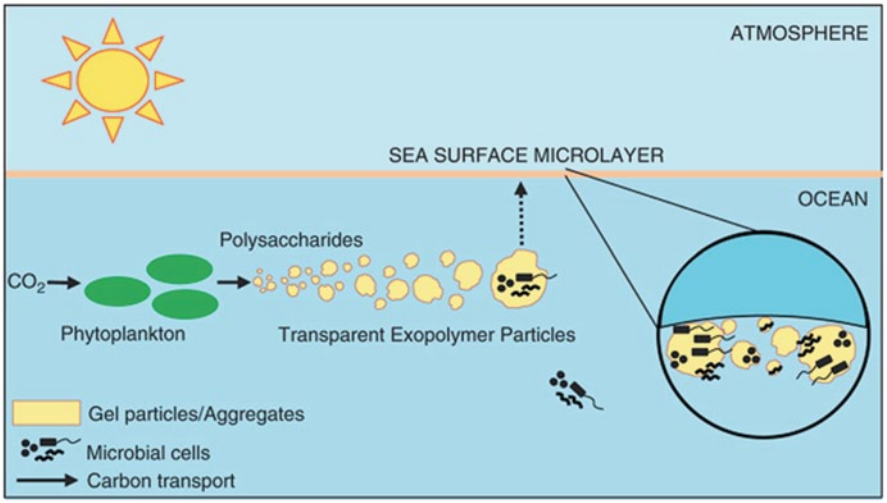

Fig. 2.5 Conceptual model of the sea surface microlayer based on the Wurl and Holmes (2008) study. The formation of transparent exopolymer particles (TEPs) in the near-surface layer of the ocean is a pervasive process, which is also a significant component of the global carbon cycle. Some TEPs float up to the surface microlayer, forming a gelatinous film. TEPs are readily colonized by microbial cells. (Reproduced from Cunliffe et al. (2009) by permission of John Wiley & Sons Ltd)

scavenging, and transport by bubbles and buoyant particles effectively spread surfactants over broad areas of the ocean surface. At the same time, flow convergences associated with organized structures, upwelling events, and internal waves have tendency to localize surface-active materials on various spatial scales, ranging from a few meters to kilometers (Bock and Frew 1993; Liss and Duce 1997).

Sampling of the sea surface microlayer is a challenge. A number of methods have been developed for surface microlayer sampling, including mesh screens (Garrett 1965), glass plates (Harvey and Burzell 1972), and membranes (Kjelleberg et al. 1979). All of these sampling methods, however, result in some degree of contamination, from either the research vessel or underlying water column.

Franklin et al. (2005) implemented DNA analysis of the sea surface microlayer. For this purpose, they used the 47-mm diameter, 2-μm pore polycarbonate membrane. The membrane was placed on the sea surface and attached to the surface by surface tension forces. Water samples were also collected from below the surface. Using this method, Franklin et al. (2005) showed that the bacterioneuston was distinctly different compared with subsurface water 0.4 m below the surface. The weakness of this method is that it is difficult to avoid distortions of the sea surface microlayer from the boat due to proximity of the sampling area to the boat hull.

Kurata (2012) and Kurata et al. (2013) improved this method by attaching the polycarbonate membrane filter to a fishing line and by using the fishing rod to deploy this filter away from the boat wake and then bringing it to the boat. They also used an advanced DNA analysis, which was able to identify surfactant-producing bacteria as well

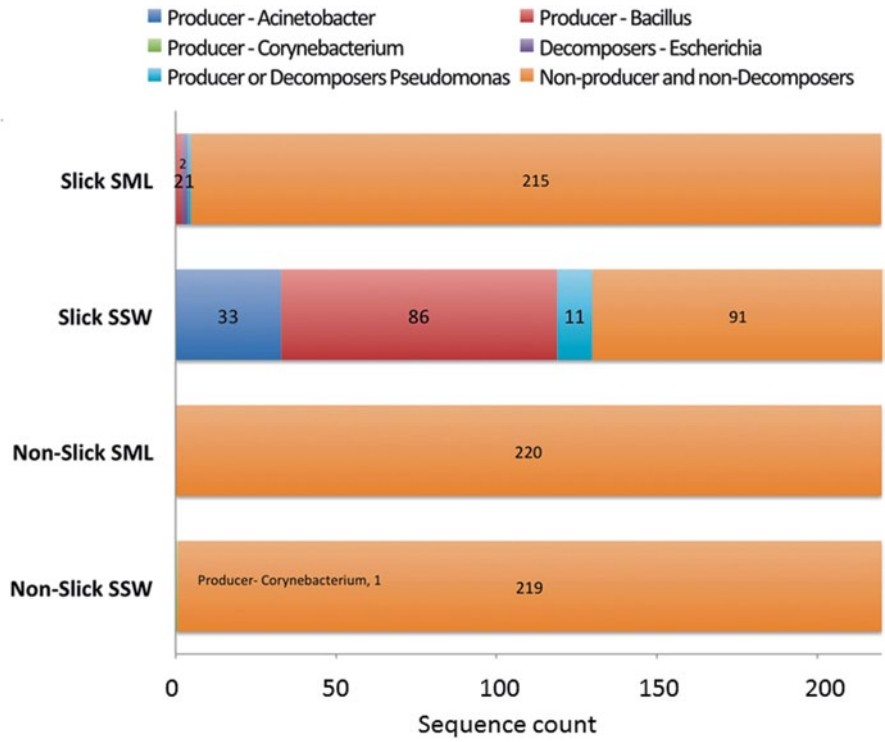

Fig. 2.6 Relative abundance of potential surfactant-associated genera in the sea surface microlayer (SML) and subsurface water (SSW). Sampling in slick and non-slick areas are shown on the synthetic aperture radar (SAR) image in Fig. 2.7. (After Kurata 2012 and Kurata et al. 2013)

as possible bacterial contamination during samples handling and laboratory analysis. The results of a pilot experiment in the Straits of Florida are shown in Fig. 2.6. Note significant diversity of surfactant-associated bacteria in the subsurface layer below the slick, which suggests that surfactants were produced by bacteria in the water column and transported to the surface by diffusion, air bubbles, or organized circulations. This slick was visible on the high-resolution synthetic aperture radar (SAR) satellite image taken during in situ measurements (Fig. 2.7). This case study reported by Kurata (2012) and Kurata et al. (2013) suggests that the DNA analysis of the near-surface organisms opens an opportunity to pinpoint exactly which organisms, and in what environmental conditions, are responsible for generation of surface active materials.

2.3 Physics of Aqueous Molecular Sublayers

The surface microlayer is subject to disturbances from near-surface turbulence (wave breaking, shear, convection, rising bubbles, spray hitting the sea surface, raindrops, etc.). Breaking waves that entrain air and thereby produce whitecaps are

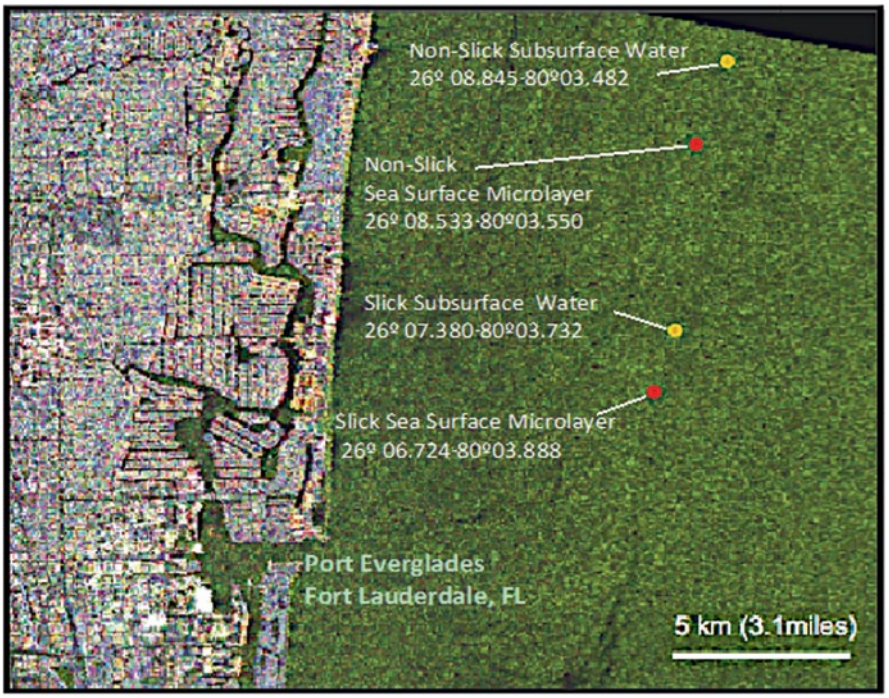

Fig. 2.7 The RADARSAT-2 polarimetric image taken during the pilot experiment in the Straits of Florida on July 10, 2010 to study sea surface microlayer (see Fig. 2.6).Marked are the location of the bacterioneuston in situ sample areas within and out of slicks. (After Kurata et al. 2013)

the most intense and obvious manifestation of the turbulent disturbance. Waves may also break without entraining air and producing whitecapping. This phenomenon is associated with the free-surface boundary condition and is called *microscale wave breaking* (Banner and Phillips 1974) or *rollers* (Csanady 1990). Capillarity effects and the presence of surface-active materials significantly complicate physics of the free surface.

2.3.1 Convective and Shear Instability

Convection and wind-induced shear are important factors in the physics of aqueous molecular sublayers. The molecular sublayers are not stationary and continuous but intermittent in time and space. The boundary-layer processes in the near-surface layer of the ocean are altered by the presence of the free surface (see Chap. 3).

Surface cooling and/or salinity increase due to evaporation initiate convection in the upper layer of the ocean. Convection as a type of hydrodynamic process has a tendency to self-organization and therefore exhibits features of organization (Sect. 5.7). The absorption of solar radiation or rainfall inhibits the convective instability.

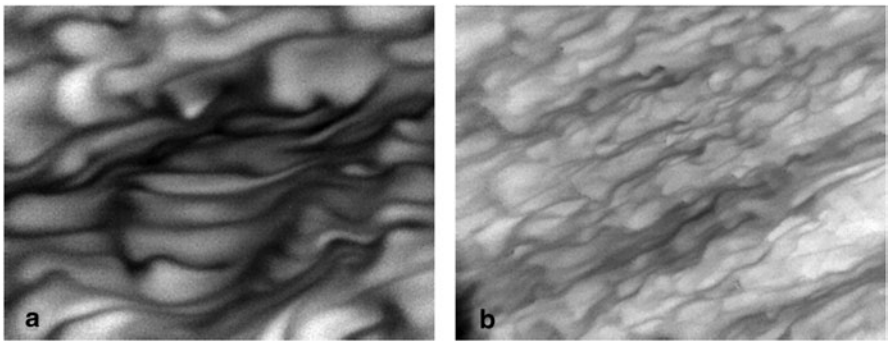

Fig. 2.8 Infrared images of the surface taken in the RSMAS air-sea interaction tank for: **a** light and **b** moderate winds with an imposed air-water temperature difference of 10°C.The water is warmer than the air and light areas are warmer water. (Courtesy of Mark Donelan)

With no solar radiation and precipitation effects, convective instability of a thermal molecular sublayer occurs at low wind speeds. Under moderate and high wind speeds, the molecular sublayers are controlled by the wind stress and surface waves.

Laboratory experimentation involving visualization techniques helps to understand the physics of molecular sublayers. Figure 2.8a shows infrared images of the water surface under convective conditions. The mean temperature is subtracted in the images. White represents temperatures above the mean, and black represents temperatures below the mean. The full range of shades corresponds to 2°C. The spatial and temporal structures observed in the surface temperature field are obviously linked to the near-surface turbulence. The thin cool sheets (black on infrared images) are the convergences, while the wide areas of warm water (white) are divergences. These processes are indicative of surface renewal events. Note a pronounced change in the surface structures from light winds to moderate winds (Fig. 2.8b).

In a laboratory experiment, Syalor et al. (2002) studied the cross-correlation between surface temperature and the vertical component of subsurface velocity in the regime of free convection and found practically zero time lag between the surface and subsurface events. In the Syalor et al. (2002) experiment, the event occurring at the surface would require a delay on the order of 20 s to reach 2 cm depth via turbulent transport. Spangenberg and Rowland (1961), Katsaros et al. (1977), and Volino and Smith (1999) previously reported falling sheet structures during evaporative convection penetrating to several centimeters depth and migrating significant horizontal distances across the surface before disappearing. As structures pass over the measurement location, a sudden change in velocity and temperature resembling bursting event should almost simultaneously be observed at the surface and at 2 cm.

Observations in the open ocean appear to be consistent with the idea of periodic water renewal in near-surface molecular sublayers. Figure 2.9a shows a temperature profile in the upper 10 m obtained with a free-rising profiler under conditions of nighttime convective cooling and low wind speed. The upper part of the tempera-

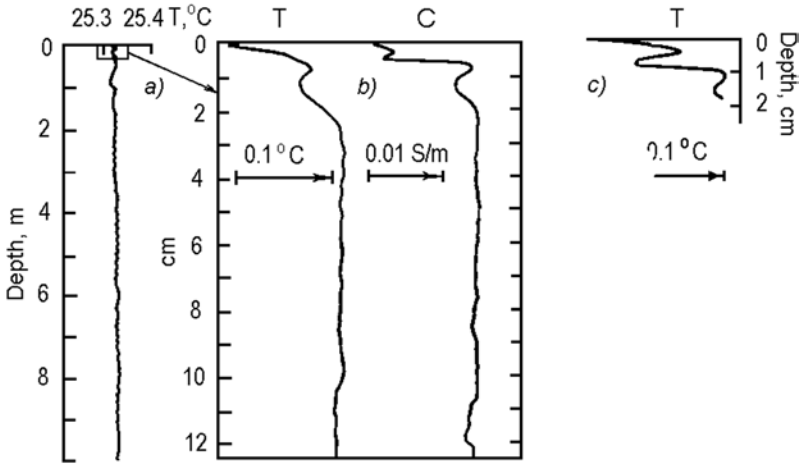

Fig. 2.9 a, b Vertical structure of the near-surface layer of the ocean from measurements with a free-rising profiler in the equatorial Atlantic made at night (02:57 LT) under conditions of low wind speed (U_{10}= 3 m s^{-1}) and intense cooling of the ocean surface (Q_0= 170 W m^{-2}) in comparison **c** with the data from laboratory experiment of Ginzburg et al. (1977). *T* temperature, *C* conductivity of seawater. (Reproduced from Soloviev and Vershinsky (1982) by permission of Elsevier)

ture profile marked by a rectangle in Fig. 2.9a is shown in more detail in Fig. 2.9b. The simultaneous conductivity profile is also shown. The upper 2 mm of the conductivity profile is removed because of the disturbance to the conductivity measurement in the vicinity of the air–water interface.

In the upper few centimeters, the temperature (and conductivity) profile is characterized by inversion, which is presumably caused by convection. According to Katsaros et al. (1977), the temperature inversions in the upper few centimeters can be due to the passage of discrete convective elements (thermals). Figure 2.9c shows a temperature profile obtained near the water surface in a laboratory experiment conducted by Ginzburg et al. (1977) in the free convection regime.

The conductivity sensor in this experiment had a higher spatial resolution (better than 1 mm in vertical direction) than the temperature sensor and therefore revealed more detail (Fig. 2.9b). According to estimates by Soloviev and Vershinsky (1982), in the nighttime convective mixing regime (no precipitation or insolation), the conductivity profiles in the near-surface layer of the ocean mainly depend on the temperature rather than salinity variations. Frictional scales of the turbulent temperature and salinity fluctuations are

$$T_* = \frac{Q_0}{c_p \rho \kappa u_*} \qquad \text{and} \qquad S_* = \frac{Q_E S_0}{\rho \kappa u_* L}, \tag{2.6}$$

respectively, where S_0 is the average surface salinity, L is the latent heat of vaporization, Q_E is the latent heat flux, c_p is the specific heat capacity of water, and κ is the von Karman constant.

For inhomogeneities exceeding the Kolmogorov internal length scale of turbulence (2.1), the ratio of the temperature and salinity scales expressed in terms of the equivalent conductivity changes is as follows:

$$\frac{\Delta C_T}{\Delta C_S} = \frac{\gamma_T T_*}{\gamma_S S_*} = \frac{\gamma_T}{\gamma_S} \frac{LQ_0}{c_p S_0 Q_E} \approx 25, \tag{2.7}$$

where $\gamma_T = (\partial C / \partial T)_{S,p}$ and $\gamma_S = (\partial C / \partial S)_{T,p}$. The estimates of the Kolmogorov length scale for temperature (2.2) and salinity (2.3) are $\eta_T \approx 0.7$ mm and $\eta_D \approx 0.07$ mm, respectively. These estimates are made for the conditions of experiments reported by Soloviev and Vershinsky (1982) under an assumption that the turbulence is driven by convective instability. Since the shear and surface wave instability can only add to the turbulence dissipation level, these are the upper bound estimates of η_T and η_D. According to (2.7), the contribution of temperature to the conductivity changes during nighttime convection well exceeds that of salinity. The high-resolution conductivity profiles can therefore be interpreted in terms of temperature.

Figure 2.10 shows a series of conductivity profiles in the depth range from 2 mm to 20 cm obtained during nighttime. The time interval between successive profiler was from 5 to 9 min; the ship drifted for tens of meters.

For the conditions of this experiment, an estimate for the flux Rayleigh number defined according to Foster (1971) is $Ra_f = \alpha_T g Q_0 h^4 / (\kappa_T{}^2 \nu) \approx 10^{12}$, where h is the mixed layer depth (equal to 50 m in this estimate). Free convection at very large Rayleigh numbers is intermittent in space and time (Turner 1973). Howard (1966) formulated a phenomenological theory of the convection at large Rayleigh numbers that represented turbulent convection as the following cyclic process: The thermal boundary-layer forms by diffusion, grows until it is thick enough to develop convective instability, and is destroyed by convection, which in turn dies down once the boundary layer is destroyed. Then the cycle begins again.

The convective period at the ocean surface is of the order of tens of seconds only; the horizontal length scale of the convective cells is about 1 cm (Foster 1971). The vertical profiles shown in Fig. 2.10 are consistent with Howard's theory in general. Since the profiling time interval greatly exceeded the intermittency period of the convection, in interpreting the results shown in Fig. 2.10 it is necessary to assume that there is no correlation between any two successive temperature profiles in this series of measurements. Following Howard's (1966) phenomenology, the profiles obtained at 02:51, 02:57, 03:18, 03:27, and 00:34 LST can be interpreted as the stage of destruction of the cold surface sublayer by a discrete convective element (thermal). The profiles obtained at 03:04, 03:09, 03:43, and 03:51 LST can be related to the stage of dissipation of the thermal and beginning of the next cycle by the formation of the unstably stratified thermal sublayer due to the molecular heat diffusion.

The observations shown in Figs. 2.9 and 2.10 provide an insight into the renewal process near the surface in convectively unstable conditions. In particular, the data are consistent with the concept of intermittent convection in the near-surface layer, which has found its application for the modeling of the aqueous molecular sublayers.

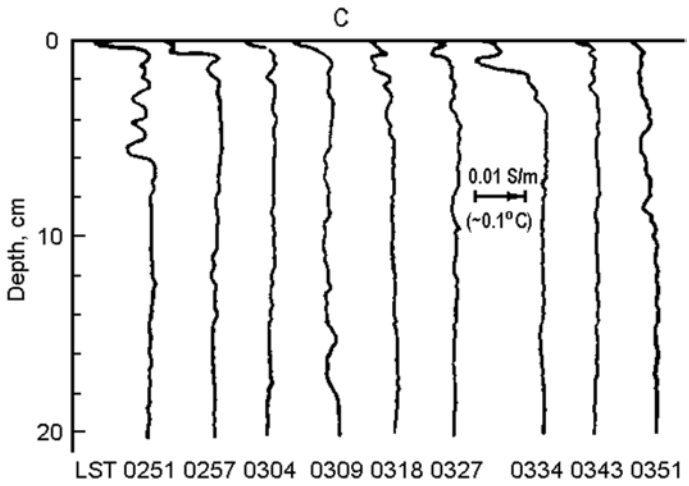

Fig. 2.10 Vertical profiles of conductivity observed during night under convectively unstable conditions near the surface according to measurements in the equatorial Atlantic. The time of observation is marked (LST) under each profile. Wind speed $U_{10} = 3$ m s^{-1}, net surface heat flux $Q_0 = 170$ W m^{2}. The scale of conductivity is shown in the equivalent temperature units under the assumption of constant salinity. (Reproduced from Soloviev and Vershinsky (1982) by permission of Elsevier)

2.3.2 Microscale Wave Breaking

Microscale wave breaking has been the subject of several theoretical, laboratory, and modeling studies. Laboratory wind–wave studies of Okuda (1982) and Ebuchi et al. (1987) revealed a high-vorticity region near the crests of gravity waves with capillary ripples generated ahead of the crests. Longuet-Higgins (1992) identified the origin of vorticity within this surface roller as accompanying parasitic capillaries, which themselves generate fluid rotation (i.e., vorticity) via the surface tension effect (Yeh 1992). Rollers (Longuet-Higgins 1992), breaking wavelets (Csanady 1990), steep wind waves accompanied by a high-vorticity layer near the crest (Okuda 1982), and microscale breaking (Banner and Phillips 1974) appear to be descriptions of the same phenomena.

Microscale breaking waves are typically 0.1–1 m in length and a few centimeters in amplitude. The schematic diagram and the photo from a laboratory experiment shown in Fig. 2.11 illustrate the typical features of microscale wave breaking. Note the bore-like structure at the crest accompanied by parasitic capillary waves distributed along the forward face. Microscale wave breaking is far more widespread than whitecapping. The absence of air entrainment makes the microscale breaking difficult to identify visually. The microscale wave breaking, however, produces the convergence of flow that leads to intense renewal of surface water. The process of surface renewal substantially determines properties of the aqueous molecular sublayers under moderate wind-speed conditions (Csanady 1990).

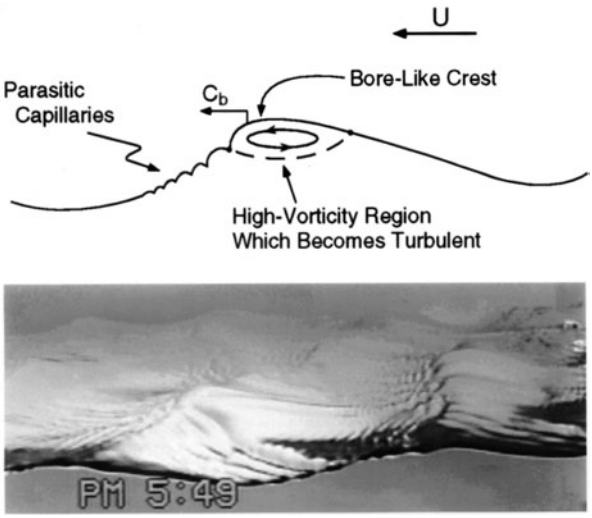

Fig. 2.11 The characteristic feature of a microscale breaking wave is the bore-like crest with parasitic capillary waves riding along the forward face. U wind speed, C_b crest speed of the breaking wavelet (After Longuet-Higgins 1992). Bottom: photograph of a breaking wavelet with a wavelength of roughly 0.1 m (adapted from Jessup et al. 1997). (Reproduced by permission of American Geophysical Union)

2.3.3 *Wave Breaking and Whitecapping*

The widespread occurrence of microscale wave breaking suggests that its cumulative effect on the fluxes of heat and gas across the air–sea interface is significant (Csanady 1990; Banner and Peregrine 1993; Soloviev and Schlüssel 1994; Melville 1996). The aqueous molecular sublayers at the air–sea interface are associated with the action of the tangential wind stress on the sea surface. The tangential component represents only a part of the total wind stress that is transferred from the atmosphere to the ocean. Under high wind speeds, a significant portion of the momentum is transferred to surface waves. Surface waves periodically break destroying the aqueous viscous sublayer as well as the thermal and diffusion sublayers. The molecular sublayers regenerate between wave-breaking events.

The ratio of the tangential wind stress τ_t controlling the aqueous viscous sublayer to the total air–sea momentum flux τ_0 is as follows (Soloviev and Schlüssel 1996):

$$\tau_t = \tau_0 (1 + Ke / Ke_{cr})^{-1}, \tag{2.8}$$

where

$$Ke = u_*^3 / (g\nu) \tag{2.9}$$

is the *Keulegan number*, which is a fundamental parameter in the dynamics of free interfaces (Csanady 1990). At low Keulegan numbers, $Ke << Ke_{cr}$ interfacial instabilities are suppressed by molecular viscosity.

Formula (2.8) reflects the transformation of a substantial part of the surface wind stress to form drag and whitecapping at high wind speeds. Figure 2.12 illus-

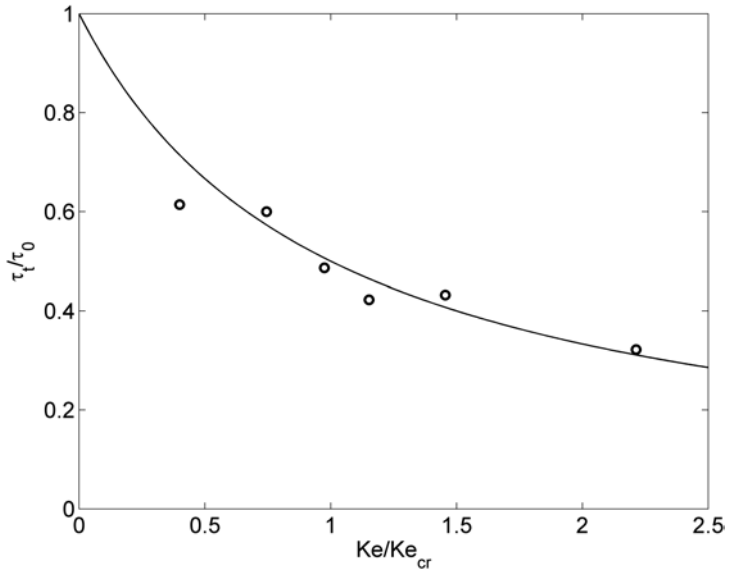

Fig. 2.12 Transformation of the surface wind stress to form drag and whitecapping for high wind speeds. The line is equation (2.8); the circles represent the experiment of Banner and Peirson (1998). (After Soloviev and Schlüssel 1996)

trates this dependence for $Ke_{cr} = 0.18$ in comparison with the data from the Banner and Peirson (1998) laboratory experiment. The theoretical curve is in reasonably good agreement with the experimental data taking into account that the estimate, $Ke_{cr} = 0.18$, had been independently derived by Soloviev and Schlüssel (1994) from the wind-speed conditions for which energy-containing surface waves first start breaking.

2.3.4 Capillary Wave Effects

The presence of capillary waves on the sea surface is a characteristic feature of air–sea interaction. In particular, parasitic capillaries accompany microscale wave breaking, which is one of the principle mechanisms controlling the molecular sublayers, as discussed in the previous section. The overall knowledge about the role of capillary waves in air–sea molecular sublayers and exchanges is still far from satisfactory.

Csanady's (1990) theoretical analysis suggests that the capillary waves by themselves do not contribute substantially to the convergence in the aqueous molecular sublayer. For the molecular sublayers, the surface within capillary waves still appears to be smooth from the waterside, unless there is substantial divergence occur-

ring in parts of the wavelets, for instance, as described by the rollers on top of short gravity waves.

Wu (1996) refers to laboratory measurements reporting a rapid increase in the gas-transfer velocity coinciding with the onset of capillary waves on the water surface (Kanwisher 1963; Broecker et al. 1978). After a critical discussion of the laboratory findings, Wu (1996) proposed the idea of a sudden change of the gas-transfer velocity due to the direct influence of the steep capillary waves on the aqueous molecular sublayer.

Soloviev and Schlüssel (1998) proposed an alternate explanation of the Wu (1996) results: The change of surface roughness due to capillary waves could directly influence the flow on the airside of the interface, thus modifying the wind stress. The sudden change could be merely a reaction to enhanced roughness modifying the wind field rather than a direct impact of the ripples on the aqueous molecular sublayer. The change of roughness could result in a sudden increase in the friction velocity and hence in the intensification of the air–water gas exchange. Another interpretation of the Wu (1996) results points to the connection between microscale wave breaking (rollers) and the parasitic capillaries (Soloviev and Schlüssel 1998). The rollers, if present in the Wu (1996) experiment, would result in a significant effect on the air–sea exchange. In any case, this is a rather indirect influence of capillary waves on the diffusion sublayer.

There is nevertheless evidence of a direct impact of the capillary waves on air–sea exchange. Saylor and Handler (1997) experimented in a small laboratory tank with capillary waves from 2.62 to 3.62 mm wavelength (which corresponds to 400 to 200 Hz frequencies) and found an almost two orders of magnitude increase in the interfacial gas transport rate as the wave slope was increased from 0 to 0.2 mm^{-1}. In this work, small vertical vibration of the tank generated capillary waves via the Faraday instability. The Saylor and Handler (1997) experiment provides remarkable evidence that capillary waves can greatly increase fluxes across the air–water interface. Applicability of these results to the real ocean, however, is not completely clear since the Faraday waves differ from the parasitic capillaries observed in a wind/wave tank or on the open-ocean surface. In natural conditions, the capillary waves of these frequencies (from 200 to 400 Hz) dissipate quickly and may only cover a very small percentage of the sea surface, while in the tank waves excited via the Faraday instability completely covered the water surface.

As seen on the ocean surface, capillary waves indeed appear suddenly when the wind speed exceeds some threshold level. The wind speed has not only a mean but also a variance that makes the sea surface patchy with respect to the coverage with capillary waves (the so-called “cats paws”). As the wind speed increases, the area covered by ripples gradually increases so that the surface averaged over a larger area should demonstrate a smooth transition from no capillary waves to full coverage without an obvious “jump.” This is relevant to the mean gas transfer (i.e., averaged over some space and time intervals). The sudden increase should only be observed on a small scale that might be relevant to fluctuations but not to the mean exchange.

The sudden increase in gas transfer has been observed mainly (if not exclusively) in laboratory studies (see, for instance, Fedorov and Ginzburg 1988). The natural variance of the wind speed, and the implied variance of the surface patches covered with capillaries, does not occur in the laboratory airflow. This is an important difference between the tank airflow and the open-ocean wind pattern; it is basically because timescales of wind velocity fluctuations in the laboratory and in the field conditions are very different (Soloviev and Schlüssel 1998).

Finally, as summarized by Cox (2001), several processes may be at work:

1. Convergence/divergence of orbital motions in waves disturbs the boundary layer at the interface where fluxes are controlled by molecular diffusion.
2. The decay of capillary wave trains accompanying rollers delivers horizontal momentum to the water in patches corresponding to the locations of the wave trains. This patchy driving force can induce turbulent motions of a size corresponding to the length of the wave train.
3. Short gravity waves and capillaries dramatically increase the momentum transferred to the ocean via increased sea surface roughness, thus enhancing near-surface mixing.
4. In addition, the properties of capillary waves depend considerably on the presence of surfactants and surface films.

2.3.5 *Chemical and Photochemical Reactions in the Sea Surface Microlayer*

Complex chemical, photochemical, and biological metamorphoses take place in the ocean microlayer. Photochemical and chemical reactions rapidly developing within the microlayer could produce a variety of feedbacks to the biological and physical processes (Plane et al. 1997). For example, elevated levels of highly reactive intermediate products produced in the microlayer could represent a ‘reaction barrier’ to the transport of gases and some chemicals across the air–sea interface. Certain photochemical reactions destroy or produce surfactants modifying surface films; altered surface waves from the gravity-capillary band then affect gas exchange rates. Many other reactions occur within the microlayer, in particular those increasing or reducing the surface concentrations of certain gases relative to their bulk-water concentrations, as well as those influencing the types and the distributions of microlayer materials ejected to the atmosphere during bubble bursts and delivered to the deep ocean by coalescent particles.

2.3.6 *Natural and Anthropogenic Influences*

In this book, we mainly focus on the physics of aqueous molecular sublayers. The physics, chemistry, and biology of the sea surface, nevertheless, are closely related.

For example, phytoplankton in the water column produces particulate organic matter and a variety of biogenic chemicals and gases, which then rise to the surface where they enter the microlayer (Hardy et al. 1997). This organic matter modifies surface films, which affects the gravity-capillary waves and, thus, the air–sea gas exchange on the global scale.

Increasing pollution of the ocean threatens marine neuston and represents one of the significant factors accelerating global ecological changes. Anthropogenic enrichment of the sea surface impacts natural biochemical processes in the ocean microlayer affecting the air–sea CO_2 exchange with possible consequences for global climate (Hardy et al 1997).

On the other hand, iron (the element which limits primary biological productivity) is supplied to the ocean via the surface microlayer. The increase in productivity due to an increased iron supply stimulates the ocean's "biological pump" increasing the CO_2 uptake by the ocean and potentially reducing the global warming (Wu et al. 2003).

The mechanical influence of disturbances produced by the swimming motion of small zooneuston organisms perhaps may also contribute to the microlayer structure at some level (Gladyshev 1997). Flying fish, birds, and ships disturb the microlayer significantly, though only locally.

2.3.7 Effects of Surface Films

Surface films are an important part of the sea surface microlayer. Air–sea exchanges depend on film properties, especially under low wind-speed conditions. Laboratory and field measurements show that the surface tension can be reduced by up to 60 % due to surface films (Hühnerfuss et al. 1987). The presence of surface films on the ocean is one of the factors leading to uncertainty in the existing air–sea exchange parameterizations.

The effects of surface films are dependent on the type and concentration of surface-active materials (surfactants) and wind–wave regime. Breaking waves and near-surface flow convergences substantially erode the surface films above wind speeds of 5–6 m s^{-1}. Surface films are also fragmented by rain, although there are observations suggesting that even in the case of intense rain the surface films are not completely removed (Baier et al. 1974).

The effect of surfactants on the properties of the sea surface has been studied in relation to air–sea fluxes (Frew 1997; Asher et al. 2005) and SAR imagery of the ocean surface (Chap. 7). The presence of surface films on the ocean is one of the factors leading to uncertainty in the existing air–sea exchange parameterizations under low wind-speed conditions. Surface films can affect air–sea exchanges through static and dynamic mechanisms (Liss 1983). The static mechanism results from the physical barrier provided by the film; it requires the presence of organized (condensed, solid) surfactant films that can easily be reproduced in the laboratory but hardly survive typical oceanic conditions of wind and waves. The films with

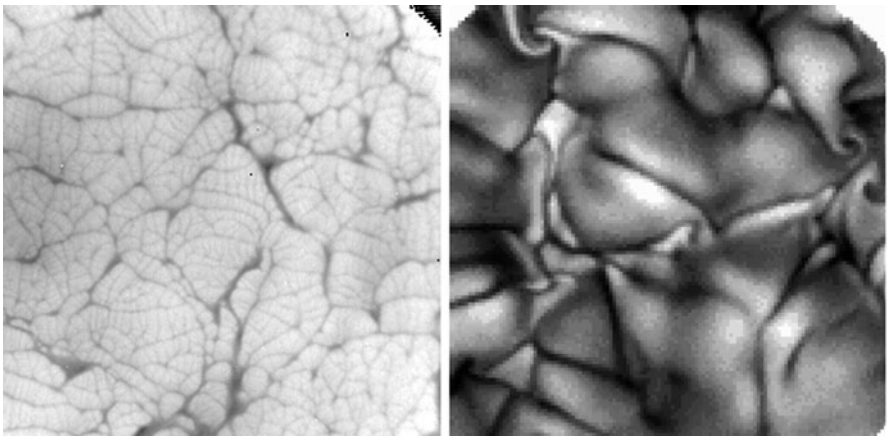

Fig. 2.13 Infrared images of sea temperature under convective conditions for clean (left subplot) and surfactant covered (right subplot) surface for a heat flux of 407 W m^{-2}. The mean temperature is subtracted in the images so that white represents temperatures above the mean and black represents temperatures below the mean. The dynamic range of the image is approximately 1 K. (Reused with permission from Flack et al. 2001 AIP)

high surface concentrations of organic material occupy only a small fraction of the global ocean surface. The dominant point of view among ocean chemists is that the organic matter concentrations are quite low in the open ocean. The static mechanism thereby is not of primary importance for typical open-ocean conditions (Liss and Duce 1997). The dynamic mechanism is more important in the ocean, because it can be effective even with relatively low surfactant concentrations.

The dynamic mechanism relates to the viscoelastic properties of surface films (Frew 1997). Nonzero viscoelasticity modifies the surface boundary conditions, which affects hydrodynamic processes at the air–sea interface. Figure 2.13 shows infrared images of clean and surfactant-covered water surfaces obtained in convectively unstable conditions. The spatial scale of the convective structures dramatically changes when surfactant is present on the water surface compared to a clean surface. The surfactant film inhibits very fine structures and emphasizes larger scale motions, some of which can be vortical. Damping effect of surfactants on the gravity-capillary waves (Fig. 2.14) is the result of the dilatational viscoelasticity of the monomolecular surface film.

The temperature dependence of surface tension leads to circulations driven by horizontal temperature gradients, referred to as the Maragoni effect (Katsaros 1980). Horizontal temperature gradients are produced by adjacent but phase-lagged surface renewals. Calculations of the Maragoni effect for typical temperature gradients produced by the surface renewals show that under low wind-speed conditions the renewal time would be reduced by orders of magnitude in the case of totally film-free water surfaces. This is not observed in the ocean because under natural conditions the sea surface is always covered by surface-active agents that diminish the temperature dependence of the surface tension to negligible values.

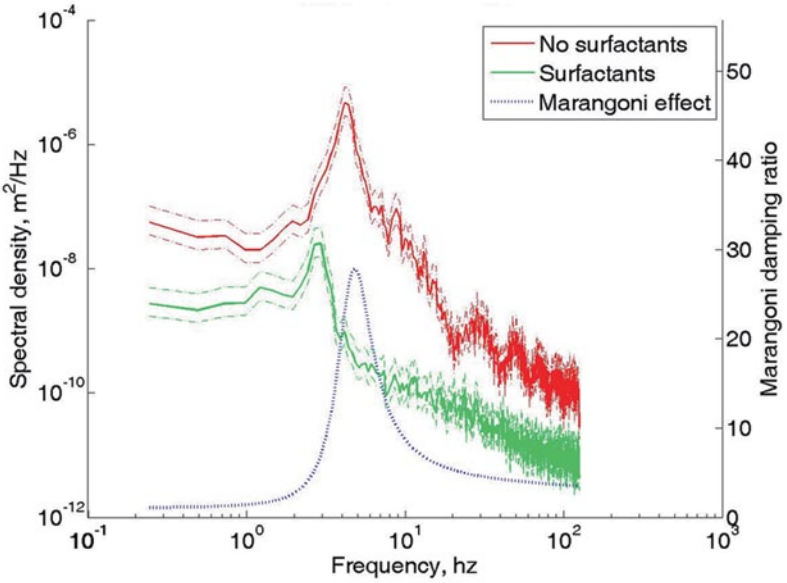

Fig. 2.14 Wind wave spectra of clean water surface (red) and in the presence of oleyl alcohol surface film (green)—measurements in ASIST facility of UM RSMAS. The 95 % confidence interval is shown by the dash-dot lines. The wind speed recalculated to a 10 m height was approximately $U_{10} = 7$ m/s. The dotted line represented the curve (ordinate on the right-hand side) for Marangoni wave theory for oleyl alcohol (eqs. 1–4 in Hühnerfuss 1987). After Soloviev et al. (2011) by permission of Kyoto University Press

Although rain fragments surface films, as already mentioned, there are observations suggesting that even in the case of intense rain the surface films are not completely removed (Baier et al. 1974).

Remarkably, the laboratory result shown in Fig. 2.15 suggests that the presence of surfactant increases the surface drift velocity by approximately 25 %. This is equivalent to the reduction of the drag coefficient from the waterside by 36 %. The reduction is even stronger when taking into account that the momentum transmitted from the air to the water surface is reduced in the presence of surfactant due to reduced surface roughness from the airside of the interface.

In order to understand the nature of the effect of surfactants on the drag coefficient from the waterside and increase in the surface drift velocity, Soloviev et al. (2011) measured the horizontal structure of the velocity field at a 2-cm depth using DIGITAL PARTICLE IMAGE VELOCIMETRY (DPIV). They observed "streak-like" features oriented in the along-tank direction. The streak-like features practically disappeared after the addition of surfactant and the corresponding variance of the horizontal velocity gradient reduced by almost a factor of 2 for both velocity components. Streak-like features have previously been reported from experiments and numerical simulations near the rigid wall (Lesieur 2008) and below the free surface (Dhanak and Si 1999; Tsai 2001). Streaks of low and high longitudinal velocity relative to the local mean velocity profile are a generic feature of the turbulent boundary

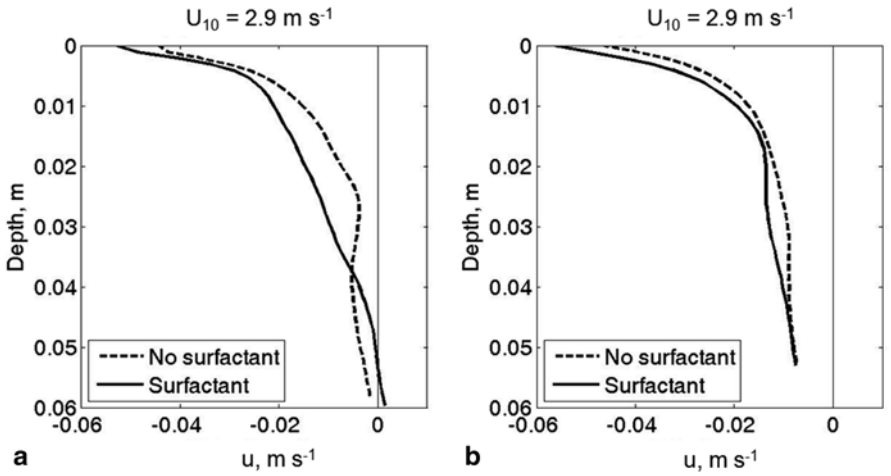

Fig. 2.15 Averaged velocity profiles from DPIV (along tank component) from experiments in ASIST: **a** Experiment 1, and **b** Experiment 2. We used oleic acid in Experiment 1 and oleyl alcohol in Experiment 2. (After Soloviev et al. (2011) by permission of Kyoto University Press)

layer near a ridged wall. These streaks are a type of coherent structures developing in the buffer layer between the viscous sublayer and the area of developed turbulence. Such streaks are observed between approximately $z_+ = 5$ and $z_+ = 40 - 50$, where $z_+ = z/(\nu/u_*), z$ is the distance to the surface, ν is the kinematic viscosity, and u_* is the friction velocity. The streaks near the ridged wall are of spanwise size of about 100 z_+ and of average length of 500 z_+ (Lesieur 2008).

Matt et al. (2011) reproduced the streak-like features reported in the laboratory experiment by Soloviev et al. (2011) using a computational fluid dynamcis (CFD) model. In the numeric model, viscoelastic surface boundary conditions were formulated as follows:

$$\tau_x = \tau_0 + \partial\sigma_w / \partial C \;\; \partial C / \partial x + \partial\sigma_w / \partial T \;\; \partial T / \partial x, \tag{2.8}$$

$$\tau_y = \partial\sigma_w / \partial C \;\; \partial C / \partial y + \partial\sigma_w / \partial T \;\; \partial T / \partial y, \tag{2.9}$$

The last two terms on the right side of (2.8) and (2.9) represent the dependence of surface tension σ_w on the surface concentration of surfactant (C) and on temperature (T). The model results revealed "streak-like" features in the velocity field (Fig. 2.16a). However, noticeable suppression of streaks occurred when the viscoelastic boundary conditions were activated (Fig. 2.16b).

Near rigid walls, the near-surface velocity streaks are subject to the Tollmien–Schlichting (TS) type instability leading to the development of 'hairpin vortices' and ejection of fluid from the viscous sublayer (Kim et al. 1987). A similar instabil-

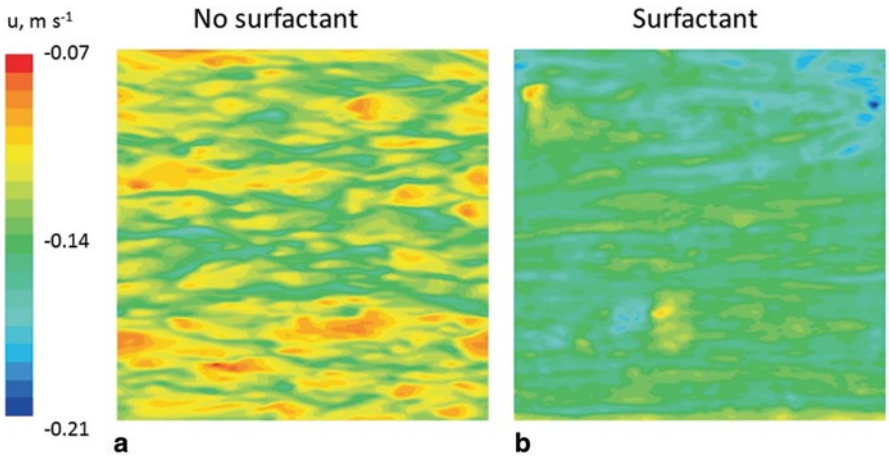

Fig. 2.16 Top view of along tank velocity without **a** and with **b** elastic boundary condition simulating surfactant effect. (After Matt et al. (2011) by permission of Kyoto University Press)

ity, though possibly not exactly of the same type as that near the rigid wall, can also develop near a flexible wall (Benjamin 1960, 1963) or a free surface (Caulleiz et al. 2008). In Chap. 5, we link this type of instability (resulting in fluid ejection from the near-surface layer) to 'ramp-like structures', which are an observable feature in turbulent boundary layers in the atmosphere (Antonia et al. 1979) and ocean (Thorpe 1985; Soloviev 1990). This type of coherent structure is responsible for about 40 % of the momentum transport across the boundary layer (Antonia et al. 1979).

Figure 2.17 shows average current velocity profiles from the numerical simulation of the Soloviev et al. (2011) laboratory experiment. The increase in the surface drift velocity observed in the presence of surfactants in the upper few centimeters of the water layer in the laboratory experiment (Fig. 2.15) is also seen in the numerical results (Fig. 2.17). This is a result of the suppression of turbulent velocity fluctuations and coherent structures due to the dilatational viscoelasticity of the monomolecular surface film, which is schematically illustrated in Fig. 2.18. The concentration of the surfactant in convergence zones reduces surface tension, while the dilution of the surfactant in divergence zones decreases surface tension. As a result, forces opposing fluid motion develop at the water surface and suppress coherent (as well as random) velocity fluctuations in the near-surface layer of water. A consequence of streak and turbulence suppression below the surface is the reduction of the drag coefficient from the waterside of the air–water interface, which explains the effect of surface drift velocity increase observed in the presence of surfactants.

Phongikaroon et al. (2004) demonstrated in a laboratory experiment that surfactants can modify SST by affecting dynamics of the millimeter thick aqueous thermal molecular sublayer (cool skin). The numerical simulations by Soloviev et al. (2012) demonstrate an effect on the temperature difference across the aqueous thermal molecular sublayer in the presence of surfactants during nighttime (Fig. 2.19) and daytime (Fig. 2.20). Note that under strong solar irradiance, "cool skin" turns into a "warm skin."

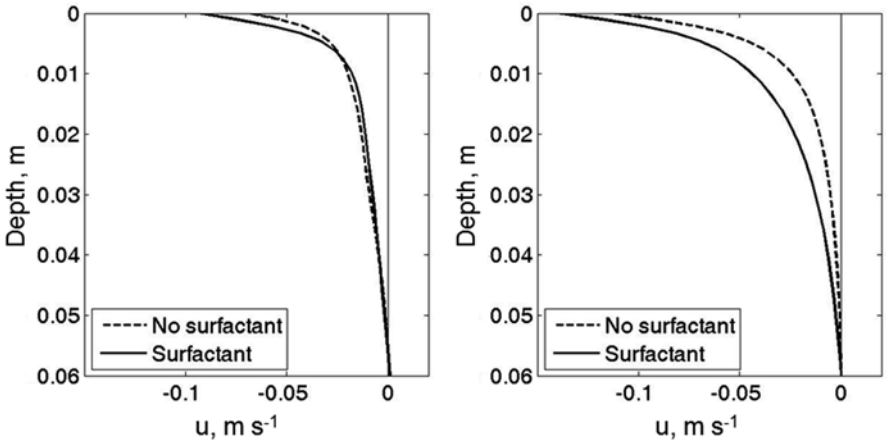

Fig. 2.17 Along tank velocity (u) referenced to $z = -0.06$ m (CFD model). (left) Large eddy simulation wall-adaptive local eddy viscosity model (LES-WALE), (right) detached eddy simulation (DES) model with realizable k-ε. Note increase of the surface drift velocity in the presence of surfactant. (After Soloviev et al. (2011) by permission of Kyoto University Press)

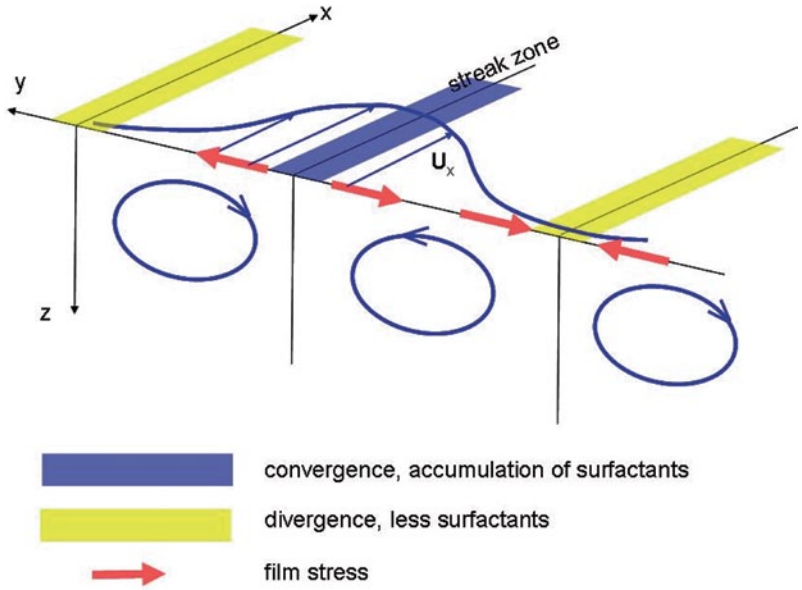

Fig. 2.18 Schematic representation of the effect of surfactants on near-surface circulation. (After Soloviev et al. (2011) by permission of Kyoto University Press)

During nighttime (Fig. 2.19), the temperature difference across the cool skin increased approximately by a factor of 2 in the presence of surfactant. During daytime, under conditions of strong solar radiation and light winds (Fig. 2.18), the presence of surfactants resulted in an increase in the temperature difference across the warm skin by approximately 25 %.

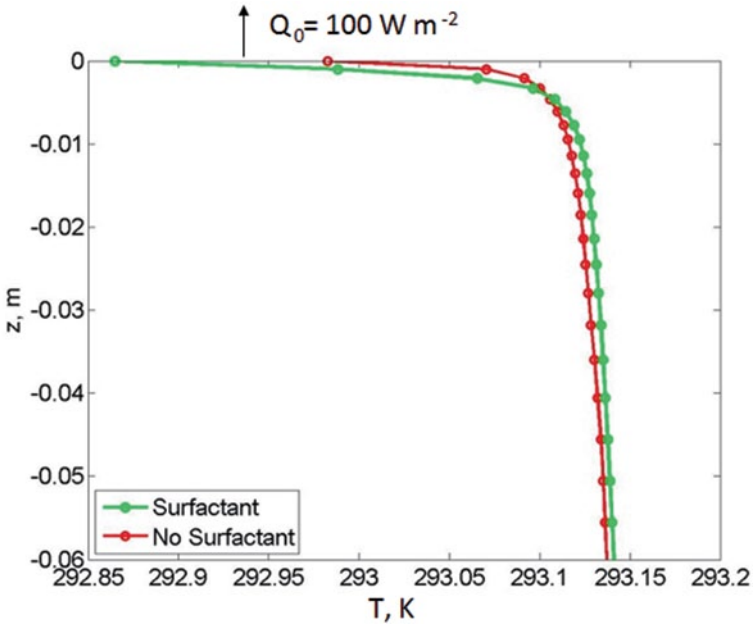

Fig. 2.19 Effect of surfactants on SST during nighttime calculated with CFD model at U_{10} = 4 ms^{-1}. Due to effect of surfactants, temperature difference across the cool skin ΔT changed from −0.15 K to −0.3 K. (After Soloviev et al. 2012)

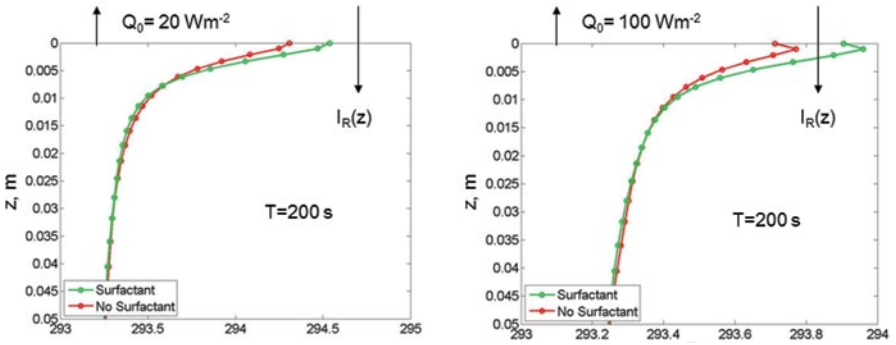

Fig. 2.20 Effect of surfactants on SST during daytime calculated with CFD Model at U_{10}= 1 ms^{-1}, $I_R(0)$ = 1200 Wm^{-2}. Under strong solar irradiance, "cool skin" turns into a "warm skin". (After Soloviev et al. 2012)

The effect of surfactants on SST may be comparable to the global change of SST during the last 30 years, when the satellite technology was introduced in the SST measurement.

The removal of surface films by convection, rain, near-surface shear, and breaking waves affects hydrodynamic processes at the air–sea interface, especially the capillary wave field, which substantially determines the surface roughness and thus air–sea exchanges. This process has a dual effect on the gravity-capillary wave field: It damps waves due to increased turbulence, and it enhances waves due to fragmentation and dissipation of surface films.

The lack of in situ measurements of the viscoelastic properties of films under various ocean regimes and particularly under different forcing conditions, limits the direct estimates of the global surface film effects on air–sea exchange. There are, however, indications that this uncertainty can be largely reduced if the mean square wave slope due to capillary-gravity waves is used rather than wind speed (Frew 1997). Glazman and Greysuku (1993) demonstrated the correlation between the surface wind stress and the sea surface roughness associated with capillary-gravity waves detected by backscattering from altimeters. This means that surface films may have less effect on the air–sea exchange parameterizations that are derived in terms of the mean square wave slope or friction velocity rather than in terms of the wind speed.

2.4 Parameterization of Molecular Sublayers During Nighttime Conditions

Conceptual models of the aqueous molecular sublayers can be divided into two classes: surface renewal models and boundary-layer models. In renewal models, the properties of molecular sublayers depend on the surface *renewal time*. The renewal time is then related to the environmental parameters causing hydrodynamic instabilities that control the properties of molecular sublayers. Boundary-layer models are based on the quasi-stationary representation of boundary-layer processes. We describe these modeling approaches in detail below. The effects of sea surface elasticity, however, have not yet been fully addressed in the parameterization of aqueous molecular sublayers.

2.4.1 Dimensional Analysis

Dimensional considerations can provide initial insight into the dynamics of aqueous molecular sublayers. Here, we ignore the bubble and droplet production in whitecaps and hence account for only interfacial (direct) heat, mass, and momentum transport. For the sake of simplicity, we also ignore here any explicit effects of surfactants (though, surfactant effects can enter the resulting parameterizations implicitly via modified empirical constants). In the case of steady meteorological and wave conditions, the following set of functional dependences can then be formulated:

$$\overline{\Delta u} = function(u_*, q_0, \alpha_T, g, \nu, \kappa_T, \sigma_w, \sigma_f, h) \tag{2.10}$$

$$\overline{\Delta T} = function(u_*, q_0, \alpha_T, g, \nu, \kappa_T, \sigma_w, \sigma_f, h) \tag{2.11}$$

$$K_\mu = function(u_*, q_0, \alpha_T, g, \nu, \mu, \kappa_T, \sigma_w, \sigma_f, h) \tag{2.12}$$

where $\Delta u = u_0 - u_b$ is the velocity difference across the aqueous viscous sublayer, u_b is the magnitude of the bulk (mixed layer) horizontal velocity, and u_0 is the magnitude of the sea surface velocity; $\Delta T = T_0 - T_b$ is the temperature difference across the cool skin, T_0 is the SST, and T_b is the temperature of the bulk (mixed layer); K_μ is the gas-transfer velocity defined by equation (1.50); $q_0 = Q_0 / (c_p \rho) = (Q_T + Q_E + I_L) / (c_p \rho)$ is the scaled net heat flux at the sea surface, Q_T is the sensible heat flux, I_L is the net longwave irradiance, Q_E is the latent heat flux; α_T is the coefficient of thermal expansion of water, g is the acceleration due to gravity, ρ is the water density, ν is the kinematic molecular viscosity, κ_T is the thermal molecular conductivity, σ_w is the surface tension of pure water, σ_s is the surface tension of water covered with film, $\sigma_f = \sigma_w - \sigma_s$ is the film pressure, μ is the coefficient of molecular gas diffusion; and h is the depth of the upper ocean mixed layer.

Since transport across molecular sublayers is intermittent, functional dependences in (2.10)–(2.12) are formulated for ensemble-averaged parameters. These relationships take into account the influence of thermally driven convection, wind-induced turbulence, and surface gravity and gravity-capillary waves on molecular sublayers. The effects of precipitation, solar radiation, and surfactants are ignored here but considered elsewhere in this chapter.

Choosing friction velocity in water (u_*) instead of wind speed reduces the uncertainty caused by surfactants (see discussion at the end of the previous section). The functional connection between the sea surface roughness associated with capillary-gravity waves and the wind stress ($\tau_0 = \rho u_*^2$) also simplifies the application of observational and theoretical results to remote sensing applications. Unfortunately, the replacement of wind speed with friction velocity does not solve the problem of surfactants completely, because the experimental friction velocities are often determined from wind-speed measurements and a bulk flux algorithm, normally ignoring any surfactant effects.

A standard dimensional analysis of functional dependences (2.10)–(2.12) leads to the following dimensionless relations:

$$\Delta \overline{u} / u_* = f_u(Rf_0, Ke, R_w, P_f, \mathrm{Pr}, Ra_h), \tag{2.13}$$

$$\Delta \overline{T} / T_* = f_T(Rf_0, Ke, R_w, P_f, \mathrm{Pr}, Ra_h), \tag{2.14}$$

$$K_\mu / u_* = f_C(Rf_0, Ke, R_w, P_f, \mathrm{Pr}, Sc, Ra_h), \tag{2.15}$$

where $T_* = q_0 / u_*$; f_u, f_T, and f_C are nondimensional functions of their nondimensional arguments; $\mathrm{Pr} = \nu / \kappa_T$ is the Prandtl number, $Sc = \nu / \mu$, $Ra_h = -\alpha_T g q_0 h^4 / (\nu \kappa_T{}^2)$, $Rf_0 = \alpha_T g q_0 \nu / u_*^4$, $Ke = u_*^3 / (g\nu)$, $R_w = u_* / \left(g\sigma_s / \rho\right)^{1/4}$, and $P_f = u_*{}^4 / \left[g(\sigma_w - \sigma_s)/\rho\right]^{1/4}$ (we identify the last four numbers a little bit later in this section).

In the upper ocean the Rayleigh number Ra_h is usually very large. It is well known that in a fully developed turbulent flow, parameters of a molecular boundary layer no longer explicitly depend upon the external scale of the flow. It has been customary in such cases to hypothesize self-similarity for the Ra_h number; this dimensionless number respectively drops out of the number of determining parameters. Dimensionless relationships (2.13)–(2.15) reduce to

$$\Delta\bar{u} / u_* = F_u(Rf_0, Ke, R_w, P_f, \mathrm{Pr}), \tag{2.16}$$

$$\Delta\bar{T} / T_* = F_T(Rf_0, Ke, R_w, P_f, \mathrm{Pr}), \tag{2.17}$$

$$K_\mu / u_* = F_C(Rf_0, Ke, R_w, P_f, \mathrm{Pr}, Sc), \tag{2.18}$$

where F_u, F_T, and F_C are the universal functions of nondimensional arguments Rf_0, Ke, Pr, R_w, P_f, and Sc (in case of the gas-transfer velocity only).

Parameters Sc and Pr entering (2.16)–(2.18) are the Schmidt and Prandtl numbers, respectively, which are well known from the classical boundary-layer theory. Four other dimensionless numbers, Rf_0, Ke, R_s, and P_f are less known but are also important for the physics of aqueous molecular sublayers at the air–sea interface.

The parameter Rf_0 proposed by Kudryavtsev and Soloviev (1985) determines the transition from convective to shear instability of aqueous molecular sublayers. From the definition of the flux Richardson number in the near-surface layer of the ocean $Rf = \alpha_T g q_0 \rho / \left(\tau_{xz}\partial u/\partial z + \tau_{yz}\partial v/\partial z\right)$ and from the expression for the momentum flux within the viscous sublayer $\tau_{xz} = \tau_{x0} = \rho\nu\partial u/\partial z$ and $\tau_{yz} = \tau_{y0} = \rho\nu\partial v/\partial z$ (also using relation $\tau_0 = \rho u_*^2 = \left(\tau_{x0}^2 + \tau_{y0}^2\right)^{1/2}$), the following expression for the flux Richardson number in the viscous sublayer follows:

$$Rf\Big|_{-z<\delta_\nu} = \alpha_T g q_0 \nu / u_*^4 = Rf_0, \tag{2.19}$$

where δ_ν is the thickness of the viscous sublayer. Since Rf_0 appears to be the surface asymptote of Rf, Kudrayvtsev and Soloviev (1985) named this parameter the *surface Richardson number*. For convectively unstable conditions Rf_0 is negative because $\alpha_T q_0 < 0$.

The parameter $Ke = u_* / (g\nu)$ determines the transition to whitecapping at the air–sea interface. Csanady (1990) named this parameter the *Keulegan number*. As emphasized in Sect. 2.3.3, it is a fundamental parameter in the dynamics of free interfaces.

The effect of surface tension on aqueous molecular sublayers is associated with two nondimensional numbers, $R_w = \rho u_*^4 / (g\sigma_w)$ and $P_f = g(\sigma_w - \sigma_s)/(\rho u_*^4)$. The R_w number is assumed to be a determining parameter in direct disruption of the air–sea interface under very strong wind-speed conditions (and possibly in the process of microscale wave breaking under moderate wind-speed conditions). This number is linked to the *Koga number* as follows $R_w = (\rho/\rho_a)^2 Ko^4$. Note that the Koga number, *Ko*, introduced by Soloviev and Lukas (2010) is a characteristic of the Kelvin–Helmholtz (KH) instability at the air–water interface (see Sect. 6.3.4). The dimensionless number P_f is related to the effect of surfactants.

Specification of dependences (2.16)–(2.18) via Rf_0, *Ke*, *Pr*, and *Sc* is now possible within the framework of the physical models considered in the next sections. To our best knowledge, no explicit dependence on R_w and P_f has ever been included in the parameterization of aqueous molecular sublayers. Reasonable assumptions are that P_f is important for low winds only, while R_w is essential for hurricane conditions predominately.

2.4.2 Renewal Model

The renewal concept follows from the idea of intermittent transport of properties across molecular sublayers. Kim et al. (1971) found that the turbulent momentum transport and production in a wall layer take place intermittently in time and space through small-scale bursting motions.

The renewal model developed by Liu and Businger (1975) is based on the Kim et al. (1971) result and considers intermittent transport of properties across molecular sublayers. Liu and Businger (1975) developed a method for calculation of average temperature profiles in molecular sublayers by assuming that the sublayers undergo cyclic growth and subsequent destruction. Kudryavtsev and Soloviev (1985) parameterized the transition from free to forced convection in the cool skin using the surface Richardson number Rf_0 as the determining parameter. Soloviev and Schluessel (1994) incorporated a Keulegan number (*Ke*) dependence for high wind-speed conditions and developed a coupled parameterization for the temperature difference across the cool skin of the ocean and the air–sea gas-transfer velocity.

Further developing the surface renewal model and following Liu and Businger (1975), Soloviev and Schlüssel (1994) and Soloviev (2007), considered a fluid element adjacent to the sea surface. Initially, it had a uniform velocity u_w, temperature T_w, and the concentration of scalar property C_w equal to the corresponding bulk-water value. As the fluid element is exposed to the interface, the appropriate molecular diffusion laws (1.6), (1.10), and (1.12) govern the velocity (Δu) and temperature (ΔT) differences, and the interfacial gas flux (G_o). Under assumption of horizontal homogeneity, no insolation, and no rain, one-dimensional molecular diffusion laws are as follows:

$$\frac{\partial u}{\partial t} = \frac{\partial}{\partial z}\left(\nu \frac{\partial u}{\partial z}\right), \tag{2.20}$$

$$\frac{\partial T}{\partial t} = \frac{\partial}{\partial z}\left(\kappa_T \frac{\partial T}{\partial z}\right), \tag{2.21}$$

$$\frac{\partial C}{\partial t} = \frac{\partial}{\partial z}\left(\mu \frac{\partial C}{\partial z}\right). \tag{2.22}$$

The classic error-function integral solutions of equations (2.20)–(2.22) result in the following dependences:

$$\Delta u(t) = 2\pi^{-1/2}(t/\nu)^{1/2}\tau_t/\rho, \tag{2.23}$$

$$\Delta T(t) = -2\pi^{-1/2}(t/\nu)^{1/2} q_0, \tag{2.24}$$

$$G_0(t) = \pi^{-1/2}(t/\mu)^{-1/2}\Delta C, \tag{2.25}$$

where $\Delta u(t) = u_0(t) - u_w$, $\Delta T(t) = T_0(t) - T_w$, t is the elapsed time, vertical coordinate z is related to the instantaneous position of the sea surface (uncertain during wave-breaking events), and π=3.14. Note that in (2.23)–(2.24) the evolutions of the velocity and temperature differences are considered under conditions of constant tangential stress τ_t and scaled heat flux q_0, respectively, while in (2.25) the gas flux evolution is considered under conditions of constant gas concentration difference across the diffusion sublayer, $\Delta C = C_w - C_0$, which is assumed to be close to effective air–sea concentration difference.

Wind-induced surface current constitutes only a tiny part of the total velocity difference between air and sea (about 2 %). The condition of constant momentum flux rather than constant velocity difference is therefore appropriate in (2.23). Waves are a volume source of momentum in the near-surface layer of the ocean; formally, they do not enter the surface boundary condition for velocity. We nevertheless neglect here the second-order effect relating to the modification of the gravity-capillary waves and, thereby, the surface roughness and momentum fluxes by surface drift current. This secondary effect, however, may become of primary importance under conditions of very high wind speed (see Chap. 6).

The dependence of the net longwave irradiance I_L and latent heat flux Q_E on the temperature difference due to the cool skin is typically within several percent (Paulson and Simpson 1981). Only Q_T may depend appreciably on the cool-skin presence. Usually $|I_L + Q_E| >> |Q_T|$, which means that the net surface flux, q_0, does not depend strongly on the cool-skin presence. As a result, the condition of constant heat flux is justified for deriving dependence (2.24). Solar radiation is a volume

source of heat for the near-surface layer of the ocean and does not enter the surface boundary condition.

The condition of constant concentration difference accepted in (2.25) follows from the fact that the aqueous diffusion sublayer provides the main resistance to the gas transfer (Bolin 1960) and thereby contains the main gas concentration difference across the air–sea interface.

The average velocity and temperature difference across the aqueous viscous and thermal sublayers and the average surface gas flux at the air–sea interface can be defined as follows:

$$\overline{\Delta u} = \int_0^\infty p(t) t^{-1} \left(\int_0^t \Delta u(t') dt' \right) dt \tag{2.26}$$

$$\overline{\Delta T} = \int_0^\infty p(t) t^{-1} \left(\int_0^t \Delta T(t') dt' \right) dt \tag{2.27}$$

$$\overline{G_0} = \int_0^\infty p(t) t^{-1} \left(\int_0^t G_0(t') dt' \right) dt \tag{2.28}$$

where $p(t)$ is the probability density for time periods, t, of bursting motions in the molecular sublayers. This is the probability of local destruction of the molecular sublayers in a time interval $(t, t+dt)$, where t is the elapsed time since the previous destruction.

The experiments of Rao et al. (1971) on the structure of the boundary layer turbulence indicate that the time between bursts is distributed according to a lognormal law. The probability density for such a process is given by

$$p(t) = \pi^{-1/2} (\sigma t)^{-1} \exp\left[-(\ln t - m)^2 / \sigma^2 \right], \; t > 0, \tag{2.29}$$

where m is the mean value and σ^2 is the variance for the logarithm of the random variable t. Garbe et al. (2002) found the lognormal distribution (2.29) as being in good agreement with the histogram of time intervals between two successive renewal events derived from infrared images in a laboratory tank (Fig. 2.21).

Inserting (2.29) into relationships (2.26)–(2.28), we obtain

$$\overline{\Delta u} = (4\pi^{-1/2} / 3) \exp(-\sigma^{2/16}) (t_* / \nu)^{1/2} \tau_t, \tag{2.30}$$

$$\overline{\Delta T} = -(4\pi^{-1/2} / 3) \exp(-\sigma^{2/16}) (t_* / \kappa_T)^{1/2} q_0, \tag{2.31}$$

$$K_\mu = 2\pi^{-1/2} \exp(3\sigma^2 / 16) (t_* / \mu)^{-1/2}, \tag{2.32}$$

where K_μ is the gas-transfer velocity (the piston velocity) defined by equation (1.44), and $t_* = \exp(m + \sigma^2 / 4)$ is the average time between bursts, which has been

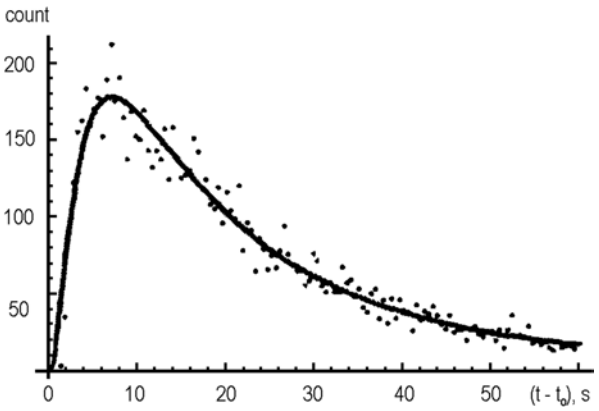

Fig. 2.21 Lognormal distribution (2.29) fitted to the histogram of the time between two consecutive surface renewal events $t - t_0$ for a wind speed of 2 m s^{-1}. (After Garbe et al. 2002. Reproduced by permission of American Geophysical Union)

referred to as the renewal time. Since the bursting events have significant energy, we assume that they affect the viscous, thermal, and diffusion molecular sublayers in the same manner, and the quantity σ^2 in (2.30)–(2.32) is the same.

Soloviev and Schlüssel (1994) considered three wind-speed regimes:

1. Calm and low wind-speed conditions: The cyclic injection of fluid from the molecular sublayers is of convective nature. The time period of the convective bursts is defined by Foster (1971) as follows:

$$t_c = a_c(-\nu / \alpha_T g q_0)^{1/2}, \tag{2.33}$$

where a_c is a dimensionless coefficient.

2. Intermediate wind-speed conditions: According to Csanady (1990), the most intense surface renewal on a wind-blown surface is caused by viscous surface-stress variations associated with rollers on breaking wavelets. The time period of these variations is defined as

$$t_r = a_r \nu / u_*^2, \tag{2.34}$$

where a_r is a dimensionless constant.

3. High wind-speed conditions: Surface waves take most of the wind stress and the development of rollers is less probable. The surface renewal due to waves breaking and whitecapping dominates. For fully developed wind waves, the timescale of the surface renewal depends on the parameters u_* and g. A dimensional analysis leads to the following relation:

$$t_w = a_w u_*^2 / g, \tag{2.35}$$

where a_w is a dimensionless constant.

The surface Richardson number (Rf_0) controls the transition from free convection (regime 1) to rollers (regime 2) at the air–sea interface, while the Keulegan number (Ke) controls the transition from rollers (regime 2) to wave breaking (regime 3). Combining (2.33), (2.34), and (2.35), the renewal (or exposure) time can then be expressed as follows:

$$t_* = \begin{cases} a_c \left[\nu / (-\alpha_T g q_0)^{1/2} \right] \text{ at } 0 \le u_* \le (\alpha_T g q_0 \nu / Rf_{cr})^{1/4} \\ a_r \nu / u_*^2 \quad \text{at } (\alpha_T g q_0 \nu / Rf_{cr})^{1/4} \le u_* \le (Ke_{cr} \nu g)^{1/3} \\ a_w u_* / g \quad \text{at } u_* \ge (Ke_{cr} \nu g)^{1/3} \end{cases} \tag{2.36}$$

where Rf_{cr} and Ke_{cr} are the critical values of the surface Richardson number and the Keulegan number, respectively. In dimensionless form, formula (2.36) is as follows:

$$t_* / (a_r \nu / u_*^2) = \begin{cases} (Rf_0 / Rf_{cr})^{-1/2} \text{ at } Rf_0 / Rf_{cr} \ge 1 \\ 1 \text{ at } Rf_0 / Rf_{cr} \le 1 \text{ and } Ke / Ke_{cr} \le 1 \\ Ke / Ke_{cr} \text{ at } Ke / Ke_{cr} \ge 1 \end{cases} \tag{2.37}$$

where $Rf_{cr} = -(a_c / a_r)^2$ and $Ke_{cr} = a_r / a_w$.

Formula (2.37) can be approximated in the following way:

$$t_* / (a_r \nu / u_*^2) = (1 + Rf_0 / Rf_{cr})^{-1/2} (1 + Ke / Ke_{cr}), \tag{2.38}$$

which is a sufficiently accurate and convenient analytical expression. An interpretation of the Ke-number dependence in (2.38) is that under high wind-speed conditions the tangential stress τ_t relates to the total wind stress τ_0 according to (2.8).

Inserting the renewal time (2.38) into (2.30)–(2.32) and taking into account (2.8) and the definition of the friction velocity $u_* = (\tau_0 / \rho)^{1/2}$ leads to the following coupled set of parametric relationships:

$$\overline{\Delta u} / u_* = \Lambda_0 (1 + Rf_0 / Rf_{cr})^{-1/4}, \tag{2.39}$$

$$\overline{\Delta T} / T_* = -\Lambda_0 \, \mathrm{Pr}^{1/2} (1 + Rf_0 / Rf_{cr})^{-1/4} (1 + Ke / Ke_{cr})^{1/2}, \tag{2.40}$$

$$K_\mu / u_* = A_0 \Lambda_0^{-1} Sc^{-1/2} (1 + Rf_0 / Rf_{cr})^{1/4} (1 + Ke / Ke_{cr})^{-1/2}, \tag{2.41}$$

where $T_* = q_0 / u_*$, $\mathrm{Pr} = \nu / k$, and $Sc = \nu / \mu$. The dimensionless coefficients A_0 and Λ_0 are expressed through the parameter of lognormal distribution (2.29) as follows:

$$A_0 = \left(8\pi^{-1} / 3\right) \exp\left(\sigma^2 / 8\right), \tag{2.42}$$

Table 2.1 Parameter σ in (2.29) from the results of Garbe et al. (2002) and the computation of coefficient A_0 from equation (2.42)

Wind speed, m s^{-1}	2.0	4.2	8.0
σ	1.39	0.8	0.7
A_0	1.08	0.92	0.89

$$\Lambda_0 = \left(4\pi^{-1/2}/3\right)\exp\left(-\sigma^2/16\right)a_r^{1/2}. \tag{2.43}$$

The calculation of A_0 with σ determined from the Garbe et al. (2002) laboratory experiment is presented in Table 2.1.

For low wind-speed conditions, $Rf_0 \to \infty$ and $Ke \to 0$; equations (2.39)–(2.41) have the following asymptotes:

$$\overline{\Delta u} \approx \Lambda_0 u_* \left(\frac{Rf_0}{Rf_{cr}}\right)^{-1/4} = \Lambda_0 u_*^2 \left(\frac{Rf_{cr}}{\alpha_T g q_0 \nu}\right)^{1/4}, \tag{2.44}$$

$$\Delta T \approx -\Lambda_0 \,\mathrm{Pr}^{1/2} \left(\frac{Rf_0}{Rf_{cr}}\right)^{-1/4} \frac{q_0}{u_*} = -\Lambda_0 \,\mathrm{Pr}^{1/2} \left(\frac{Rf_{cr}}{\alpha_T g \nu q_0}\right)^{1/4} q_0, \tag{2.45}$$

$$K_\mu \approx A_0 \Lambda_0^{-1} Sc^{-1/2} u_* \left(\frac{Rf_0}{Rf_{cr}}\right)^{1/4} = A_0 \Lambda_0^{-1} Sc^{-1/2} \left(\frac{\alpha_T g \nu q_0}{Rf_{cr}}\right)^{1/4}. \tag{2.46}$$

Remarkably, formula (2.45) is similar to that of Katsaros et al. (1977),

$$\overline{\Delta T} = a_0^{-3/4} \left(\frac{\nu}{-\alpha_T g \kappa_T^2}\right)^{1/4} q_0^{3/4}, \tag{2.47}$$

obtained for calm weather conditions; the appropriate nondimensional coefficients are interrelated by

$$a_0 = \Lambda_0^{-4/3} \left(-Rf_{cr}\right)^{-1/3}. \tag{2.48}$$

For moderate wind-speed conditions, which is an intermediate asymptotic $|Rf_0| << |Rf_{cr}|$ and $Ke << Ke_{cr}$, parameterizations (2.39)–(2.41) reduce to

$$\overline{\Delta u} = \Lambda_0 u_*, \tag{2.49}$$

$$\overline{\Delta T} \approx -\Lambda_0 \,\mathrm{Pr}^{1/2} T_* = -\Lambda_0 \,\mathrm{Pr}^{1/2} q_0 / u_*, \tag{2.50}$$

$$K_\mu = A_0 \Lambda_0^{-1} Sc^{-1/2} u_*. \tag{2.51}$$

There is presumably no direct analog of (2.49) in the literature. Formula (2.50) has an analog previously derived by Saunders (1967b)

$$\overline{\Delta T} = -\lambda_S \, \mathrm{Pr} \, q_0 / u_*, \tag{2.52}$$

while the formula similar to (2.51),

$$K_\mu = \gamma_0 Sc^{-1/2} u_*, \tag{2.53}$$

can be found in several previous publications on air–sea gas exchange. The dimensionless coefficients entering (2.50) and (2.52) are interrelated by $\lambda_S = \Lambda_0 \, \mathrm{Pr}^{-1/2}$ and $\gamma_0 = A_0 \Lambda_0^{-1}$.

For high wind-speed conditions, equations (2.39)–(2.41) have asymptotes $|Rf_0| << |Rf_{cr}|$ and $Ke >> Ke_{cr}$, which lead to:

$$\overline{\Delta u} = \Lambda_0 u_*, \tag{2.54}$$

$$\overline{\Delta T} \approx -\Lambda_0 \, \mathrm{Pr}^{1/2} T_* (Ke / Ke_{cr})^{1/2} = -\Lambda_0 \, \mathrm{Pr}^{1/2} (\nu g Ke_{cr})^{-1/2} q_0 u_*^{1/2}, \tag{2.55}$$

$$K_\mu \approx A_0 \Lambda_0^{-1} Sc^{-1/2} u_* (Ke / Ke_{cr})^{-1/2} = A_0 \Lambda_0^{-1} Sc^{-1/2} (\nu g Ke_{cr})^{1/2} u_*^{-1/2}, \tag{2.56}$$

Same as for (2.49), no direct analog to (2.54) could be found in literature. Parameterization for the velocity difference across the aqueous viscous sublayer is closely related to the problem of determining the wind-drift coefficient; related issues are considered elsewhere in this section. High wind-speed parameterizations for the temperature difference across the cool skin and the gas-transfer velocity (2.55) and (2.56) were previously derived by Soloviev and Schlüssel (1994). Note that in this chapter we do not consider hurricane conditions and respectively assume any explicit dependence on R_w.

Active breaking events (whitecaps) occupy a relatively small area of the sea surface. In the process of wave breaking, molecular sublayers are destroyed, however they are restored in between wave-breaking events. In accordance with (2.8), a reduced fraction of the momentum flux transfers to tangential stress at higher wind speeds. As a result, the velocity difference is maintained proportional to the friction velocity (2.54). The temperature difference across the cool skin slightly increases with wind speed (2.55), while the interfacial gas-transfer velocity slightly decreases. Equations (2.54)–(2.56), however, do not include two important effects associated with wave breaking: 1) The residual turbulence after wave breaking maintains for several wave periods, affecting the molecular sublayers; 2) bubble production in whitecaps can substantially affect the air–sea gas exchange. The effect of the

residual wave-breaking turbulence on the interfacial gas transport (as well as the inclusion of the bubble-mediated gas transport) is discussed in Chap. 7 of this book.

Bubble-mediated heat transport is apparently negligible in comparison with the direct flux at the ocean–air interface, due to the low heat capacity of air inside the bubbles. In contrast, droplet and spray production by breaking waves is an important mechanism of the air–ocean heat and mass transport at wind speeds greater than about 15–17 m s^{-1} (Chap. 6).

Substituting (2.48) into (2.39)–(2.41), we obtain a coupled set of parameterizations:

$$\Delta\overline{u} / u_* = \Lambda_0 (1 - a_0{}^3 \Lambda_0^4 Rf_0)^{-1/4} \tag{2.57}$$

$$\Delta\overline{T} / T_* = -\Lambda_0 \,\mathrm{Pr}^{1/2} (1 - a_0{}^3 \Lambda_0^4 Rf_0)^{-1/4} (1 + Ke / Ke_{cr})^{1/2} \tag{2.58}$$

$$K_\mu / u_* = A_0 \Lambda_0^{-1} Sc^{-1/2} (1 - a_0{}^3 \Lambda_0^3 Rf_0)^{1/4} (1 + Ke / Ke_{cr})^{-1/2} \tag{2.59}$$

Replacing the surface cooling $Q_0 = Q_E + Q_T + I_L$ with the *virtual cooling*, which includes the buoyancy effects of salinity due to evaporation

$$Q_v = Q_E + Q_T + I_L + \frac{S_0 \beta_S c_p}{\alpha_T L} Q_E, \tag{2.60}$$

the expression for the surface Richardson number transforms in the following way:

$$Rf_0 = \frac{\alpha_T g \nu}{c_p \rho u_*^4} \left(Q_E + Q_T + I_L + \frac{\beta_S S_0 c_p}{\alpha_T L} Q_E \right). \tag{2.61}$$

Coefficients Λ_0, a_0, Ke_{cr}, and A_0 are now to be determined from the comparison with experimental data.

From the comparison with Grassl's (1976) data, which represented a relatively small number of field observations, Kudrayvtsev and Soloviev (1985) derived tentative estimates of the two constants $\Lambda_0 \approx 13.3$ and $Rf_{cr} \approx -1.5 \cdot 10^{-4}$, treating them as independent constants. From relationship (2.48) it then follows that $a_0 \approx 0.6$, which is much bigger than the commonly accepted estimate $a_0 = 0.25$ (Fedorov and Ginzburg 1988).

Since the publication of the Kudryavtsev and Soloviev (1985) work, new laboratory data sets on the surface wind-drift current using particle image velocimetry and infrared imaging have been obtained, which allow us to specify more accurately numerical constant Λ_0. Formulation (2.57)–(2.59) including constants Λ_0 and a_0 is more convenient than formulation (2.39)–(2.41) including constants Λ_0 and Rf_{cr}, because it is believed that, in contrast to Rf_{cr}, the numerical value of a_0 can be determined with an acceptable accuracy from laboratory experiments. A complication

is that a_0 depends on the presence of surfactants, which is characterized by the P_f number. The exact functional dependence, however, is not known.

It is also remarkable that according to (2.57) the dimensionless ratio $\overline{\Delta u}/u_*$ does not depend on the Keulegan number, which means that constant Λ_0 can be estimated from the experimental data on the surface wind-drift current. According to (2.49) and (2.54), for intermediate and high wind-speed conditions $\Lambda_0 = \overline{\Delta u}/u_*$. We assume that there is no explicit dependence of Λ_0 on R_w, since we do not consider in this analysis hurricane force winds.

The ratio, $\overline{\Delta u}/u_*$, is closely related to the *wind-drift coefficient*, u_0/U_{10}, where u_0 is the averaged current velocity at the sea surface (relative to the background ocean current), and U_{10} is the wind speed at 10 m height. The current velocity at the sea surface includes the Stokes drift as well, which provides a relatively small (between 5 and 20 %) contribution to the wind-drift coefficient however. The difference between the current velocity at the sea surface u_0 and the Stokes surface drift u_S is the wind-induced surface drift:

$$u_{wd} = u_0 - u_S. \tag{2.62}$$

The ratio between the wind-induced surface drift u_{wd} and the water friction velocity u_* as measured by Wu (1975) varied between 11 and 20. Wu (1975) concluded that $\langle u_{wd}/u_* \rangle \approx 17.0$ and has no obvious systematic dependence upon friction velocity. Phillips and Banner (1974) laboratory experiment indicated that $\langle u_{wd}/u_* \rangle \approx 16.1$.

Values of u_{wd}/u_* derived from particle image velocimetry and from infrared imaging also demonstrate no obvious dependence on the friction velocity but consistently indicate smaller surface drift currents than those derived from drifter measurements (Zhang and Harrison 2004). The wind-induced velocities derived from the infrared images are shown in Fig. 2.22. Averaging over all friction velocities results in $\langle u_{wd}/u_* \rangle \approx 7.4$. Based on these laboratory results we accept an estimate $\Lambda_0 \approx 7.4$. This is in fact an upper estimate, because it does not take into account the existence of relatively small current velocity difference across the turbulent layer (i.e., below the viscous sublayer).

A fit of parameterization (2.57) to the results of the Zhang and Harrison (2004) is shown in Fig. 2.22. In (2.57) the term $(1 - a_0^3 \Lambda_0^4 R f_0)^{-1/4}$ relating to buoyancy effects is of importance under low wind-speed conditions. Figure 2.22 therefore shows parameterization (2.39) for two values of the net surface heat flux Q_0.

A tentative estimate of $Ke_{cr} \approx 0.18$ was derived by Soloviev and Schlüssel (1994) from indirect data—the critical wind speed, $U_{10} \approx 10$ m s^{-1}, at which, according to the visual Beaufort scale, longwave breaking sets in. Later, Zhao and Toba (2001) proposed a parameter $R_B = u_{*a}^2/(\nu_a \omega_p)$ with a critical value of $R_B = 10^3$ for the onset of wind–wave breaking. Parameter R_B can be rewritten as

$$R_B = A_w u_{*a}^3/(g\nu_a) \tag{2.63}$$

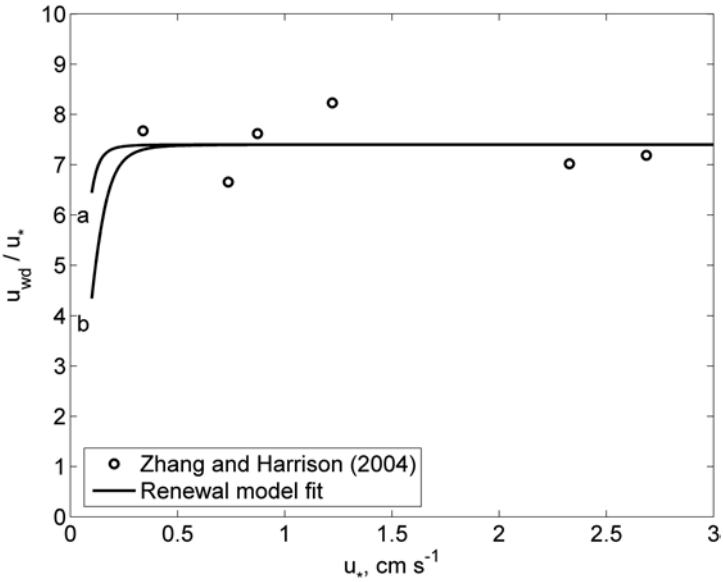

Fig. 2.22 Non-dimensional wind-induced surface current in the laboratory tank for different wind friction velocities and in comparison with the renewal model (2.57) at $a = 0.25$ and $\Lambda_0 = 7.4$, calculated for two surface cooling rates: **a** $Q_0 = 20$ W m^{-2}, and **b** $Q_0 = 200$ W m^{-2}

where A_w is the wave age defined as $A_w = g / \left(\omega_p u_{*a}\right) = c_p / u_{*a}$. The Keulegan number appears to be connected to the Zhao and Toba (2001) nondimensional parameter R_B as follows:

$$Ke = \frac{u_*^3}{g\nu} = \frac{u_{*a}^3}{g\nu_a}\frac{\nu_a}{\nu}\left(\frac{\rho_a}{\rho}\right)^{3/2}\frac{1}{A_w} = R_B\frac{\nu_a}{\nu}\left(\frac{\rho_a}{\rho}\right)^{3/2}\frac{1}{A_w}. \tag{2.64}$$

From (2.64), it follows that critical value $R_B = 10^3$ corresponds to $Ke_{cr} = 0.18$ at $A_w = 3.25$.

During TOGA COARE, Hartmut Grassl collected substantial statistics on the temperature difference across the cool skin in the western equatorial Pacific. Figure 2.23 shows parameterization (2.58) plotted for $a_0 = 0.25$, $\Lambda_0 \approx 7.4$, and wave $A_w = 15$ in comparison with the TOGA COARE data set collected during nighttime. The wave age of $A_w = 15$ corresponds to developed wind waves, which are often observed in the open ocean. There is a reasonable agreement between the COARE data set and the renewal-type model.

Horrocks et al. (2002) collected a large data set on the cool skin in the western tropical and subtropical Pacific using a scanning infrared SST radiometer. Comparison of parameterization (2.56) with the Horrocks et al. (2006) data set has also shown a reasonable correlation (Soloviev et al. 2007).

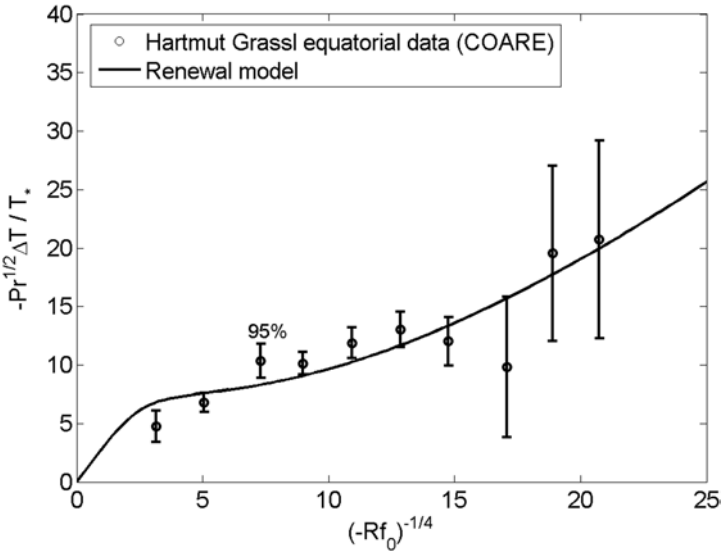

Fig. 2.23 Nighttime cool skin data of Hartmut Grassl obtained in the western equatorial Pacific during TOGA COARE in comparison with renewal model. (After Soloviev 2007 by permission of Elsevier)

Figure 2.24 compares results of direct, eddy-correlation measurements of the CO_2 air–sea flux during *GasEx-01* collected by Hare et al. (2004) with renewal model (2.59). According to Table 2.1, constant A_0 entering the gas-exchange parameterization is close to unity, varying within $\pm 10\%$ as a function of wind speed. For simplicity, we take $A_0 = 1$. The bubble-mediated contribution to the gas-transfer velocity for CO_2 according to the model of Woolf (1997) is shown in Fig. 2.24a. The resultant curve demonstrated in Fig. 2.24b suggests a good agreement between model and observations encouraging further exploration of the applicability of the renewal model for parameterization of the air–sea gas exchange.

Figure 2.25 shows a summary of gas-transfer results over the ocean. The theoretical dependencies correspond to the sum of an interfacial component (renewal model (2.57)) and Woolf's (1997) bubble-mediated component. Both theoretical relationships and field data are color-coded. Blue color indicates low-solubility gases (SF6 and 3He); red color indicates higher solubility gases (Rn and CO_2), and black color is reserved for a well soluble gas (DMS). Under high wind-speed conditions, theoretical curves for different gases diverge but appear to be consistent with the available data.

The renewal model also appears to be useful for parameterizing salinity difference in the aqueous haline diffusion sublayer at the air–sea interface (Fedorov and Ginzburg 1988). Zhang and Zhang (2012) estimated this difference to reach up to 0.3 psu in some regions of the ocean, though being localized in the upper 0.1–0.2 mm layer of the ocean.

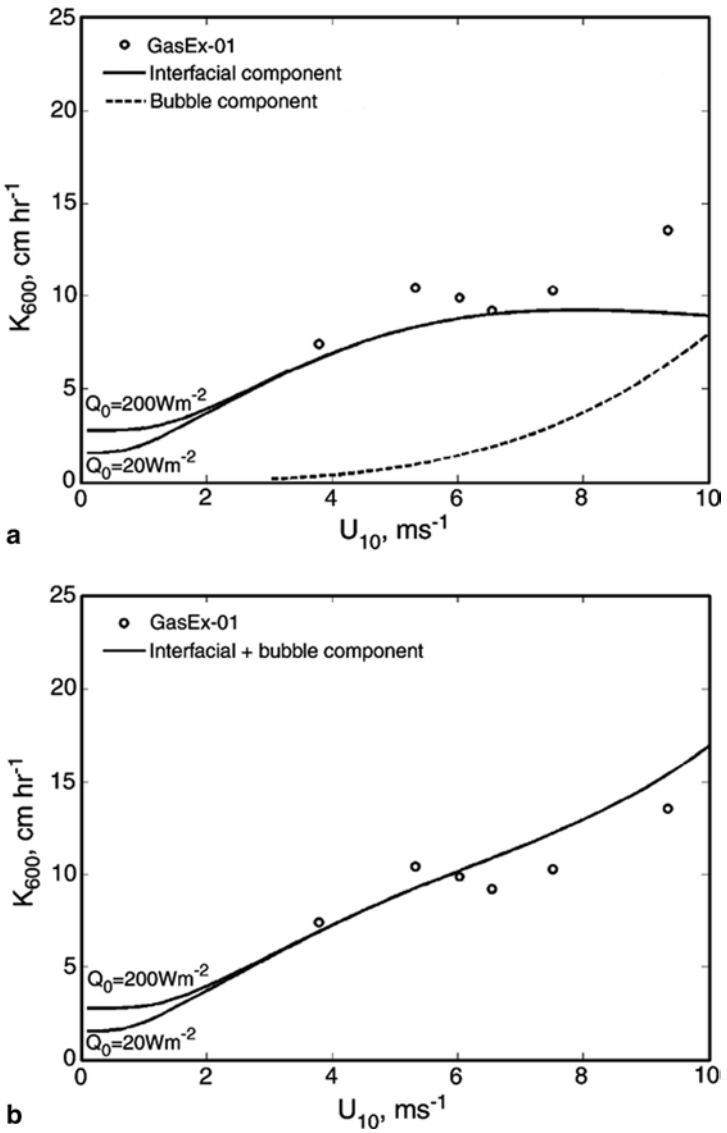

Fig. 2.24 **a** Comparison of the renewal type (interfacial) parameterization (20) for two values of the surface heat flux Q_0 with direct measurements of the CO_2 transfer velocity during GasEx-2001 (Hare et al. 2004). Woolf's (1997) parameterization of the bubble-mediated component is shown with a dashed line. **b** Sum of the interfacial and bubble mediated parameterizations in comparison with the GasEx-2001 data. (After Soloviev 2007 by permission of Elsevier)

2.4.3 Boundary-Layer Model

Though boundary-layer models operate with the averaged turbulent characteristics such as the dissipation rate ε (for instance, defining the viscous sublayer depth as

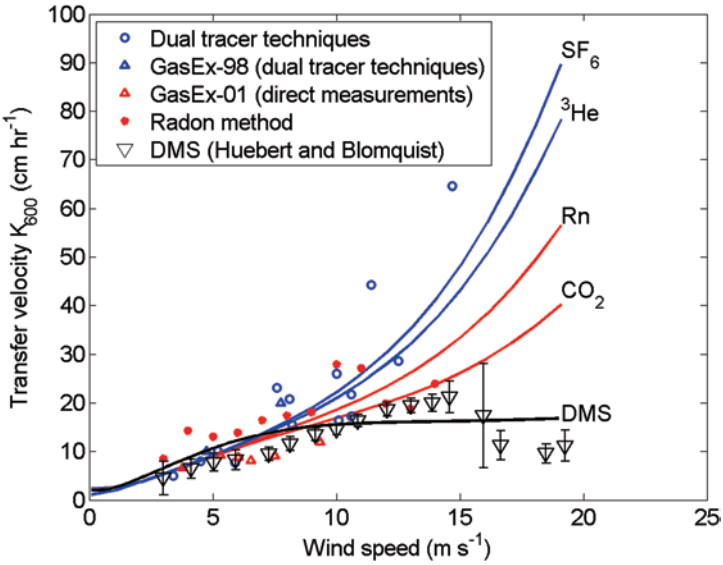

Fig. 2.25 Renewal gas-transfer parameterization in comparison with field data. The dual tracer data are from Wanninkhof et al. (1997), Asher and Wanninkhof (1998), and Nichtingale et al. (2000). The radon data are from Peng et al. (1974), Peng et al. (1979), and Cember (1985). The GasEx-98 data are from Wanninkhof and McGillis (1999), the GasEx-01 data are from Hare et al. (2004), DMS data are from Huebert et al. (2004). To illustrate the effect of surface heat flux and insolation on the air-sea gas exchange at low wind speed the model curves for all gases are calculated for $Q_0 = 130$ W m^{-2}, $Q_E = 60$ W m^{-2} and for two values of $I_R(0) = 0$ W m^{-2} and $I_R(0) = 1000$ W m^{-2}

proportional to Kolmogorov's internal scale of turbulence, $\eta_\nu = \left(\nu / \varepsilon^3\right)^{1/4}$), these models are consistent with the concept of intermittency of molecular sublayers in time and space through small-scale bursting motions (Kim et al. 1971).

Initial development of the boundary-layer model for molecular sublayers is usually attributed to Saunders (1967b) who, based on the wall layer analogy, derived a formula for the temperature difference across the cool skin in the form (2.52). Boundary-layer modeling has also been applied to the free convection problem for a cooling sea surface. A theoretical formula for convective heat transfer over a horizontal plate,

$$Nu = a_0 Ra^{1/3} \tag{2.65}$$

in application to the thermal molecular sublayer below the air–water interface leads to the Katsaros et al. (1977) formula for the temperature difference across the aqueous thermal sublayer (cool skin) (2.47). The Nusselt and Raleigh numbers are defined as follows:

$$Nu = \frac{q_0}{\kappa_T(\overline{\Delta T}/h)}, \; Ra = \frac{\alpha_T g \overline{\Delta T} h^3}{\kappa_T \nu}. \tag{2.66}$$

When the exponent on the Rayleigh number is 1/3, the equality (2.65) becomes independent of depth resulting in the Katsaros et al. (1977) equation (2.47).

Since both shear and convection contribute to the energy dissipation, the boundary-layer model describes the transition from free to forced convection in pretty much the same way as the renewal model. In particular, the same dimensionless number Rf_0 controls this transition. Correspondingly, Fairall et al. (1996) modified the Saunders (1967b) parameterization (2.52) as follows:

$$\overline{\Delta T} = -\lambda_S \,\mathrm{Pr}\, q_0 u_*^{-1}\left[1+\left(a_0^{\,3}\lambda_S^4 Rf_0\,\mathrm{Pr}^2\right)^{3/4}\right]^{-1/3}$$

where $Rf_0 = \alpha_T g Q_v \nu/(c_p \rho u_*^{\,4})$ is the surface Richardson number introduced by Kudryavtsev and Soloviev (1985) from modeling surface renewals, and Q_v is the virtual cooling given by (2.58). The model remains bounded as $u_* \to 0$ (asymptotically approaching Katsaros' formula (2.45) for free convection), which is an improvement over the original Saunders (1967b) formula (2.50).

Taking into account that $\Lambda_0 = \lambda_0 \,\mathrm{Pr}^{1/2}$, boundary-layer parameterization (2.66) practically coincides with parameterization (2.56) for low and moderate wind-speed conditions. Similar to the renewal model, the boundary-layer-type model can be extended to high wind-speed conditions including wave breaking and whitecapping. Such an extension is considered by Soloviev et al. (2007) for the example of air–sea gas-transfer modeling.

Kitaigorodskii and Donelan (1984) and Dickey et al. (1984) proposed a boundary-layer-type model for parameterizing the interfacial gas-transfer velocity:

$$K_{\mathrm{int}} \approx b\left[\varepsilon(0)\,\nu Sc^{-2}\right]^{1/4} \tag{2.67}$$

where b is a dimensionless coefficient, $\varepsilon(0)$ the surface value of the dissipation rate of the turbulent kinetic energy, ν is the kinematic viscosity of water, $Sc = \nu/\mu$ is the Schmidt number, and μ is the kinematic molecular diffusion coefficient of gas in water. Relationship (2.65) can alternatively be derived (as in Fairall et al. 2000) from the hypothesis that the thickness of the diffusive molecular sublayer δ_μ is proportional to the Kolmogorov's internal scale of turbulence for concentration inhomogeneities: $\eta_D = Sc^{-1/2}(\nu^3/\varepsilon)^{1/4}$, where the thickness of the diffusive sublayer is defined as $\delta_\mu = \mu\Delta C/G_{\mathrm{int}} = \mu/K_{\mathrm{int}}$, $\Delta C = C_w - C_0$ is the effective air–sea gas concentration difference (indices "w" and "0" relate to the bulk and surface values, respectively), and G_{int} is the interfacial component of the air–sea gas flux.

Soloviev et al. (2007) have developed the boundary-layer approach in detail by including convection, shear, wave breaking, turbulence patchiness, and wave-age-dependent bubble-mediated component. Figure 2.26 compares Soloviev's et al. (2007) parameterization model with the results of direct, eddy-correlation measurements of the CO_2 air–sea flux during *GasEx-2001* (Hare et al. 2004). The resultant model curves show good agreement between model and available observations. Remarkably, within the wind-speed range of up to 9 m/s, there is practically no dependence of the gas-transfer velocity on wave age.

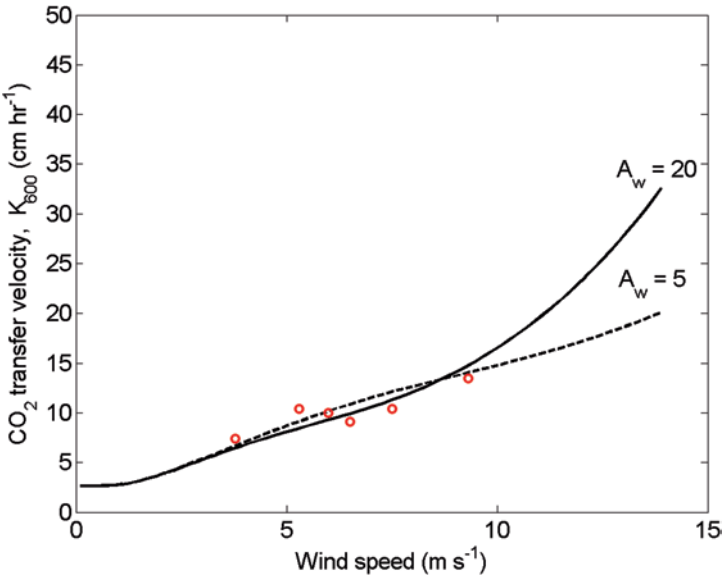

Fig. 2.26 Boundary-layer type gas-transfer parameterization for CO_2 at two wave ages A_w in comparison with the direct air-sea CO_2 flux measurements during GasEx-2001 data by Hare et al. (2004). (After Soloviev et al. 2007)

The boundary layer modeling approach is based on the physics of turbulent boundary layer near near a free interface. In contrast to the renewal model, the boundary-layer model does not explicitly include intermittency of exchange processes near the surface. Instead, it identifies the connection between the interfacial gas-transfer velocity and the dissipation of the turbulent kinetic energy directly, following Kitaigorodskii and Donelan (1984) and Dickey et al. (1984), or indirectly, via the Kolmogorov's internal scale of turbulence (Fairall et al. 2000). Since both the renewal and the boundary-layer model are based on equivalent physical principles of the boundary-layer turbulence, they ultimately lead to quite similar final results.

The effect of surface films of the air–sea exchange processes, which not only is primarily important under low wind-speed conditions but also determines dynamics of gravity-capillary waves under moderate and high wind-speed conditions, is far from complete understanding. At this point, there is no plausible parameterization or sufficient data to address this issue adequately. If future experiments will reveal significant differences in the effect of surface films on the different types of molecular sublayers, then parameterizations (2.57–2.59) will need to be decoupled in their low wind-speed portions via introduction of additional parameters (i.e., P_f) and possibly Sc and Pr number dependences similar to that proposed by Asher et al. (2005).

Consideration of the gas-transfer parameterization in terms of practical applications, including remote sensing and air–sea exchange of CO_2 and DMS gases, is explained in Chap. 7.

2.5 Effect of Penetrating Solar Radiation

2.5.1 Model Equations

The impact of penetrating solar radiation on the dynamics of molecular sublayers can be quantified in a consistent way with a renewal model (Soloviev and Schlüssel 1996). Note that the term "cool skin" might not be completely appropriate during daytime hours since in extreme situations the solar warming may reverse the sign of the temperature gradient in the thermal molecular sublayer.

Following the same approach as in Sect. 2.4.2, consider a fluid element adjacent to the sea surface that participates in the process of cyclic renewal of the surface water in the presence of both surface cooling and the volume absorption of solar radiation. Initially, the fluid element has a uniform temperature equal to the bulk-water value. As it is exposed to the interface, the molecular diffusion law governs the evolution of the temperature difference across the thermal sublayer:

$$\frac{\partial T}{\partial t} = \frac{\partial}{\partial z}\left(\kappa_T \frac{\partial T}{\partial z}\right) + \frac{\partial q_R}{\partial z}, \tag{2.68}$$

where $q_R = I_R / (c_p \rho)$ is the volume source due to absorption of solar radiation in water.

The boundary condition on the waterside of the air–sea interface is

$$-\kappa_T \frac{\partial T}{\partial z}\Big|_{z \to -0} = q_0, \tag{2.69}$$

and the initial condition is formulated as follows:

$$T(z,0) = T_w, \tag{2.70}$$

where $q_0 = Q_0 / (c_p \rho) = (Q_T + Q_E + I_L) / (c_p \rho)$, and T_w is the bulk-water temperature. Q_E and I_L do not depend strongly on the presence of the temperature difference across the cool skin (Paulson and Simpson 1981). The sensible heat flux Q_T can appreciably depend on the temperature difference across the cool skin; the magnitude of Q_T is, however, usually much less than that of Q_E or I_L. The total heat flux Q_0 is thereby assumed to be constant during the time period between successive surface renewals.

Equation (2.68) is a linear equation in partial derivatives with a volume source, and the superposition principle can be applied with initial and boundary conditions (2.69) and (2.70). This is a mixed problem with boundary conditions of the second type. Introducing a new variable $\Delta T(z,t) = T(z,t) - T_w$ the solution can be represented as follows (Vladimirov 1976):

$$\Delta T(z,t) = \Delta T_c(z,t) + \Delta T_R(z,t) \tag{2.71}$$

where

$$\Delta T_c(z,t) = -q_0(\kappa_T \pi)^{-1/2} \int_0^t (t-t')^{-1/2} \exp\left\{-\frac{z^2}{4\kappa_T(t-t')}\right\} dt' \tag{2.72}$$

and

$$\Delta T_R(z,t) = \int_0^t \int_{-\infty}^0 \hat{f}(\eta)\left[4\kappa_T \pi(t-t')\right]^{-1/2} \exp\left\{-\frac{(z-\eta)^2}{4\kappa_T(t-t')}\right\} d\eta dt' \tag{2.73}$$

with $f(z) = \partial q_R / \partial z$. The circumflex denotes an even extension of the function to $z > 0$ so that

$$\hat{f}(z) = \hat{f}(-z). \tag{2.74}$$

The quantities ΔT_c and ΔT_R are interpreted as the near-surface temperature differences due to surface cooling and due to absorption of solar radiation, respectively. Integration of (2.72) results in the following expression for the temperature difference developing due to surface cooling and molecular heat diffusion:

$$\Delta T_c(z,t) = -2q_0(t/\kappa_T)^{1/2}\left[\pi^{-1/2}\exp\left(-\xi^2\right) - \xi erfc(\xi)\right], \tag{2.75}$$

where $\xi = z(4\kappa_T t)^{-1/2}$. Expression (2.73) for the temperature difference due to absorption of solar radiation can be rewritten in the following way:

$$\begin{aligned}\Delta T_R(z,t) = &\int_0^t \int_{-\infty}^0 f(\eta)\left[4\kappa_T \pi(t-t')\right]^{-1/2} \exp\left\{-\frac{(z-\eta)^2}{4\kappa_T(t-t')}\right\} d\eta dt' \\ &+ \int_0^t \int_{-\infty}^0 \hat{f}(-\eta)\left[4\kappa_T \pi(t-t')\right]^{-1/2} \exp\left\{-\frac{(z+\eta)^2}{4\kappa_T(t-t')}\right\} d\eta dt'\end{aligned} \tag{2.76}$$

Since $\hat{f}(\eta) = \hat{f}(-\eta)$ for $\eta < 0$ and $\hat{f}(\eta) \equiv f(\eta)$ for $\eta \geq 0$, (2.76) can be transformed as follows:

$$\begin{aligned}\Delta T_R(z,t) = &\int_0^t \int_{-\infty}^0 f(\eta)\left[4\kappa_T \pi(t-t')\right]^{-1/2} \exp\left\{-\frac{(z-\eta)^2}{4\kappa_T(t-t')}\right\} d\eta dt' \\ &+ \int_0^t \int_{-\infty}^0 f(\eta)\left[4\kappa_T \pi(t-t')\right]^{-1/2} \exp\left\{-\frac{(z+\eta)^2}{4\kappa_T(t-t')}\right\} d\eta dt'\end{aligned} \tag{2.77}$$

Substitution of the expression for the absorption of solar radiation in the form given by equation (1.60):

$$f(\eta) = q_{R0} \sum_1^9 a_i \alpha_i \exp(\alpha_i \eta) \tag{2.78}$$

into (2.77) results in the following formula:

$$\Delta T_R(z,t) = q_{R0}\sum_1^9 a_i\alpha_i\left[I_1(z,t;i)+I_2(z,t;i)\right], \tag{2.79}$$

where

$$\begin{aligned} I_1(z,t;i) &= \int_0^t\int_{-\infty}^0 \exp(-\alpha_i\eta)\exp\left\{-\frac{(z-\eta)^2}{4\kappa_T(t-t')}\right\} \\ &\times\left[4\kappa_T\pi(t-t')\right]^{-1/2} d\eta dt', \end{aligned} \tag{2.80}$$

$$\begin{aligned} I_2(z,t;i) &= \int_0^t\int_{-\infty}^0 \exp(-\alpha_i\eta)\exp\left\{-\frac{(z+\eta)^2}{4\kappa_T(t-t')}\right\} \\ &\times\left[4\kappa_T\pi(t-t')\right]^{-1/2} d\eta dt', \end{aligned} \tag{2.81}$$

and q_{R0} is the scaled solar irradiance just below the sea surface mathematically defined as $q_{R0} = \left(c_p\rho\right)^{-1} I_R(z)\big|_{z\to-0} = \left(c_p\rho\right)^{-1}(1-A)I_\Sigma$.

Change of variables in (2.80) and (2.81) $\theta = t-t'$, $u = (z-\eta)(4\kappa_T\theta)^{-1/2} - \alpha_i(\kappa_T\theta)^{1/2}$, and $u' = (z+\eta)(4\kappa_T\theta)^{-1/2} + \alpha_i(\kappa_T\theta)$ leads to:

$$\begin{aligned} \Delta T_R(z,t) &= q_{R0}\sum_{i=1}^9 a_i\alpha_i\int_0^t\left\{\exp\left(\kappa_T\alpha_i^2\theta-\alpha_i z\right)\left[1+erf\left(\frac{z}{\left(4\kappa_T\theta\right)^{1/2}}\right.\right.\right. \\ &\left.\left.\left.-\alpha_i\left(\kappa_T\theta\right)^{1/2}\right)\right]+\exp\left(\kappa_T\alpha_i^2\theta+\alpha_i z\right)\left[1-erf\left(\frac{z}{\left(4\kappa_T\theta\right)^{1/2}}+\alpha_i\left(\kappa_T\theta\right)^{1/2}\right)\right]\right\}d\theta. \end{aligned} \tag{2.82}$$

Equation (2.82) is integrated to obtain

$$\begin{aligned} \Delta T_R(z,t) &= \frac{1}{2}q_{R0}\kappa_T{}^{-1}\sum_{i=1}^9 a_i\alpha_i\left\{\exp(-\alpha_i z+\delta_i^2)\left[1+erf(\xi-\delta_i)\right]\right. \\ &+\exp(\alpha_i z+\delta_i^2)\left[1-erf(\xi+\delta_i)\right]-2\exp(-\alpha_i z)+ \\ &\left.4\delta_i\left[\pi^{-1/2}\exp(-\xi^2)-\xi+\xi erf(\xi)\right]\right\} \end{aligned} \tag{2.83}$$

where $\xi = z(4\kappa_T t)^{-1/2}$ and $\delta_i = \alpha_i(\kappa_T t)^{1/2}$ are nondimensional depth and time, respectively.

According to (2.75) and (2.83), the near-surface temperature difference between the renewal events evolves in the following way:

$$\Delta T(0,t) = \Delta T_c(0,t) + \Delta T_R(0,t) = -2q_{R0}\left(\frac{t}{\kappa_T \pi}\right)^{1/2} + q_{R0}\kappa_T{}^{-1}\sum_{i=1}^{9} a_i \alpha_i^{-1}\left\{\exp(\delta_i^2)\left[1 - erf(\delta_i^2)\right] - 1\right\} + 2q_R(0)\left(\frac{t}{\kappa_T \pi}\right)^{1/2} \tag{2.84}$$

The average temperature difference across the thermal molecular sublayer of the ocean is defined as follows:

$$\Delta \overline{T} = \int_0^{\infty} p(t)\Delta T_w(0,t)dt \tag{2.85}$$

where

$$\Delta T_m(0,t) = \frac{1}{t}\int_0^t \Delta T(0,t')dt', \tag{2.86}$$

and $p(t)$ is the probability density. From (2.84) and (2.86), the following expression can be obtained:

$$\Delta T_m(0,t) = -\frac{4}{3}q_0\left(\frac{t}{\kappa_T \pi}\right)^{1/2} + \frac{q_{R0}}{\kappa_T}\sum_{i=1}^{9} a_i \alpha_i^{-1}\left(\delta_l^{-2}\left\{\exp(\delta_l^2)\left[1 - erf(\delta_l^2)\right] - 1\right\} + 2\pi^{-1/2}\delta_l - 1\right) + \frac{4}{3}q_{R0}\left(\frac{t}{\kappa_T \pi}\right)^{1/2} \tag{2.87}$$

With the Rao et al. (1971) probability density function (2.29), expression (2.85) can be rewritten in the following way:

$$\Delta \overline{T} = \pi^{-1/2}\sigma^{-1}\int_{-\infty}^{+\infty} \exp\left[-\frac{\left(t_{\ln} - m\right)^2}{\sigma^2}\right]\Delta T_m\left(0, \exp\left(t_{\ln}\right)\right)dt_{\ln}, \tag{2.88}$$

where $t_{\ln} = \ln t$, $m = \ln t_* - \sigma^2/4$, t_* is the mean time between bursting events (renewal time); m and σ^2 are the mean value and the variance of the logarithm of the random variable t, respectively. Transformation to the logarithmic variable $t_{\ln}$ is required to estimate integral (2.88) numerically.

2.5.2 Renewal Time

It follows from (2.38) that the renewal time can be expressed in the following way:

$$t_* = \frac{9\pi\nu}{16u_*^2}\exp(\sigma^2/8)\Lambda_0^2\left(1-a_0{}^3\Lambda_0^4 Rf_0\right)^{-1/2}(1+Ke/Ke_{cr}). \tag{2.89}$$

The introduction of a coefficient $A_0 = \frac{8}{3}\pi^{-1}\exp\left(\sigma^2/8\right)$, which appears in the parameterization of the air–sea gas-transfer velocity, leads to the following expression for the renewal time:

$$t_* = \frac{27A_0\nu\pi^2}{128u_*^2}\Lambda_0^2(1-a_0{}^3\Lambda_0^4 Rf_0)^{-1/2}(1+Ke/Ke_{cr}). \tag{2.90}$$

The expression for renewal time (2.90) is applicable only for nighttime conditions, when the surface flux is negative and, therefore $Rf_0 < 0$. During daytime, solar heating can affect the renewal time by inhibiting convective instability of the near-surface layer of the ocean. Moreover, in some regions of the ocean evaporation may be replaced by condensation of vapor at the ocean surface; the latent heat flux reverses its sign, and Rf_0 may become positive. In the next section, the definition of the surface Richardson number is extended for conditions of solar heating and condensation of vapor at the ocean surface.

2.5.3 Convective Instability of the Cool Skin During Daytime

Under calm weather $Rf << -a_0{}^{-3}\Lambda_0^{-4}$, and the renewal time is determined by convective instability. The positive buoyancy flux due to absorption of solar radiation may modify dynamics of the near-surface layer of the ocean. Woods (1980) proposed the following Rayleigh-number criterion characterizing the influence of solar radiation absorption on thermally driven convection in the upper ocean:

$$Ra(z) = \frac{z^4\alpha_T g q_{R0}\left[f_R(D)-f_R(z)\right]}{\nu\kappa_T{}^2}, \tag{2.91}$$

where $f_R(z)$ is the solar radiation absorption function (defined in Sect. 1.4.6), q_{R0} is the solar irradiance just below the sea surface, and D is the *compensation depth* defined from the following relationship:

$$q_0 = q_{R0}\left[1-f_R(D)\right]. \tag{2.92}$$

The maximum of $Ra(z)$ is determined by

$$dRa(z)/dz = 0 \tag{2.93}$$

With (2.91) and (2.92), condition (2.93) reduces to

$$4\left[f_R(z)-1+q_0/q_{R0}\right]+zdf_R(z)/dz=0, \tag{2.94}$$

which is used to determine the value, $z=z_{\max}$ (being somewhere between 0.7 D and 0.9 D) so that $Ra_{\max}=Ra(z_{\max})$. The absorption of solar radiation in water inhibits the thermally driven convection in the near-surface layer of the ocean when

$$Ra_{\max}=-\frac{z_{\max}^4\alpha_T g\left[-q_0+q_{R0}-q_{R0}f_R\left(z_{\max}\right)\right]}{\nu\kappa_T{}^2}<Ra_{cr}=1700 \tag{2.95}$$

Under low and calm wind-speed conditions, the absorption of solar radiation may therefore dramatically increase the renewal time especially near midday. Such an extreme effect supposedly takes place in lakes and rivers under low wind-speed conditions and a strong insolation. In the open ocean, however, additional convective instability is caused by the increase in sea surface salinity due to evaporation. The effect of absorption of solar radiation and of the additional buoyancy flux due to evaporation from the ocean surface can be included into the renewal time parameterization (2.90) by extending the definition of the surface Richardson number (2.61) in the following way:

$$Rf_0=\frac{\alpha_T g\nu}{c_p\rho u_*^4}\begin{cases}(Q_E+Q_T+I_L+(\beta_S S_0 c_p Q_E)/\alpha_T L) & \text{for } Ra_{\max}\geq Ra_{cr}\\ (\beta_S S_0 c_p Q_E)/\alpha_T L & \text{for } Ra_{\max}<Ra_{cr}\end{cases} \tag{2.96}$$

In order to extend the parameterization to cases with positive latent heat flux (condensation), Rf_0 should be reset equal to zero if it becomes positive according to expression (2.96).

2.5.4 Model Calculations

Penetrating solar radiation is specified according to (1.59)–(1.60). There are also material coefficients to be set in the model as functions of temperature and salinity; they are $\nu,\kappa_T,\alpha_T,L,c_p$, and ρ. As a first approximation, the influence of SST and salinity variability on the material coefficients is ignored, while the dimensionless product $\beta_S S_0$ is fixed at 0.026.

In Fig. 2.27, vertical profiles of ΔT_R, ΔT_c, and ΔT within the upper 43 cm of the ocean have been calculated for three wind-speed and two heat-flux regimes from equations (2.75), (2.83), and (2.71), respectively. Shown in Fig. 2.27 are the instantaneous profiles developed after a surface renewal event at the end of the renewal time period (i.e., at $t=t_*$). The renewal time is determined from formula (2.89) with the surface Richardson number defined by equation (2.96).

As expected the low wind-speed regime shows the greatest temperature deviations extending to depths of several centimeters (Fig. 2.27a, b). The model calcula-

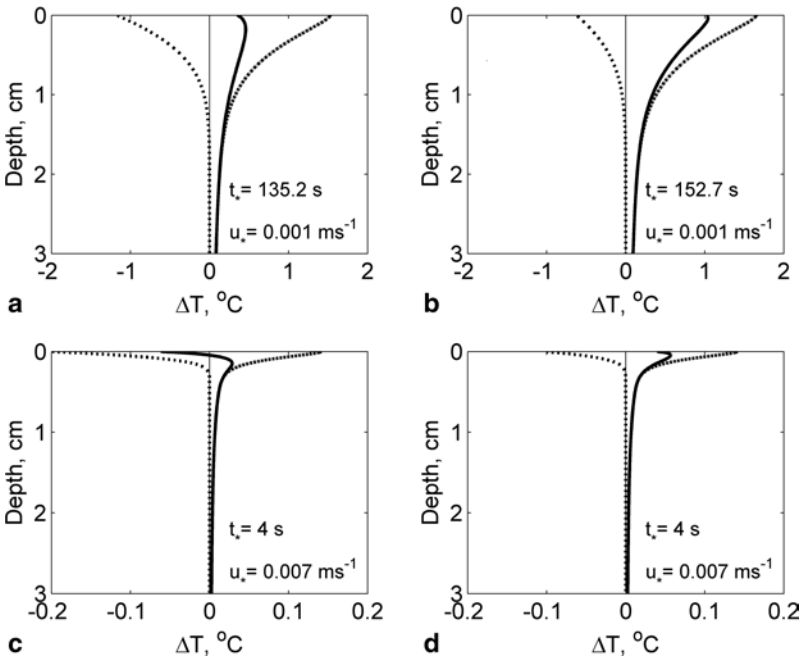

Fig. 2.27 Instantaneous vertical temperature profiles in the upper 3 cm of the ocean at the end of the time period between renewal events. The contribution of the solar heating (dash-dotted), surface cooling (dashed), and the combined effect (contiguous) are calculated from a renewal model for **a, c** $Q_0 = 140$ W m^{-2}, $Q_E = 70$ W m^{-2} and **b**, **d** $Q_0 = 70$ W m^{-2}, $Q_E = 35$ W m^{-2}. The top row (**a, b**) corresponds to free and the bottom row (**c, d**) to forced convection regimes. Solar irradiance just below the sea surface $I_R(0) = 1000$ W m^{-2}, water temperature $T_0 = 29$ °C, and salinity $S_0 = 36$ psu are the same in all cases. Note the different temperature scale between the top and bottom pairs of diagrams

tions are consistent with the instantaneous temperature profiles in the open ocean that have been observed with the free-rising profiler (see Fig. 2.3).

In contrast, the profiles generated by the model for higher friction velocities (Fig. 2.27c, d) are affected by surface cooling and heating only very close to the interface. The combined effect, $\Delta T(z)$, shows a maximum in a small range of depths between 50 and 150 μm. Above this maximum, surface cooling prevails at high wind speeds, while for the values of energy fluxes chosen here, the net effect at low wind speed is a surface warming.

Calculations with different water types from Table 2.1 do not show the temperature differences larger than 0.02 °C. The absorption and scattering of light in near-infrared band mainly determine the transmission of solar radiation within the upper few millimeters of the ocean. Dependence on the water type is small for this wavelength range.

Observation of SST by infrared radiometer averages over relatively large areas and shows an integrated contribution of the surface renewal process at different stages. Figure 2.28 shows the average temperature difference across the aqueous

Table 2.2 Comparison of different parameterizations and models for the temperature difference, ΔT, between the sea surface and 4 m depth (ship's thermosalinograph intake), with measurements made by Hartmut Grassl during TOGA COARE

Cool-skin model	Diurnal mixed layer and thermocline model	Night		Day		Day and night	
		Bias	Std. dev.	Bias	Std. dev.	Bias	Std. dev.
H	Included	0.32	0.27	0.28	0.23	0.30	0.25
S	Included	0.14	0.10	−0.02	0.19	0.05	0.15
PS	PWP	0.06	0.13	0.14	0.20	0.10	0.17
SS	PWP	0.01	0.13	0.06	0.20	0.03	0.17
SS_m	PWP	0.02	0.12	0.05	0.20	0.02	0.17
SS	SK	0.06	0.11	0.10	0.18	0.08	0.15

The cool-skin models are labeled as follows: H (Hasse 1971), S (Schluessel et al. 1990), PS (Paulson and Simpson 1981), SS (Soloviev and Schlüssel 1996), and SS_m (Soloviev and Schlüssel 1996 with updated empirical constants); the diurnal thermocline models, PWP (Price et al. 1986) and SK (Stull and Kraus 1987). All temperature differences are in °C.

thermal molecular sublayer ΔT, as well as its components ΔT_c and ΔT_R, as a function of u_*. The main effect of solar radiation on the cool skin is observed at low wind speeds. Figure 2.29 shows the diurnal evolution of the temperature difference across the aqueous thermal molecular sublayer and the direct (interfacial) air–sea gas-transfer velocity under idealized insolation conditions. For low wind speeds, suppression of free convection due to the absorption of solar radiation has a strong effect on the gas transfer at the ocean–air interface. This is because the surface renewal time "jumps" at some threshold level of insolation. For the temperature difference across the aqueous thermal molecular sublayer, this effect is not as big as for the gas exchange because of the partial compensation of surface cooling by solar heating.

2.5.5 Comparison with Daytime and Nighttime Cool-Skin Field Data

SST measurements in the western equatorial Pacific made by Hartmut Grassl from the R/V *Vickers* during TOGA COARE from 30 January to 26 February 1993 near 156°E, 2°S have provided the data set that is particularly useful in validating parameterizations for the temperature difference across the cool skin. The SST data were taken with infrared radiometer. The bulk-water temperature was measured with a standard shipboard thermosalinograph pumping water from 3 m depth. At night, the temperature differences in the upper 3 m were usually very small (a few hundredths of a degree at most). During daytime the difference between SST and water temperature taken at 3 m depth could be affected by the presence of shallow diurnal thermocline as schematically shown in Fig. 2.30. In addition, precipitation effects result in a stable salinity stratification (the near-surface rain-formed halocline), which is usually accompanied by temperature gradients. The likely presence

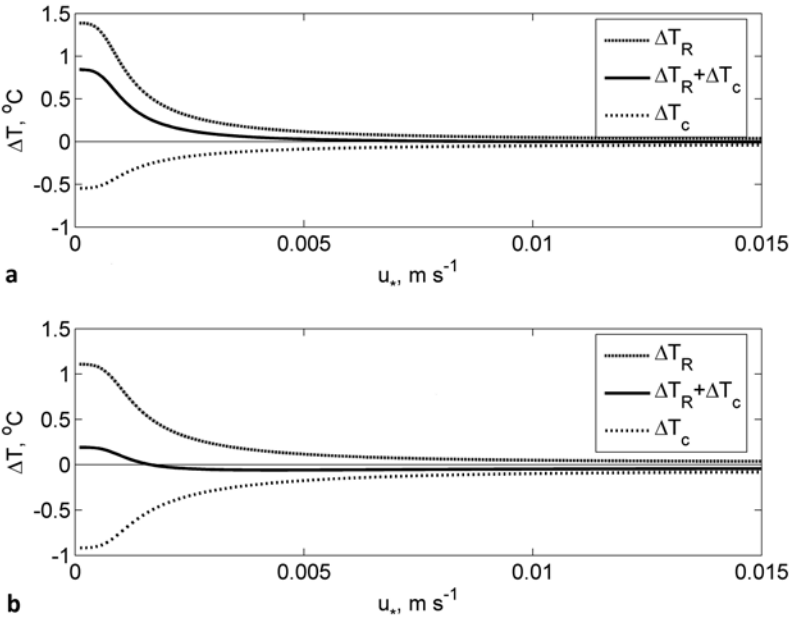

Fig. 2.28 Temperature difference across the cool skin due to solar heating ΔT_R, surface cooling ΔT_c, and the combined effect, $\Delta T_R + \Delta T_c$, as a function of friction velocity u_* calculated from parameterization (2.88) for **a** $Q_0 = 70$ W m^{-2}, $Q_E = 35$ W m^{-2}, and **b** $Q_0 = 140$ W m^{-2}, $Q_E = 70$ W m^{-2}. The solar irradiance just below the ocean surface is $I_{R0} = -1000$ W m^{-2}, water temperature $T_0 = 29$ °C, and salinity $S_0 = 36$ psu are the same for both cases

of fine thermohaline structure in the upper few meters of the ocean under low wind-speed conditions is one of the limitations of the cool-skin model validation. (More details about the fine thermohaline structure of the near-surface layer of the ocean can be found in Chap. 4)

As a first approximation, the temperature difference across the diurnal thermocline (ΔT_d) can be accounted for with a model of the diurnal mixed layer and thermocline. We make use of two types of models for the diurnal mixed layer and thermocline. The first model is that of Price et al. (1986), hereafter referred to as PWP. The second model is that of Stull and Kraus (1987), hereafter referred to as SK. The SK model is the so-called transilient (nonlocal) model, which represents the turbulent transport by a cascade of eddies. The absorption of solar radiation is simulated with nine spectral components for water type IB according to Jerlov (1976) classification (see Chap. 1, Table 1.2), because this type of water is typical for in the TOGA COARE domain.

Figure 2.31 compares parameterization (2.88), hereafter referred to as SS_m, with the TOGA COARE data. Since the field measurements include both the thermal molecular sublayer and diurnal thermocline, a diurnal mixed layer model has been included, either PWP or SK (only the PWP model results are shown in Fig. 2.31c). Both mixed layer model calculations include the surface heat and radiation fluxes,

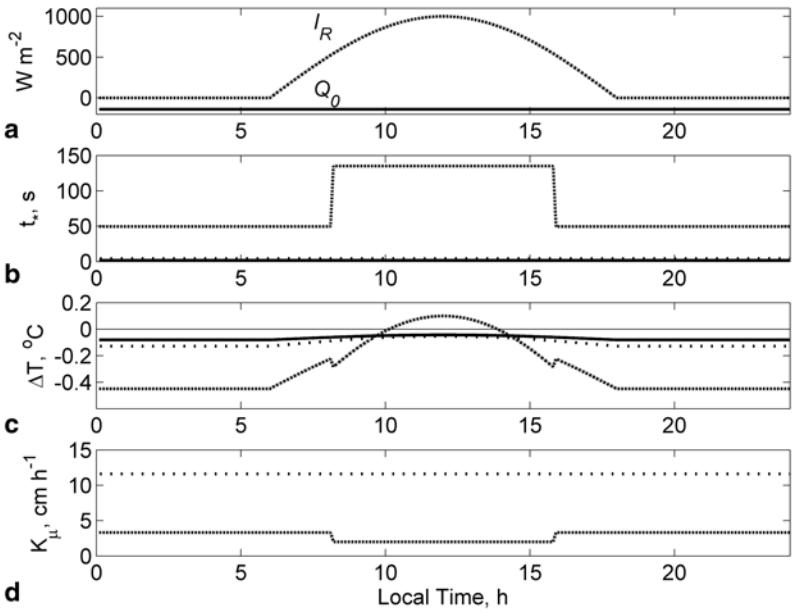

Fig. 2.29 Evolution of temperature difference across the cool skin and of the direct air-sea gas transfer coefficient during 24 h at three different friction velocities: **a** idealized diurnal cycle of the surface solar irradiance and the net surface heat flux, **b** renewal time, **c** temperature difference across the cool skin, **d** direct air-sea gas transfer coefficient for a Schmidt number Sc = 430 (CO_2 at 29 °C and 35 psu). In (b), (c), and (d) the dash-dotted, dotted and contiguous lines correspond to the condition of free convection ($u_* = 0.001$ m s^{-1}), forced convection ($u_* = 0.007$ m s^{-1}), and intensive surface waves breaking ($u_* = 0.015$ m s^{-1}), respectively

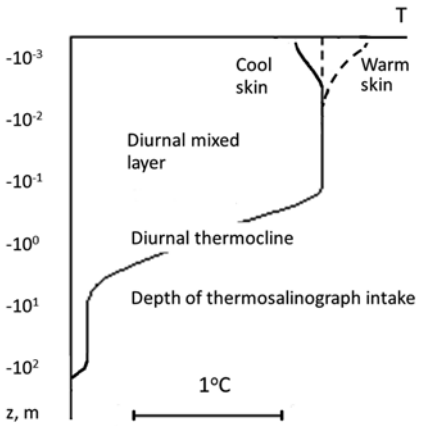

Fig. 2.30 Schematic representation of the vertical temperature profile during a large diurnal warming event. Typical depth and temperature scales are shown (but may vary greatly)

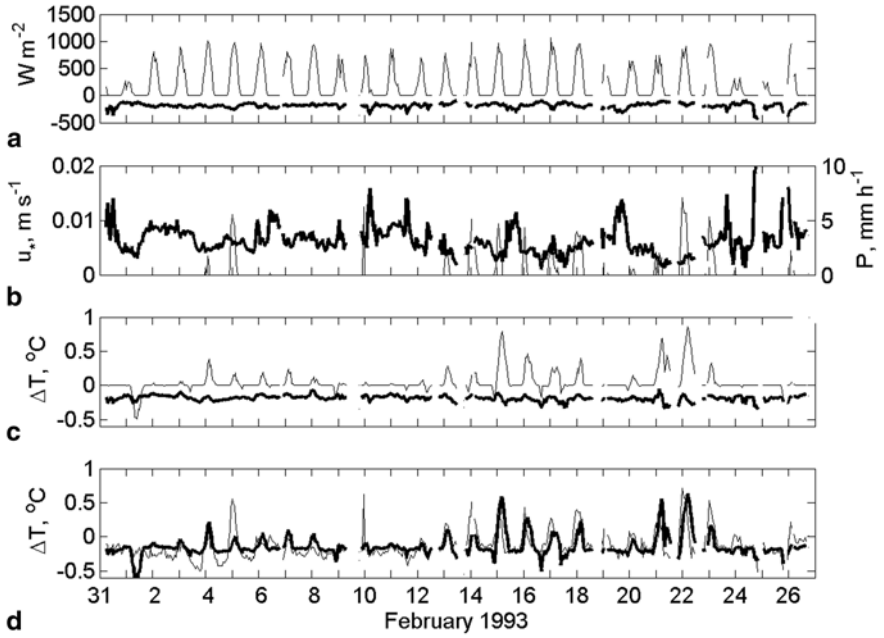

Fig. 2.31 Comparison of parameterization SS_m with measurements during TOGA COARE. **a** hourly means of the surface solar irradiance I_R0 (thin line) and net surface heat flux Q_0 (bold line), **b** hourly means of friction velocity u_* (bold line) and rain rate P (thin line), **c** calculated temperature difference across the cool skin (parameterization SS_m, bold line) and across the diurnal thermocline with the PWP model, thin line), **d** hourly means of the difference between bulk and skin temperature as observed during COARE (thin line), parameterized by SS_m plus PWP model (bold line). (After Soloviev and Schlüssel 1996)

wind stress, and rainfall rates as measured from the R/V *Vickers*. (Technical details relating to mixed layer modeling in this case can be found in Soloviev and Schlüssel 1996.) Figure 2.31d suggests that there is a phase shift between the PWP model prediction and field data under conditions of evening deepening. This is related to the slow, diffusive response of the PWP model during deepening of the diurnal thermocline. The SK model reproduces the SST evolution with no phase delay; it, however, results in a larger bias than the PWP model.

Table 2.2 compares several parameterizations and models of the cool skin with the TOGA COARE data set. The Paulson and Simpson (1981) parameterization (labeled PS), the Soloviev and Schlüssel (1996) parameterization (labeled SS), as well as the Hasse (1971) model (labeled H) are designed to calculate $\Delta\overline{T}$ during day and night. The parameterization specified by Schlüssel et al. (1990) is labeled S; it has the night- and daytime components. Models H and S implicitly include the effect of the diurnal thermocline (ΔT_d); PS, SS, and SS_m are designed to parameterize the temperature difference $\Delta\overline{T}$ across the thermal molecular sublayer (cool skin) only.

The SS cool-skin parameterization combined with the PWP model produces a bias of –0.03 °C and a standard deviation of 0.17 °C. The SS parameterization

combined with a nonlocal model of the diurnal thermocline SK gives a slightly better standard deviation (0.15 °C) but larger bias (–0.08 °C). The SS_m cool-skin parameterization, which represents the SS parameterization with updated constants ($a_0 = 0.23$, $\Lambda_0 \approx 10$, and $Ke_{cr} \approx 0.18$), produces a bias of –0.02 °C and a standard deviation of 0.17 °C.

Model S (including both cool-skin and diurnal thermocline parameterizations) and the PS+PWP model produced comparable results. Traditional parameterization H exhibits a larger bias and standard deviation. The H parameterization is, however, based entirely on data from a field experiment in the Northeast Atlantic Ocean and is not necessarily valid in other parts of the world ocean.

Though parameterization SS_m, combined with the PWP model follows the main features of the field data (Fig. 2.31) and on average outperforms the other models brought to the analysis, in some situations, especially under low wind-speed conditions, the "instantaneous" difference between the model and data exceeds 0.5 °C. As mentioned above, numerical models of the diurnal mixed layer and thermocline are not yet perfect, in particular under low wind-speed conditions. Improvement of the mixing parameterization is one of the closely related issues (see Sect. 1.7.5).

Note that the SS cool-skin model uses the Soloviev and Schlüssel (1996) version of the renewal model. New field data instigated a modification of the empirical coefficients entering this model, as described in Sect. 2.4.2. Qualitative comparison of the revised model with the COARE data set presented in has not been done.

Both mixed layer models, SK and PWP, account for the rain-formed stratification in the near-surface layer. None of the cool-skin models mentioned in this section, however, accounts for the rain-related effects that are the subject of the next sections.

2.6 Cool and Freshwater Skin of the Ocean during Rainfall

Rain falling into the sea modifies the aqueous molecular sublayers through a variety of different effects. These effects include additional momentum flux and stabilizing buoyancy flux from air to sea, additional sensible heat flux of the rain, modification of physical water constants because of temperature and salinity changes, increase in the surface roughness, damping of short gravity waves, excitation of capillary waves at higher wave frequencies, and the surface mixing by droplets.

During rainfall the raindrops penetrate to tens of centimeters directly affecting the near-surface salinity. Rain falling on the sea surface also establishes a haline diffusive molecular sublayer with a salinity gradient. Schlüssel et al. (1997) refer to this layer as the *freshwater skin* of the ocean. The freshwater skin is only about 50 μm thick. The salinity difference developing in the haline diffusive molecular sublayer can to some extent affect the interpretation of the radar and radiometric observations of the sea surface at low microwave frequencies. The dielectric constant of water depends on the sea surface salinity at centimeter wavelengths (Lager-

loef et al. 1995). The dielectric constant change may cause interpretation problems when remotely measuring wind speed or SSTs at these frequencies. The dielectric constant dependence on salinity may also be used for remote sensing of the sea surface salinity. Though the depth of the haline molecular sublayer is much less than the penetration depth of the electromagnetic radiation at these wavelengths, the exponential decay of the radiation energy entering the ocean can, however, make it sensitive to salinity changes in the skin layer.

An important effect is the dependence of gas solubility on salinity. For instance, a 1 % decrease in the seawater salinity results in a 0.5 % increase in the CO_2 solubility and 0.1 % increase in the O_2 solubility (Stephen and Stephen 1964; Riley and Skirrow 1965).

In view of the different effects that can be expected from rainfall on the surface molecular sublayer, Schlüssel et al. (1997) provide a comprehensive description of the modifications of this layer of the ocean due to precipitation. According to these authors, the impact of precipitation on the thermal and diffusive molecular sublayers of the ocean includes the following processes:

1. The freshwater flux due to rain produces a buoyancy flux in the near-surface layer of the ocean, which tends to suppress convection (Ostapoff et al. 1973).
2. Raindrop temperatures are usually lower than the SST (Katsaros 1976). The precipitation falling into the ocean results in an interfacial sensible heat flux Q_{rs} caused by small drops that do not penetrate into the ocean and in a volume heat flux Q_{rV} due to drops submerging into the ocean and gradually mixing with depth.
3. Changes in the temperature and salinity due to rain mentioned in the previous two points modify physical constants of sea surface water (Katsaros and Buettner 1969). In particular, the kinematic viscosity increases with decreasing temperature and decreases with decreasing salinity.
4. Rainfall can enhance the surface roughness as much as two orders of magnitude by generation of impact craters, Rayleigh jets, splash drops, and small waves (Houk and Green 1976).
5. Raindrops falling into the ocean fragment and partly remove surface films (Green and Houk 1979).
6. Raindrops penetrating through the surface disturb wave motions and damp the short gravity waves by reducing the amplitudes at which they break (Yakimov 1959; Manton 1973; Tsimplis and Thorpe 1989; Le Méhauté and Khangaonkar 1990; Poon et al. 1992). As a result, small-scale wave breaking intensifies and the surface renewal time period decreases.
7. Raindrops impact the sea surface and submerge into the ocean, generating additional surface renewals.
8. Raindrops obtain horizontal momentum from the airflow at cloud levels. These raindrops subsequently pass this momentum to the atmospheric boundary layer and to the sea surface, adding to the wind stress that acts on the surface (Caldwell and Elliot 1971). All the momentum of the drop is transferred to the ocean, as opposed to only a small fraction the air.

9. The freshwater skin coexisting with the cool skin is subject to irreversible thermodynamic processes due to significant local temperature and salinity gradients (Doney 1995).

Schlüssel et al. (1997) made an attempt to quantify the various effects of rain on the aqueous molecular sublayers. The irreversible thermodynamic processes in the presence of the cool skin and freshwater skin, however, have not yet been quantified.

2.6.1 Effects of Rain on the Cool Skin

Following again the same approach as in Sect. 2.4.2, consider a fluid element adjacent to the sea surface that participates in the process of cyclic renewal of the surface water in the presence of rain. Initially, the fluid element has a uniform temperature equal to the bulk-water value T_w. As it is exposed to the interface, the molecular diffusion law governs the evolution of the temperature difference across the thermal sublayer.

In the framework of the surface renewal theory described in Sect. 2.4.2 the temperature change between subsequent renewal events in the thermal molecular sublayer of the ocean including a volume source is described by the molecular diffusion equation similar to (2.68) but, instead of solar radiation term, including the volume source of heat due to rain:

$$\frac{\partial T}{\partial t} = \frac{\partial}{\partial z}\left(\kappa_T \frac{\partial T}{\partial z}\right) - P(T_0 - T_r)\frac{\partial f_V}{\partial z}, \tag{2.97}$$

where f_V is the volume source function defined according to (1.78) and T_r the raindrop temperature. We ignore here the difference between specific heats and densities of seawater and rainwater.

The surface boundary condition is defined by rain-induced surface heat flux (1.80):

$$-\kappa_T \frac{\partial T}{\partial z} = \frac{Q_{rs}}{c_p \rho} = P\left(T_0 - T_r\right)\left[1 - f_V\left(0\right)\right]. \tag{2.98}$$

Instead of the volume heat source due to the absorption of solar radiation, equation (2.97) includes the volume source of heat due to raindrops mixing with their environment. In order to reduce the problem of the rain effect to the already considered problem of the solar radiation effect on the cool skin, Schlüssel et al. (1997) approximated the volume source function in (2.97) by a sum of exponentials (similar to the solar radiation absorption function):

$$\partial f_V(z)/\partial z \simeq \sum_{i=1}^{N_r} \varsigma_l \exp(\psi_l \Lambda z / a_r), \tag{2.99}$$

where ς_l and ψ_l are coefficients obtained by a nonlinear least-squares fit. The requirements, $\varsigma_l > 0$ and $\psi_l > 0$, resulted in $N_r = 14$ terms for a good fit. The numerical values of these coefficients for $r_c = 0.40$ mm and $r_c = 0.75$ mm can be found in the original publication of Schlüssel et al. (1997).

The solution to a linear problem (2.97)–(2.98) with a homogeneous vertical temperature profile as the initial condition is obtained in the same way as for equation (2.97) (for details, see Sect. 2.5.1). The temperature difference between the SST $\Delta T_r(0,t)$ and the bulk-water temperature is then as follows:

$$\Delta T_r(0,t) = \Delta T_{rs}(0,t) + \Delta T_{rv}(0,t) \tag{2.100}$$

where

$$\Delta T_{rs}(0,t) = P(T_r - T_w)2\sqrt{\frac{t}{\kappa_T \pi}}\left(1 + 2\Lambda r_c + \frac{4\Lambda^2 r_c^2}{2} + \frac{8\Lambda^3 r_c^3}{6}\right)\exp(-2\Lambda r_c),$$

$$\Delta T_{rV}(0,t) = P\left(T_r - T_w\right)\frac{1}{\kappa_T}\sum_{l=1}^{L}\frac{\varsigma_l a_r}{\Lambda \psi_l}\left[\exp\left(\delta_l^2\right)\left[erf\left(\delta_l\right) - 1\right] + 1 - \pi^{-1/2}\delta_l\right],$$

$\xi = z/\sqrt{4\kappa_T t}$, and $\delta_l = \psi_l \Lambda\sqrt{kt}/a_r$. The first term on the right side of (2.100) is related to the surface flux of rainwater, while the second term is related to the volume source of rainwater.

In accordance with the renewal concept, this temperature difference should be averaged over time by weighting with probability density $p(t)$ of the surface renewals:

$$\overline{\Delta T} = \int_0^\infty p(t)\Delta T_{wr}(0,t)\,dt \tag{2.101}$$

where

$$\Delta T_{wr}(0,t) = \frac{1}{t}\int_0^t \Delta T_r(0,t')dt' \tag{2.102}$$

With (2.100), the solution to (2.102) is

$$\begin{aligned}
&\Delta T_{wr}(0,t) = P(T_r - T_w)\times \\
&\left\{\frac{4}{3}\sqrt{\frac{t}{\kappa_T \pi}}\left(1 + 2\Lambda r_c + \frac{4\Lambda^2 r_c^2}{2} + \frac{8\Lambda^3 r_c^3}{6}\right)\exp(-2\Lambda r_0) - \right. \\
&\frac{1}{\kappa_T}\sum_{l=1}^{L}\frac{\varsigma_l a_r}{\Lambda \psi_l}(\delta_l^{-2}\left\{\exp(\delta_l^2)\left[1 - erf(\delta_l^2)\right] - 1\right\} + 2\pi^{-1/2}\delta_l - 1) - \\
&\left.\sum_{l=1}^{L}\frac{4}{3}\varsigma_l\sqrt{\frac{t}{\pi\kappa_T}}\right\},
\end{aligned} \tag{2.103}$$

which is used together with (2.101) and the lognormal probability density function of the surface renewals similar to (2.87)–(2.88); this allows the numerical integration that gives the modification of the cool skin caused by the sensible heat flux related to the rain.

2.6.2 Freshwater Skin of the Ocean

Besides the modification of the cool skin, rainfall creates a freshwater skin on the top of the ocean where a salinity flux takes place via molecular diffusion (Schlüssel et al. 1997). Under no-rain conditions, evaporation at the sea surface increases salinity, which tends to destabilize the near-surface water enhancing the renewal process at the surface. However, when rain starts, the part of the rain that does not submerge into the ocean can compensate for the evaporation effect and create a stably stratified freshwater skin. This is analogous to the conversion of the cool skin into its antipode, the warm skin, which sometimes occurs under conditions of strong insolation. Consequently, this freshwater effect on diffusion can be described by the diffusion equation in analogy to equation (2.97) that was derived for the thermal sublayer:

$$\frac{\partial S}{\partial t} = \frac{\partial}{\partial z}\left(\mu \frac{\partial S}{\partial z}\right) - PS\frac{\partial f_V}{\partial z}, \tag{2.104}$$

where μ is the coefficient of molecular salinity diffusion and f_V is the volume source function due to rain submerging into the ocean.

The surface boundary condition for salinity flux due to rain that is to be included in the boundary condition for the diffusion equation (2.104) is as follows:

$$-\mu \frac{\partial S}{\partial z} = J_{rs} = S_0 P\left[1 - f_V(0)\right]. \tag{2.105}$$

Assuming that

$$\Delta S << S_w, \tag{2.106}$$

the salinity S and its surface value $S_{0,}$ entering equations (2.104) and (2.105), respectively, are both replaced with the bulk-water salinity S_b. The solution to the linear problem (2.104)–(2.106) is then obtained in the same way as in Sect. 2.5.1 (as well as in the previous section, Sect. 2.6.1):

$$\Delta S_r(0,t) = \Delta S_{rs}(0,t) + \Delta S_{rv}(0,t), \tag{2.107}$$

where

$$\Delta S_{rs}(0,t) = -PS_0 2\sqrt{\frac{t}{\kappa_T \pi}}\left(1 + 2\Lambda r_c + \frac{4\Lambda^2 r_c^2}{2} + \frac{8\Lambda^3 r_c^3}{6}\right)\exp(-2\Lambda r_c)$$

and

$$\Delta S_{rV}(0,t) = -PS_0 \frac{1}{\kappa_T}\sum_{l=1}^{L}\frac{\varsigma_l a_r}{\Lambda \psi_l}\left[\exp(\delta_l^2)\left[erf(\delta_l) - 1\right] + 1 - \pi^{-1/2}\delta_l\right].$$

The first term on the right side of (2.107) is related to the surface flux of rainwater, while the second term is related to the volume source of rainwater.

The first term on the right side of (2.100) is related to the surface flux of rainwater, while the second term is related to the volume source of rainwater.

The salinity difference should be averaged over time by weighting with probability density $p(t)$ of the surface renewals:

$$\overline{\Delta S} = \int_0^\infty p(t)\Delta S_{mr}(0,t)\,dt \tag{2.108}$$

where

$$\begin{aligned}
&\Delta S_{mr}(0,t) = -PS_0 \times \\
&\left\{\frac{4}{3}\sqrt{\frac{t}{\kappa_T \pi}}\left(1 + 2\Lambda r_c + \frac{4\Lambda^2 r_c^2}{2} + \frac{8\Lambda^3 r_c^3}{6}\right)\exp(-2\Lambda r_0)\right. \\
&- \frac{1}{\kappa_T}\sum_{l=1}^{L}\frac{\varsigma_l a_r}{\Lambda \psi_l}(\delta_l^{-2}\left\{\exp(\delta_l^2)\left[1 - erf(\delta_l^2)\right] - 1\right\} + 2\pi^{-1/2}\delta_l - 1) \\
&\left. - \sum_{l=1}^{L}\frac{4}{3}\varsigma_l\sqrt{\frac{t}{\pi\kappa_T}}\right\}.
\end{aligned} \tag{2.109}$$

Solutions (2.109) hold for the linear case only under an assumption that $S \approx S_w$ (i.e., $\Delta S << S_w$) and physical properties of seawater do not change substantially because of the salinity dependence. The properties that could be affected by the rain-caused changes in sea surface salinity are the thermal expansion coefficient, kinematic viscosity, density, specific heat, and latent heat of vaporization. The large salinity differences arising from substantial freshwater influx and relatively long renewal times would require a nonlinear solution to (2.104)–(2.105). However, as shown in the next section, under moderate and heavy rain conditions the renewal time is restricted to very small values, while in light rain the drop of surface salinity remains relatively small so that the solution for the nonlinear case may not be required in most cases.

2.6.3 Surface Renewals Due to Rain Mixing

Small raindrops do not produce an impact crater on the sea surface, while large drops do, disturbing the aqueous molecular sublayer. The area covered by each impact crater is subject to a surface renewal event since the impact crater is deeper than the conductive layer and represents a "catastrophic" event for the molecular sublayer (Engel 1966). (Note that spray droplets from breaking waves also have to be considered in this regard.)

Rodriguez and Mesler (1988) studied drops falling from low heights into pools of liquid; they found that the impact crater radius r_k exceeds about two to three times the corresponding drop radius r_0. Drops falling from higher altitudes generate even bigger craters, with radii up to $r_k \approx 4r_0$ (Prosperetti and Oguz 1993). Dimensional analysis conducted by these authors suggests that the radius of the impact crater can be represented by a formula

$$r_k = r_0 \left(\frac{8}{3} Fr \right)^{1/4} \approx \varphi_c r_0 Fr^{1/4}, \tag{2.110}$$

where $Fr = w_t^2 / gr_0$ is the Froude number, g is the acceleration of gravity, w_t is the terminal velocity of raindrops, and $\varphi_c = (8/3)^{1/4} \approx 1.278$ is a dimensionless constant. Relationship (2.110) has been supported by observations of Pumphrey and Elmore (1990). Comparison with data from Engel (1966) suggests a somewhat smaller constant of about $\varphi_c = 1.05$. This discrepancy is nevertheless relatively small compared to other uncertainties relating to rain-induced mixing (e.g., the size distribution of droplets).

The terminal velocity of raindrops falling on the ocean surface can be estimated from an empirical formula given by Best (1950):

$$w_t = w_\upsilon \left[1 - \exp\left(-\left(r_0 / r_\upsilon \right)^\upsilon \right) \right], \tag{2.111}$$

where $w_\upsilon = 9.43$ m s^{-1}, $r_\upsilon = 1.77 \times 10^{-3}$ m, and $\upsilon = 1.147$. For radii 0.3×10^{-3} m $< r_0 < 6 \times 10^{-3}$ m, representing the majority of the raindrops, (2.111) is approximated within 0.1 m s^{-1} accuracy by

$$w_t = w_\upsilon \left[b_1 - b_2 \exp\left(-r_0 / r_\upsilon \right) \right] \tag{2.112}$$

where $b_1 = 1.0528$ and $b_2 = 1.07733$. Substituting w_t from (2.112) into (2.110) transforms formula (2.110) into a functional dependence of the impact crater radius solely on the raindrop radius:

$$r_k = \varphi_c r_0 \left(\frac{w_u^2 \left[b_1 - b_2 \exp\left(-r_0 / r_\upsilon \right) \right]^2}{gr_0} \right)^{1/4}. \tag{2.113}$$

The area that is subject to renewal due to the raindrop impact is equal to the impact crater area. The number of drops of size $r_0 \pm dr_0$ that reach the surface per unit time and unit area is $n(r_0)w_t(r_0)dr_0$, where $n(r_0)$ is the drop size distribution in the atmosphere near the water surface. Respectively, Craeye and Schlüssel (1998) represented the crater flux density (i.e., the production rate of crater area per unit area and unit time) as follows:

$$F_k = \int_{r_c}^{\infty} \pi r_k(r_0)^2 n(r_0) w_t(r_0) dr_0. \tag{2.114}$$

Representing the distribution of the rain above the sea surface by the Marshall–Palmer drop size spectrum (1.64) and substituting relationships (2.112) into equation (2.114), and (2.113) into (2.114) results in the following formula:

$$\begin{aligned} F_k = & \int_{r_c}^{\infty} \pi r_0^2 \varphi_c^{\,2} \left(\frac{w_v^2 \left[b_1 - b_2 \exp\left(-r_0 / r_v\right) \right]^2}{g r_0} \right)^{1/2} \\ & \times n\left(r_0\right) w_v \left[b_1 - b_2 \exp\left(-r_0 / r_v\right) \right] dr_0. \end{aligned} \tag{2.115}$$

The renewal time is then defined as the inverse of the impact-flux density F_k,

$$t_{*r} = 1 / F_k \tag{2.116}$$

The calculation of the integral on the right side of (2.115) and substituting the result into (2.116) leads to

$$\begin{aligned} t_{*r} = & \frac{g^{1/2}}{\pi n_0 \varphi_c^{\,2} w_v^2} \left[b_1^2 \left(2\Lambda\right)^{-5/2} \Gamma\left(5/2, 2\Lambda r_c\right) \right. \\ & - 2 b_1 b_2 \left(2\Lambda + r_v^{-1}\right)^{-5/2} \Gamma\left(5/2, 2\Lambda r_c + r_c r_v^{-1}\right) \\ & \left. + b_2^2 \left(2\Lambda + 2 r_v^{-1}\right)^{-5/3} \Gamma\left(5/2, 2\Lambda r_c + r_c r_v^{-1}\right) \right], \end{aligned} \tag{2.117}$$

where Γ is the incomplete gamma function.

Figure 2.32 shows the surface renewal time t_{*r} as a function of rain rate P. The rainfall strongly influences the renewal time even for low rain rates. For $P > 2$ mm h^{-1}, the rain-induced surface disruptions dominate the renewal process including the surface renewals caused by breaking wavelets or long breaking waves. In calm situations, even light rainfall easily surpasses the effect of free convection on the renewal time.

Figure 2.33a shows the skin cooling due to rainfall for renewal times determined by the rain as a function of rain rate. The variation of the volume flux of heat with rain rate is compensated by the rain-induced mixing, leaving an almost constant,

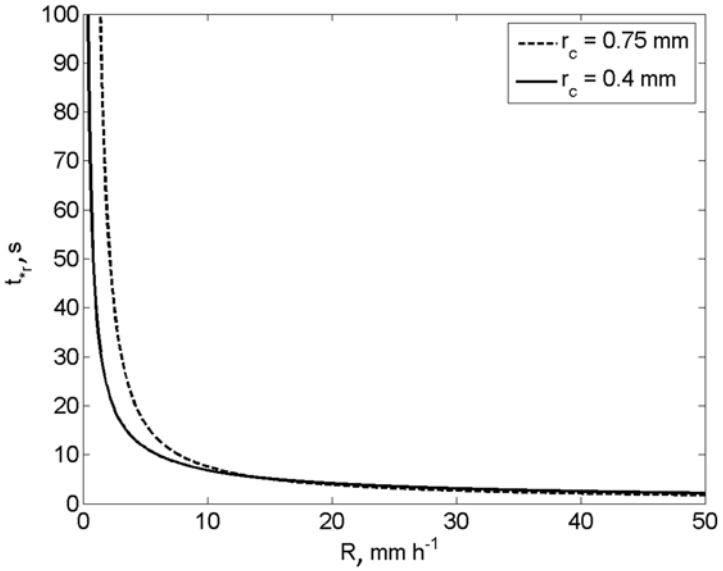

Fig. 2.32 Surface renewal time due to rain calculated from (2.117) as a function of rain rate for two critical radii r_c . (After Schlüssel et al. 1997)

but small temperature difference that depends on the difference between surface and rain temperatures only (the latter is here held constant at 5 °C). The effect of surface heat flux, however, does increase with rain rate. Nevertheless, at rain rates below 50 mm h^{-1} the temperature difference across the cool skin does not exceed $\Delta T = -0.08$ °C for the given surface versus rain temperature difference.

Figure 2.33b shows the freshwater skin due to rainfall for renewal times determined by the rain. The maximum salinity difference across the diffusion sublayer does not exceed $\Delta S = 5$ psu for rain rates up to 50 mm h^{-1}. It is, nevertheless, a dramatic salinity change compared to the range of typical salinity variations in the ocean. The drop in the surface salinity due to rain is mainly due to the surface component of the freshwater flux; the contribution of submerging raindrops appears to be small.

The combined renewal time can be derived by considering renewal events caused by skin friction and kinetic energy fluxes and rain-induced renewals as independent processes. Hence, within a given time period, the number of total renewals equals the sum of renewals due to rain t_{*r} and renewals due to momentum and energy fluxes t_{*f}. The combined renewal time is then given by formula suggested in Schlüessel et al. (1997):

$$1/t_* = 1/t_{*f} + 1/t_{*r} \tag{2.118}$$

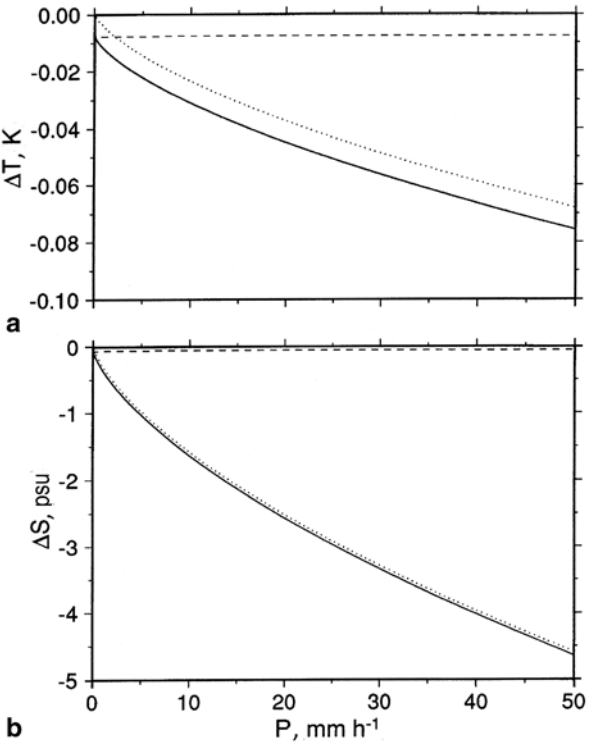

Fig. 2.33 Skin cooling by rainfall with a typical rain drop temperature of 5 °C below the sea surface temperature **(a)** and freshwater skin due to rainfall at bulk salinity of $S_w = 35$ psu **(b)**, both as a function of rain rate with respect to renewal times determined by the rainfall; the total effects are shown by the solid line, the effects due to drops penetrating into the ocean by the dashed lines and that due to surface heat flux by the dotted lines. (After Schlüessel et al. (1997). Reproduced with permission from Springer Science and Business Media)

2.6.4 Buoyancy Effects in Molecular Sublayer Due to Rain

At the sea surface from the waterside ($z \to -0$) the vertical flux of buoyancy is as follows:

$$B_0 = -\frac{g}{\rho}\overline{(w'\rho')}\Big|_{z\to -0} = -\frac{\alpha_T g}{c_p \rho}\left(Q_E + Q_T + Q_L + Q_{rs}\right) - \beta_S S_0 g \frac{Q_E}{\rho L} - \beta_S g Q_{rs}. \quad (2.119)$$

The buoyancy flux due to rain stabilizes the upper ocean, which affects the dynamics of molecular sublayers. The description of this effect is included through a modification of the surface Richardson number Rf_0

$$Rf_0 = -\nu B_0 / u_*^4, \quad (2.120)$$

where B_0 is defined in (2.119).

Expression (2.120) accounts for surface fluxes only; volume absorption of solar radiation or raindrops submerging into the ocean complicates the analysis. In the general case, the approach described in Sect. 2.5.3 can be applied: B_0 is set to zero when the maximum Rayleigh number is less than the critical value for negative val-

ues of Rf_0; positive values of Rf_0 are always set to zero. Estimates, however, show that even for very low rain rates the buoyancy flux due to freshwater input is stronger than the counterparts due to the thermal convection and evaporative surface salinity increase. Under low wind-speed and rainy conditions Rf_0 easily becomes zero, leading to very high values of t_{*f}. Below a certain rain rate (~ 0.1 mm h^{-1}) the buoyancy effect inhibits the additional mixing due to rain, while, the additional mixing due to rain prevails at larger rain rates.

The analysis of Fig. 2.33 also suggests that the contribution of the volume freshwater flux into the diffusion molecular sublayer (freshwater skin) is relatively small compared to that of the surface freshwater flux. The contribution of the volume source into the freshwater skin is negligible in most cases.

2.6.5 Rain Effects on Sea Surface Roughness

Disruptions of the sea surface produced by rain increase the sea surface roughness. The Rayleigh-jet columns, together with the raindrops on their tops and the wavelets radiated from the drop impact zones, are roughness elements that can increase the surface roughness beyond the wind-induced roughness. The roughness elements produced by the rain do not propagate as the wind-induced waves do and therefore resemble fixed obstacles such as roughness elements on land surfaces.

The molecular sublayers of the surface ocean are mainly controlled by the tangential shear stress. The flow above the surface is aerodynamically smooth as long as the height of the roughness elements is smaller than $5\nu/u_*$, where ν is the kinematic viscosity and u_* is the friction velocity of the air (Schlichting 1979). In the aerodynamically smooth flow, the momentum is passed to the ocean by skin friction only. If the roughness elements are greater than $70\nu/u_*$, the flow is aerodynamically rough, and the momentum transfer is affected by the form drag. Figure 2.34a shows the smooth and rough regimes as a function of friction velocity. There is a transition zone between these regimes, where both skin and form drag are important. The Rayleigh-jet that extends a centimeter or more into the air (Siscoe and Levin 1971) therefore affects form drag, except for situations with very low friction velocities when the thickness of the viscous sublayer increases without bound.

Engel (1966) proposed a formula for the maximum height of the waves directly adjacent to the impact craters generated by drop impacts:

$$h_{w,\max} = \alpha_0 \left(\left[\alpha_1 \frac{r_0^3 \rho_r w_t^2}{g\rho} + \alpha_2 \frac{\sigma_s^{\,2}}{g^2 \rho^2} \right]^{1/2} - \alpha_3 \frac{\sigma_s}{g\rho} \right)^{1/2} \tag{2.121}$$

where σ_s is the surface tension of the sea surface, $\alpha_0 = 33.33$, $\alpha_1 = 1.2 \times 10^8$, $\alpha_2 = 3.1149 \times 10^{10}$, and $\alpha_3 = 1.7649 \times 10^5$. Figure 2.34a shows dependence of $h_{w,\max}$ on the drop radius (2.121) with the terminal velocity parameterized according to (2.111); the flow is smooth no matter what the drop size is for very small fric-

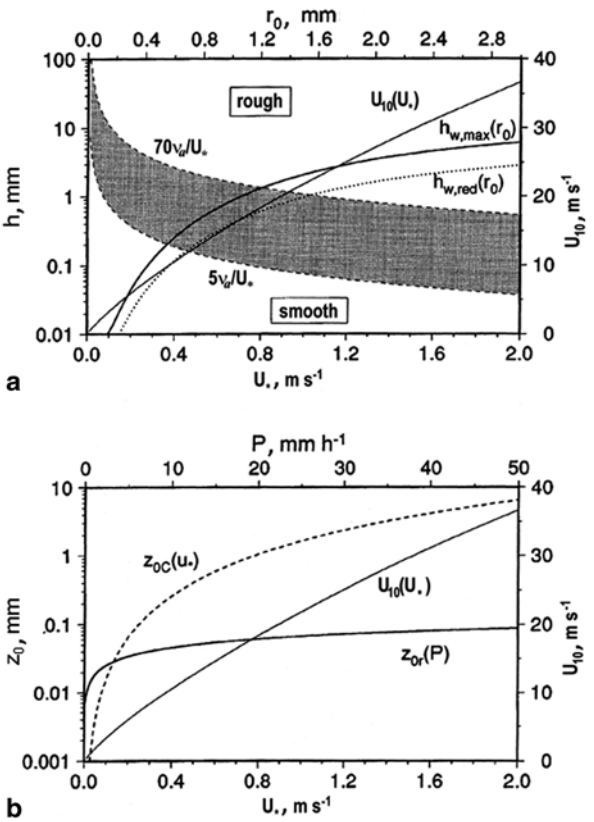

Fig. 2.34 **a** Separation of aerodynamically smooth and rough domains (dashed curves) with the transition region indicated by the hashed area, maximum ($h_{w,max}(r_0)$, solid) and reduced ($h_{w,red}(r_0)$, dotted) heights of the rain-induced wavelets depending on drop radius r_0 and the relation between wind speed u_{10} and friction velocity of the air u_* (thin solid); **b** roughness length z_0 of wind-roughed surface (dashed) and rain-induced wavelets (solid) as a function of friction velocity of air u_* and rain rate R, respectively, as well as the relation between wind speed and friction velocity (thin solid). Note: axes on opposite sides are not independent. (After Schlüessel et al. (1997). Reproduced with permission from Springer Science and Business Media)

tion velocities owing to the unbounded increase in the viscous sublayer thickness. With increasing friction velocities, drops with radii greater than about 1 mm lead to waves that cause a rather rough flow, while waves produced by smaller drops do not disturb the flow smoothness.

Smooth surface waves contribute to the surface roughness in a different way compared to random roughness elements. According to Motzfeld's (1937) experiment in a wind tunnel, the drag coefficient at a height of 0.2 m over surface waves is about seven times smaller than that over a surface with rough elements of the same size. Schlüessel et al. (1997) estimated that under the assumption of a logarithmic wind profile this implies a reduction of the roughness length of the rain-induced wavelets by a factor of 0.4 when compared to the roughness length of random rough elements of the same height. This effect leads to some increase in the wave height above which the flow becomes rough shown by the curve labeled $h_{w,red}(r_0)$ in Fig. 2.34a. Taking into account the Marshall–Palmer drop-size distribution (1.64) an upper limit of the mean height of the wavelets is estimated from the formula

$$\bar{h}_{w,red}(P) = \int_{r_c}^{\infty} h_{w,red} n_0 \exp(2\Lambda r_0)\, dr_0 \Big/ \left(\int_{r_c}^{\infty} n_0 \exp(2\Lambda r_0)\, dr_0 \right) \qquad (2.122)$$

Formula (2.122) implies that the rain-induced waves do not decay and uniformly cover the sea surface. Equation (2.122) has been resolved substituting (2.112) into (2.121) and subsequently approximating

$$h_{w,red} = \beta_0 + \beta_1 r_0^{3/4}(1 - \beta_2 \exp(-r_0 / r_\upsilon)), \tag{2.123}$$

where $\beta_0 = 0.0129$ mm, $\beta_1 = 1.60686\ \text{mm}^{1/4}$, and $\beta_2 = 1.0978$. The resulting relationship is

$$\begin{aligned}\overline{h}_{w,red}(R) = \beta_0 + \Big\{&\beta_1 (2\upsilon)^{-7/4}\Gamma(7/4, 2\Lambda r_c) \\ &+ \beta_2 (r_\upsilon^{-1} + 2\Lambda)^{-7/4}\Gamma(7/4, (r_\upsilon^{-1} + 2\Lambda) r_c)\Big\} 2\Lambda \exp(2\Lambda r_c).\end{aligned} \tag{2.124}$$

Figure 2.34b shows the roughness length calculated for the rain-induced wavelets using a coarse estimate given by Lettau (1969) as $z_{0r} \approx 0.058\overline{h}_{w,red}^{1.19}$. For comparison purposes, the roughness length z_{0C} of the wind-induced surface roughness under neutral conditions according to Charnock's (1955) formula is also given on this composite plot. The above estimate for the rain-induced roughness length is the maximum possible value, requiring an optimal drop impact and a surface uniformly covered with rain-induced wavelets. Wave interactions, which have been neglected here, likely result in greater wave heights.

The rain-induced roughness increases strongly with rain rates up to about 2 mm h^{-1}, while at higher rain rates z_{0r} increases only slightly (Fig. 2.34b). Only for air friction velocity less than approximately 0.15 m s^{-1} can the rain-induced waves appreciably contribute to the surface roughness. Charnock's (1955) formula employed for the calculation of z_{0C} in Fig. 2.34b, however, does not work under low wind-speed conditions. In fact, due to viscous effects, the surface roughness under low wind stresses increases with decreasing wind.

Figure 2.34b exhibits considerable differences in the rain-induced roughness lengths compared to those from laboratory studies by Houk and Green (1976). This is because of a more realistic raindrop spectrum employed by Schlüessel et al. (1997), which also covers many small, submillimeter drops, while in the laboratory the effect of large drops (several millimeters in diameter) had been mainly investigated. The large drops in fact cover a very small portion of the natural spectrum of raindrops (Pruppacher and Klett 1978).

The rain-induced stress leads, together with the wind stress, to increased surface wind-drift currents. This effect coexists with the attenuation of short gravity waves by enhanced turbulence in the upper ocean during rainfall (Tsimplis and Thorpe 1989). The rain-induced wind-drift currents also reduce the amplitude threshold at which short gravity waves break (Philips and Banner 1974).

From investigations in a wind–wave tank, Poon et al. (1992) found that gravity waves in the frequency range between 2 and 5 Hz decay during rainfall. At the same time, the spectral density of wave slopes in the frequency domain between 10 and 100 Hz drastically increases. The latter effect is due to rain-induced waves; however, it is pronounced only under low wind-speed conditions. The results of experi-

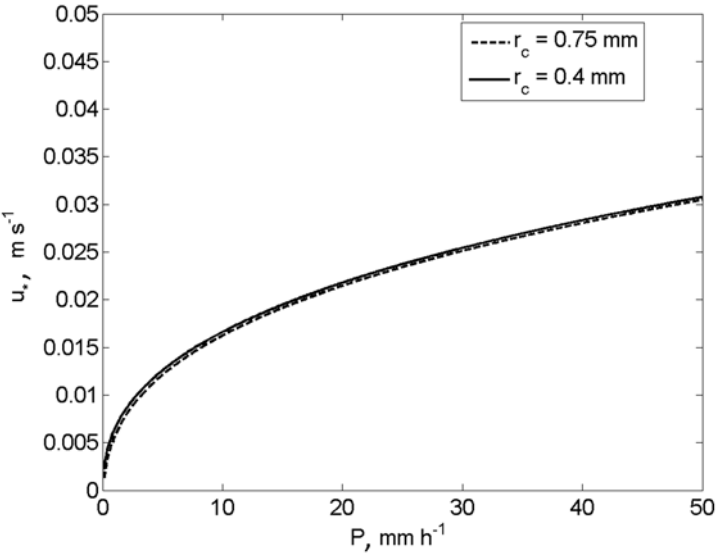

Fig. 2.35 Friction velocity in the upper ocean attributed to the flux of kinetic energy carried by rain as function of rain rate for two values of critical radii r_c calculated from (2.130). (After Schlüssel et al. 1997)

ments in a wind–wave tank by Yang et al. (1997) are consistent with the Poon et al. (1992) findings but provided some more details to the rain effects on fine structure of wind waves.

Due to damping of short gravity waves, a substantial part of the momentum transferred to the ocean by form drag under non-precipitating situations is instead transferred by skin friction during rainfall. This results in decrease of the surface renewal time, which is concurrent with the damping of short gravity waves.

2.6.6 Flux of Kinetic Energy Carried by Rain

According to Tsimplis (1992), the flux of kinetic energy carried by rain with a uniform drop size distribution is

$$F_k = \frac{1}{2}\rho P w_t^2. \tag{2.125}$$

In order to include the effect of natural drop size distributions, Craeye and Schlüssel (1998) introduced the spectral rain rate falling on the sea surface

$$\frac{dP}{dr_0} = \frac{4}{3}\pi r_0^3 n(r_0) w_t \tag{2.126}$$

which leads to a kinetic energy flux of

$$F_k = \frac{2}{3}\pi\rho\int_{r_c}^{\infty} r_0^3 n(r_0) w_t^3 dr_0. \tag{2.127}$$

For rain with a drop size distribution (1.64) and terminal velocities described by (2.112) the kinetic energy flux is then determined by

$$\begin{aligned} F_k = {} & \frac{2}{3}\pi\rho n_0 \int_{r_c}^{\infty} r_0^3 \left[b_1^3 \exp(-2\Lambda r_0) - 3b_1^2 b_2 \exp\left(-\left(2\Lambda + r_\upsilon^{-1}\right) r_0\right) \right. \\ & \left. + 3b_1 b_2^2 \exp\left(-\left(2\Lambda + 2v r_\upsilon^{-1}\right) r_0\right) - b_2^3 \exp\left(-\left(2\Lambda + 3r_\upsilon^{-1}\right) r_0\right)\right], \end{aligned} \tag{2.128}$$

where only drops entering the ocean ($r_0 > r_c$) are considered. The solution is

$$\begin{aligned} F_k = {} & \frac{2}{3}\pi\rho n_0 w_\upsilon{}^3 \left[\frac{b_1^3}{(2\Lambda)^4}\Gamma(4, 2\Lambda r_c) - \frac{3b_1^2 b_2}{\left(2\Lambda + r_\upsilon^{-1}\right)^4}\Gamma\left(4, 2\Lambda + \frac{r_c}{r_\upsilon}\right) \right. \\ & \left. + \frac{3b_1 b_2^2}{\left(2\Lambda + 2r_\upsilon^{-1}\right)^4}\Gamma\left(4, 2\Lambda r_c + \frac{2r}{r_\upsilon}\right) - \frac{b_2^3}{\left(2\Lambda + 3r_\upsilon^{-1}\right)^4}\Gamma\left(4, 2\Lambda r_c + \frac{3r_c}{r_\upsilon}\right)\right] \end{aligned} \tag{2.129}$$

The equivalent friction velocity scale in the upper ocean is

$$u_{*r} = \left(F_k / \rho\right)^{1/3} \tag{2.130}$$

Figure 2.35 shows the friction velocities corresponding to the flux of kinetic energy carried by the rain as a function of rain rate for two critical radii r_c. The friction velocity in water u_* reaches 3 cm s^{-1} at $P = 50$ mm h^{-1}.

2.6.7 Combined Effect

The enhancement of the near-surface mixing by rain is estimated by accounting for the area impacted by the raindrops of given rain rate and size distribution. It turns out that the interval between rain-induced surface renewal events can be far shorter than for wind-generated renewal events, which strongly reduces the temperature difference across the cool skin. However, for small rain rates this can be counteracted by the density stratification caused by the freshwater input. Subsequently, the extra momentum carried by the rain to the surface is accounted for, and the creation of additional surface roughness by rain-induced waves is estimated. The enhanced surface stress causes increased wind-drift currents, which, according to laboratory observations, can reduce the amplitude threshold for short gravity waves to break. This effect is parameterized as a function of rain rate. The rain-induced changes of

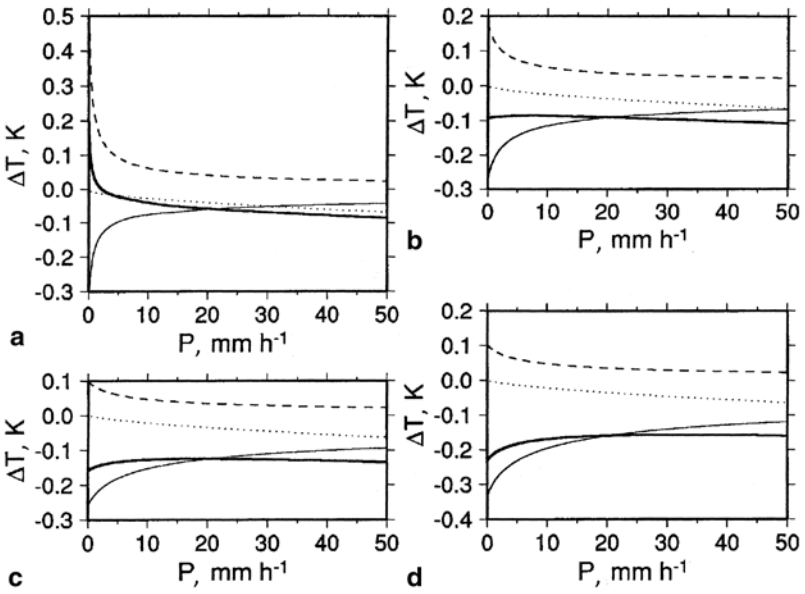

Fig. 2.36 Temperature differences across the thermal molecular sublayer as a function of rain rate for **a** $U_{10} = 1$ m s^{-1}, **b** $U_{10} = 5$ m s^{-1}, **c** $U_{10} = 10$ m s^{-1}, and **d** $U_{10} = 15$ m s^{-1}. The curves correspond to differences due to cooling by turbulent and long wave fluxes (thin solid line), warming due to the absorption of solar radiation (dashed line), rain-induced cooling (dotted line) and the combined effect (thick solid line). (After Schlüessel et al. 1997. Reproduced with permission from Springer Science and Business Media)

physical properties of seawater become important at low wind speeds, while the effect of surface film fragmentation and removal by rain is believed to be negligible in affecting the molecular sublayer (Schlüessel et al. 1997).

Schlüessel et al. (1997) incorporated all of the effects described above in a surface renewal model in order to study the combined effect of the processes involved in the physics of the aqueous molecular sublayers at the ocean surface. Figure 2.36 shows temperature differences for wind speeds of $U_{10} = 1, 5, 10, 15$ m s^{-1} for an air–sea temperature difference of 1 °C, a dew point difference of 6 K, a net longwave radiative flux of 70 W m^{-2}, and a solar irradiance of 1,000 W m^{-2}. (Note that fixing the radiative fluxes as done here is unrealistic, but is done to illustrate the physics. As wind and rain rate increase, clouds will change, certainly affecting both shortwave and longwave components.) The turbulent heat fluxes are calculated from the TOGA COARE bulk flux algorithm version 2.5b (Fairall et al. 1996). For the situations simulated, the corresponding latent and sensible heat fluxes are $Q_E = 33, 107, 186, 252$ W m^{-2} and $Q_T = 2, 7, 11, 14$ W m^{-2}. The rain temperature is assumed equal to the wet-bulb temperature calculated from the psychometric equation; its value is $T_r = 20.6$ °C when compared to the surface temperature of $T_0 = 25$ °C.

Figure 2.36 suggests that the most pronounced effect is due to additional mixing caused by the rain. This is observed at low rain rates where the rather high tempera-

ture differences prevailing in the non-precipitating situations quickly drop to low values when the rain rate increases to a few mm h^{-1}. However, with further rain rate increase the temperature difference weakens. It is remarkable that the temperature differences do not vanish even for precipitation rates of 50 mm h^{-1}. The additional skin cooling by the rain increases with rain rate though it does not exceed –0.1 K. At low wind speeds and very low rain rates the combined effect of solar warming and cooling by the turbulent and longwave fluxes results in a warm skin. At higher wind speeds, the combined effect shows a minimum skin cooling at a distinct rain rate, which depends on the actual friction velocity. Further increasing rain rates lead to a slightly enhanced cooling due to the rain-induced heat flux (Fig. 2.36b–d).

2.6.8 Comparison with Data

The surface renewal model including the precipitation component described above has been tested by Schlüessel et al. (1997) with the COARE data taken from the R/V *Vickers* in January–February 1993 near 156 °E, 2 °S and from the R/V *Wecoma* near 156 °E, between 2 °S and 5 °N (Fig. 2.37). The frequent convective rain in the western equatorial Pacific shows strong variability with rain rates ranging from less than 0.1 to more than 100 mm h^{-1}; this tests the parameterization under a great variety of situations.

The R/V *Vickers* surface fluxes in the Schlüessel et al. (1997) comparison were identical to those shown in Fig. 2.31. The calculated temperature differences across the cool skin that were caused by surface and volume cooling due to the rain showed values generally below 0.05 °C; only one case with heavy precipitation exceeding 100 mm h^{-1} gave a cooling by more than 0.1 °C. There were just a few cases with strong daytime precipitation; during these rare periods the solar warming of the skin was about halved, according to the model. During nighttime the net effect of rain on the cool skin was rather small. Apart from several cases with strong rain when the cool skin was reduced by rain-induced mixing to values below 0.1 °C, the effects of mixing and additional cooling partly canceled each other during this observation in the western equatorial Pacific Ocean.

Similar to the analysis shown in Fig. 2.31a, quantitative comparison of the parameterization with measurements of the skin versus bulk temperature difference from the R/V *Vickers* required that the temperature difference between the bulk sampling depth (i.e., the depth of the thermosalinograph intake) and the surface microlayer was accounted for. This temperature difference was calculated with the mixed-layer model of Price et al. (1986) (PWP).

The overall agreement of the cool-skin parameterization including rain is slightly better when compared to the results presented in Fig. 2.31. While the RMS error remains unchanged (0.17 °C), the small bias of 0.03–0.02 °C found earlier (Table 2.2) has now vanished completely. This is also true for the night and daytime data considered separately. In view of the skin measurement errors and the relatively small amount of data (total sample size of hourly means is 578) the result of this com-

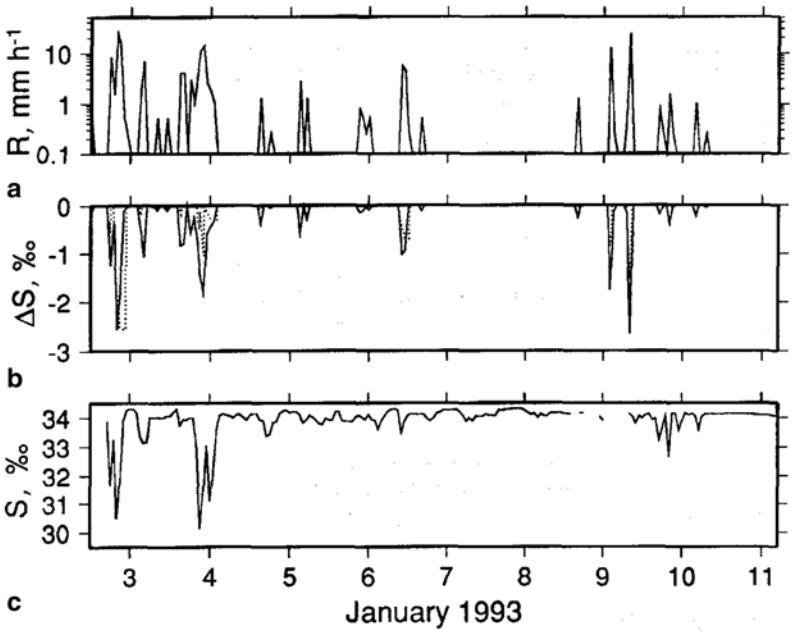

Fig. 2.37 Parameterization of the freshwater skin during raining episodes of COARE; **a** hourly mean rain rates, **b** calculated hourly mean salinity difference across the haline molecular layer (solid) and across the upper part of the mixed layer (dotted), **c** hourly mean salinity of water collected from the upper 2–3 cm of the ocean; the labels of the time axis identify the end of the days in UT. (After Schlüessel et al. 1997. Reproduced with permission from Springer Science and Business Media)

parison is rather an indication that the inclusion of the rain parameterization in the surface renewal model is useful.

Paulson and Lagerloef (1993) performed a pilot study of the near-surface salinity under rainy conditions in the tropical Pacific Ocean near 156 °E and between 2 °S and 5 °N. From the R/V *Wecoma* during COARE leg 2, they collected surface water from the upper 2–3 cm of the ocean with a scoop and hose. The temperature and salinity of the water were measured with a thermosalinograph. The salinity measurements were accompanied by detailed measurements of surface meteorological parameters including rain rates and downwelling shortwave and longwave radiation. Schlüessel et al. (1997) averaged these data sets over hourly intervals and used them with the surface renewal model to estimate the parameters of the freshwater skin of the ocean.

Figure 2.37 shows time series of the rain rate, the salinity difference across the freshwater skin, and the salinity measured at the surface for a rainy time period in January 1993. The direct comparison of the model and field data is not feasible because the model calculation is for the freshwater skin (the upper few tens of micrometers of the ocean only), while the measured salinities include surface water from the upper few centimeters.

Schlüssel et al. (1997) assumed that the freshwater skin layer must account for the greater part of the observed salinity changes because even heavy rainfall (≈ 60 mm h^{-1}) alters the salinity in the upper mixed layer by less than 1 psu (Kantha and Clayson 1994). Because the wind speeds during this experiment were rather low, the salinity changes in the mixed layer can be expected to be slightly higher. Calculations with the model of Price et al. (1986) show maximum differences exceeding 2 psu over the top half meter on 3 January that are of the same magnitude as the difference across the freshwater skin. The observed salinity changes on this day are up to 4 psu (some of this signal may, however, be associated with nonlocal rain).

For other rainfall events during this time series, the observed salinity differences in the mixed layer are generally smaller than those across the skin. A full explanation of the salinity deficits measured can only be given by considering the combined differences across the skin and mixed layers, which has not yet been done.

2.6.9 Discussion

Of the various processes that can modify the molecular layers during rainfall, the most important appears to be the rain-induced mixing that leads to enhanced surface renewals and the additional surface and volume cooling by raindrops with temperatures below the SST. Simulations with the renewal model have shown that the additional surface cooling by rain could exceed 1 °C, if the rain did not affect the surface renewal time. Nevertheless, the additional mixing and the implied increase in renewal frequencies limit the effect to less than 0.1 °C when the rainwater is 5 K cooler than the sea surface. The more impressive effect is the creation of a haline molecular diffusion layer during rainfall—a freshwater skin of the ocean—that exhibits salinity differences greater than 4 psu during strong rains.

Since laboratory studies overemphasized large drops that are a small fraction of the natural raindrop spectrum, the calculations of the rain-induced surface roughness for a realistic drop size spectrum show that this effect has been overestimated in the past (Houk and Green 1976). The wind-induced surface roughness is more important than that caused by rain except during low wind-speed conditions.

The application of the cool-skin parameterization, including the rain component, to the field measurements taken during COARE, shows some additional surface cooling that is still generally less than 0.1 °C. The cooling and mixing effects of the rainfall on the molecular sublayer partly compensate each other so that the net effect on the temperature difference almost vanishes. Nevertheless, the measured bulk versus skin temperature difference across the cool skin shows a reduction of systematic deviations of parameterized from measured differences when the rain effects are included. The errors in the measured parameters and parameterization of the turbulent surface fluxes that enter the surface renewal and mixed layer models, however, prevent a statistically significant improvement between the measured and parameterized cool skin. The salinity changes during rainfall observed in the upper

2–3 cm of the ocean can only be explained when the salinity difference across the haline molecular diffusion layer is included.

Studies of rain impacts on the sea surface have been limited to a single rain drop-size distribution, namely the Marshall–Palmer distribution. While this limitation is due to the fact that it is a distribution based on the rain rate as the only available rain parameter (which is really not a justification), the effects induced by a more precise drop-size distribution should be assessed. Further work is necessary to analyze the effect of high-latitude types of precipitation on the molecular boundary layers. For example, snowfall certainly leads to enhanced surface cooling without much volume flux, while hail falling on the sea surface penetrates deeper into the ocean than rain but subsequently returns to the surface. Precipitation in the form of hail results in more complicated surface and volume fluxes, because of a prolonged decay time compared to rain or snow.

References

Antonia RA, Chambers AJ, Friehe CA, Van Atta CW (1979) Temperature ramps in the atmospheric surface layer. J Atmos Sci 36:99–108

Asher WE, Atmane MA, Jessup AT (2005) An application of a surface penetration model to air-water gas transfer. 37th International Liège Colloquium on Ocean Dynamics (2–6 May 2005) gas transfer at water surfaces (abstract only)

Azizjan GV, Volkov YA, Soloviev AV (1984) Experimental investigation of vertical thermal structure of thin boundary layers of the sea and atmosphere. Atmos Ocean Phys 20(6):511–519

Baier RE, Goupil DW, Perlmutter S, King R (1974) Dominant chemical composition of sea surface films, natural slicks and foams. J de Rech Atmos 8:571–600

Banner ML, Peregrine DH (1993) Wave breaking in deep water. Annu Rev Fluid Mech 25:373–397

Banner ML, Peirson WL (1998) Tangential stress beneath wind-driven air-water interface. J Fluid Mech 364: 107–137

Banner ML, Phillips OM (1974) On the incipient breaking of small scale waves. J Fluid Mech 65:647–656

Benjamin TB (1960) Effects of a flexible boundary on hydrodynamic stability. J Fluid Mech 9:513

Benjamin TB (1963) The threefold classification of unstable disturbances in flexible surfaces bounding in viscid flows. J Fluid Mech 16:436–450

Best A (1950) The size distribution of raindrops. Q J Roy Meteor Soc 76:16–36

Bock EJ, Frew NM (1993) Static and dynamic response of natural multicomponent oceanic surface films to compression and dilation: laboratory and field observations. J Geophys Res 98:14599–14617

Bolin B (1960) On the exchange of carbon dioxide between atmosphere and sea. Tellus 12(3):274–281

Broecker WS, Peng TH, Stuiver M (1978) An estimate of the upwelling rate in the equatorial Atlantic based on the distribution of bond radiocarbon. J Geophys Res 83(C12):6179–6186

Caldwell DR, Elliott WH (1971) Surface stresses produced by rainfall. J Phys Oceanogr 1:145–148

Caulliez G, Makin V, Kudryavtsev V (2008) Drag of the water surface at very short fetches: observations and modeling. J Phys Oceanogr 38:2038–2055

Cember R (1989) Bomb radiocarbon in the Red Sea: A medium scale gas exchange experiment. J. Geophys Res 94: 2111-2123

Charnock H (1955) Wind stress on a water surface. Q J Roy Meteor Soc 81:639–640

Cox C (2001) Sea surface micro-structure: relation to air-sea fluxes, bubble transport and electromagnetic wave radiation. SIO Report A969093, La Jolla, CA
Craeye C, Schlüssel P (1998) Rainfall on the sea: surface renewal and wave damping. Bound-Lay Meteorol 89:349–355
Csanady GT (1978) Turbulent interface layers. J Geophys Res 83:2329–2342
Csanady GT (1990) The role of breaking wavelets in air-sea gas transfer. J Geophys Res 95:749–759
Cunliffe M, Murrell JC (2009) The sea surface microlayer is a gelatinous biofilm. ISME J 3: 1001–1003
Cunliffe M, Upstill-Goddard RC, Murrell JC (2011) Microbiology of aquatic surfacemicrolayers. FEMS Microbiol Rev 35:233–246
Dhanak MR, Si C (1999) On reduction of turbulent wall friction through spanwise wall oscillations. J Fluid Mech 383:175–195
Dickey TD, Hartman B, Hammond D, Hurst E. (1984) A laboratory technique for investigating the relationship between gas transfer and fluid turbulence. In: Gas Transfer at Water Surfaces, W. Brutsaert and G.H. Girka, Eds.: 93-100
Doney SC (1995) Irreversible thermodynamics and air-sea exchange. J Geophys Res 100:8541–8553
Ebuchi N, Kawamura H, Toba Y (1987) Fine structure of laboratory wind-wave surfaces using an optical method. Bound-Lay Meterol 39:133–151
Engel OG (1966) Carter depth in fluid mechanics. J Appl Phys 37:1798–1808
Fairall CW, Bradley EF, Rogers DP, Edson JB, Young GS (1996) Bulk parameterization of air-sea fluxes in TOGA COARE. J Geophys Res 101: 3747–3767
Fairall CW, Hare JE, Edson JB, McGillis W (2000) Parameterization and micrometeorological measurements of air-sea gas transfer. Bound Layer Meteorol 96: 63-105.
Fedorov KN, Ginzburg AI (1988) The near-surface layer of the ocean, Hydrometeoizdat, Leningrad. Translated into English in 1992 by VSP, P.O. Box 346, 3700 AH Zeist, The Netherlands
Fedorov KN, Vlasov VL, Ambrosimov AK, Ginzburg AI (1979) Investigating the surface layer of evaporating sea water by optical interferometry. Izvestya, Academy of Sciences, USSR, Atmospheric and Oceanic Physics 15:742–747
Fiedler L, Bakan S (1997) Interferometric measurements of sea surface temperature and emissivity. German J Hydrogr 49(2/3):357–365
Flack KA, Saylor JR, Smith GB (2001) Near-surface turbulence for evaporative convection at an air-water interface. Phys Fluids 13:3338
Foster TD (1971) Intermittent convection. Geophys Fluid Dyn 2:201–217
Franklin MP, McDonald IR, Bourne DG, Owens NJ, Upstill-Goddard RC, Murrell JC (2005) Bacterial diversity in the bacterioneuston (sea surface microlayer): the bacterioneuston through the looking glass. Environ Microbiol 7:723–736
Frew NM (1997) The role of organic films in air–sea exchange. In: Liss PS, Duce RA (eds) The sea surface and global change. Cambridge Univ. Press, New York, pp 121–172
Garrett WD (1965) Collection of slick-forming materials from the sea surface. Limnol Oceanogr 10:602–605
Caulliez G, Makin V, Kudryavtsev V (2008) Drag of the Water Surface at Very Short Fetches: Observations and Modeling. J Phys Oceanogr 38: 2038–2055
Ginzburg AI, Zatsepin AG, Fedorov KN (1977) Fine structure of the thermal boundary layer in the water near the air-water interface. Izvestya, Academy of Sciences, USSR, Atmospheric and Oceanic Physics 13:869–875
Gladyshev MI (1997) Biophysics of the sea surface film of aquatic ecosystems. In: Liss PS, Duce RA (eds) The sea surface and global change. Cambridge University Press, UK, pp 321–338
Glazman RE, Greysukh A (1993) Satellite altimeter measurements of surface wind. J Geophys Res 98:2475–2483
Grassl H (1976) The dependence of measured cool skin of the ocean on wind stress and total heat flux. Bound Lay Meteorol 10:465–474

Green T, Houk DF (1979) The removal of organic surface films by rain. Limnol Oceanogr 24:966–970
Hardy JT (1982) The sea-surface microlayer: biology, chemistry and anthropogenic enrichment. Prog Oceanogr 11:307–328
Hardy JT, Hunter KA, Calmet D, Cleary JJ, Duce RA, Forbes TL, Gladyshev ML, Harding G, Shenker JM, Tratnyek P, Zaitsev Y (1997) Report group 2–biological effects of chemical and radiative change in the sea surface. In: The Sea Surface and Global
Hare JE, Fairall CW, McGillis WR, Edson JB, Ward B, Wanninkhof R (2004) Evaluation of the National Oceanic and Atmospheric Administration/Coupled-Ocean Atmospheric Response Experiment (NOAA/COARE) air-sea gas transfer parameterization using GasEx data. J Geophys Res 109:C08S11
Harvey GW, Burzell LA (1972) A simple microlayer method for small samples. Limnol Oceanogr 11:156–157
Hasse L (1971) The sea surface temperature deviation and the heat flow at the air-sea interface, Bound. Layer Meteor 1: 368-379
Horrocks LA, Candy B, Nightingale T, Saunders RW, O'Carroll AG, Harris AR (2003) Parameterisations of the skin effect and implications for satellite-based measurement of sea-surface temperature. J Geophys Res 108:3096
Houk DF, Green T (1976) A note on surface waves due to rain. J Geophys Res 81:4482–4484
Howard LN (1961) Note on a paper of John Miles. J Fluid Mech 10:509–512
Howard LN (1966) Convection at high Rayleigh number. Proc of the Eleventh Intern. Congress of Applied Mechanics, Munich, pp 1109–1115
Hühnerfuss H, Walter W, Lange PA, Alpers W (1987) Attenuation of wind waves by monomolecular sea slicks and the Marangoni effect. J Geophys Res 92(4):3961–3963
Jessup AT, Zappa CJ, Yeh HH (1997) Defining and quantifying microscale wave breaking with infrared imagery. J Geophys Res 102(C10):23,145–23,154
Kantha LH, Clayson CA (1994) An improved mixed layer model for geophysical applications. J Geophys Res 99:25,235–25,266
Kanwisher J (1963) Effect of wind on CO2 exchange across the sea surface. J Geophys Res 68(13):3921–3927
Katsaros KB (1976) Effect of precipitation on the eddy exchange in a wind-driven sea. Dynam Atmos Oceans 1:99–126
Katsaros KB (1980) The aqueous thermal boundary layer. Bound Layer Meteorol 18:107–127
Katsaros KB, Buettner KJK (1969) Influence of rainfall on temperature and salinity of the ocean surface. J Appl Meteorol 8:15–18
Katsaros KB, Liu WT, Businger JA, Tillman JE (1977) Heat transport and thermal structure in the interfacial boundary layer measured in an open tank of water in turbulent free convection. J Fluid Mech 83:311–335
Kim HT, Kline SJ, Reynolds WC (1971) The production of turbulence near a smooth wall in a turbulent boundary layer. J Fluid Mech 50:133–160
Kim J, Moin P, Moser R (1987) Turbulence statistics in fully developed channel flow at low Reynolds number. J Fluid Mech 177:133–166
Kitaigorodskii SA, Donelan MA (1984) Wind-wave effects on gas transfer, In: Gas Transfer at the Water Surfaces, W. Brutseart and G.H. Jirka, Eds., Reidel: 147-170
Kjelleberg S, Stenstrom TA, Odham G (1979) Comparative study of different hydrophobic devices for sampling liquid surface films and adherent microorganisms. Mar Biol 53:21–25
Kline SJ, Reynolds WC, Schraub FA, Runstadler PW (1967) The structure of turbulent boundary layers. J. Fluid Mech 30: 741–773
Kolmogorov AN (1942) Equations of turbulent motion of an incompressible fluid. Izvestia, Academy of Sciences, USSR; Physics 6(1) & (2): 56-58
Kudryavtsev VN, Soloviev AV (1985) On parameterization of cool skin of the ocean. Izvestia, Atmos Ocean Phys 21(2):177–183
Kurata N (2012) Sea Surface Microlayer Microbial Observation System. MS Degree Thesis. Nova Southeastern University Oceanographic Center, Dania Beach, Florida, pp 45

Kurata N, Vella K, Soloviev A, Matt S, Tartar A, Shivji M, Perrie W. (2013)Surfactant-Associated Bacteria in the Near Surface Layer of the Ocean. Geophysical Research Abstracts 15, EGU2013-13199, EGU General Assembly, pp. 1

Lagerloef GSE, Swift CT, Le Vine DM (1995) Sea surface salinity: the next remote sensing challenge. Oceanography 8:44–50

Lesieur M (2008) Turbulence in fluids, Fourth Revised and Enlarged Edition. Springer pp 148

Lettau H (1969) Note on aerodynamic roughness-parameter estimation on the basis of roughness-element description. J Appl Meteorol 8:828–832

Liss PS (1983) Gas transfer, experiments, and geochemical implications. In: Liss PS, Slinn GN (eds) Air-sea exchange of gases and particles. D. Reidel, Dordrecht, pp 241–298

Liss PS, Duce RA (1997) Preface. In: Liss PS, Duce RA (eds) The sea surface and global change. Cambridge University Press, UK, pp XIII-XV

Liss PS, Watson AJ, Bock EJ, Jaene B, Asher WE, Frew NM, Hasse L, Korenowski GM, Merlivat L, Phillips LF, Schlüssel P, Woolf DK (1997) Report group 1—physical processes in the microlayer and the air-sea exchange of trace gases. In: Liss PS, Duce RA (eds) The sea surface and global change. Cambridge University Press, UK, pp 1–34

Liu WT, Businger JA (1975) Temperature profile in the molecular sublayer near the interface of fluid in turbulent motion. Geophys Res Lett 2:403–404

Longuet-Higgins MS (1992) Capillary rollers and bores. J Fluid Mech 240:659–679

Mammen TC, Bosse N von (1990) STEP – a temperature profiler for measuring the oceanic thermal boundary layer at the ocean-air interface. J Atmos Ocean Tech 7:312–322

Manton MJ (1973) On the attenuation of sea waves by rain. Geophys Fluid Dynam 5:249–260

Matt S, Soloviev A, Rhee S (2011) Modification of turbulence air-sea interface due to the presence of surfactants and implications for gas exchange. Part II: numerical simulations. In: Gas Transfer at Water Surfaces, Kyoto University Press, pp 299–312

McAlister ED, McLeish W (1969) Heat transfer in the top millimeter of the ocean. J Geophys Res 74:3408–3414

McLeish W, Putland GE (1975) Measurements of wind-driven flow profiles in the top millimeter of water. J Phys Oceanogr 5:516–518

Melville WK (1996) The role of surface-wave breaking in air-sea interaction. Ann Rev Fluid Mech 28:279–321

Le Méhauté Bernard, Tarang Khangaonkar (1990) Dynamic interaction of intense rain with water waves. J Phys Oceanogr 20:1805–1812

Minnett PJ (2003) Radiometric measurements of the sea-surface skin temperature – the competing roles of the diurnal thermocline and the cool skin. Int J Remote Sens 24(24):5033–5047

Minnett PJ, Knuteson RO, Best FA, Osborne BJ, Hanafin JA, Brown OB (2001) The Marine-Atmosphere Emitted Radiance Interferometer (M-AERI), a high-accuracy, sea-going infrared spectroradiometer. J Atmos Ocean Tech 18:994–1013

Motzfeld H (1937) Die turbulente Stromung an welligen Wanden. Z Angew Math Mech 17:193–212

Nightingale PD, Malin G, Law CS, Watson AJ, Liss PS, Liddicoat MI, Boutin J, Upstill-Goddard RC (2000) In situ evaluation of air-sea gas exchange parameterizations using novel conservative and volatile tracers. Glob Biogeochem Cy 14: 373-387

Okuda K (1982) Internal flow structure of short wind waves, Part I. The vorticity structure. J Oceanogr Soc Japan 38:28–42

Ostapoff F, Tarbeyev Y, Worthem S (1973) Heat flux and precipitation estimates from oceanographic observations. Science 180:960–962

Paulson CA, Lagerloef GSE (1993) Fresh surface lenses caused by heavy rain over the western Pacific warm pool during TOGA COARE. EOS Trans AGU 74(Suppl. to No. 43):125

Paulson CA, Simpson JJ (1981) The temperature difference across the cool skin of the ocean. J Geophys Res 86:11,044–11,054

Peng TH, Takahashi T, Broecker WS (1974) Surface radon measurements in the North Pacific Ocean station PAPA. J Geophys Res 79:1772–1780

Peng TH, Breocker WS, Mathieu GG, Li YH, Bainbrige EA (1979) Radon evasion rates in the Atlantic and Pacific Ocean as determined during the GEOSECS program. J Geophys Res 84:2471–2486

Phillips OM, Banner ML (1974) Wave breaking in the presence of wind drift and swell. J Fluid Mech 66:625–640
Phongikaroon S, Judd KP, Smith GB, Handler RA (2004) Thermal structure of clean and contaminated free-surfaces subject to an impinging gas jet. Exp Fluids 37(2):153–158
Plane JMC, Blough NV, Ehrhardt MG, Waters K, Zepp RG, Zika RG (1997) Report Group 3—Photochemistry in the sea-surface microlayer. In: Liss PS, Duce RA (eds) The sea surface and global change. Cambridge University Press, UK, pp 71–92
Poon Y-K, Tang S, Wu J (1992) Interactions between wind and waves. J Phys Oceanogr 22:977–987
Price JF, Weller RA, Pinkel R (1986) Diurnal cycling: observations and models of the upper ocean response to diurnal heating, cooling, and wind mixing. J Geophys Res 91:8411–8427
Prosperetti A, Oguz HN (1993) The impact of drops on liquid surfaces and the underwater noise of rain. Ann Rev Fluid Mech 25:577–602
Pruppacher HR, Klett JD (1978) Microphysics of clouds and precipitation. D. Reidel Publishing Company, Dordrecht, 714pp
Pumphrey HC, Elmore PA (1990) The entrainment of bubbles by drop impacts. J Fluid Mech 220:539–567
Robinson SK (1991) Coherent motions in the turbulent boundary layer. Ann Rev Fluid Mech 23:601–639. doi:10.1146/annurev.fl.23.010191.003125
Rodriguez F, Mesler RJ (1988) The penetration of drop-formed vortex rings into pools of liquid. J Colloid Interface Sci 121:121–129
Rao KN, Narasima R, Badri Narayanan M (1971) The "bursting" phenomenon in a turbulent boundary layer. J Fluid Mech 48:339–352
Riley JP, Skirrow G (1965) Chemical oceanography, Bd I. Academic Press, London, pp 712pp
Saunders PM (1967a) Shadowing on the ocean and the existence of the horizon. J. Geophys. Res. 72: 4643-4649
Saunders PM (1967b) The temperature at the ocean-air interface. J Atmos Sci 24:269–273
Saylor JR, Handler RA (1997) Gas transport across an air/water interface populated with capillary waves. Phys Fluids 9:2529–2541
Saylor JR, Flack KA, Schultz MP, Smith GB (2002) The correlation between surface temperature and subsurface velocity during evaporative convection. Exp Fluids 32: 570-579
Schlichting H (1979) Boundary-layer theory. McGraw-Hill, New York, pp 817pp
Schlüssel P, Emery WJ, Grassl H, Mammen TC (1990) On the bulk-skin temperature difference and its impact on satellite remote sensing of the sea surface temperature. J Geophys Res 95:13,341–13,356
Schlüssel P, Soloviev AV, Emery WJ (1997) Cool and freshwater skin of the ocean during rainfall. Bound.-Layer Meteor 95:82,437–82,472
Siscoe GL, Levin Z (1971) Interaction of water drops with surface waves. J Geophys Res 76:5112
Soloviev AV (1990) Coherent structure at the ocean surface in the convectively unstable conditions. Nature 346:157–160
Soloviev AV (2007) Coupled renewal model of ocean viscous sublayer, thermal skin effect and interfacial gas transfer velocity. J Marine Syst (Elsevier) 66:19–27
Soloviev AV (1992) Small-scale structure of the open ocean boundary layers. Dissertation for doctor of physical-mathematical sciences degree, Russian Academy of Sciences, Moscow (in Russian)
Soloviev A, Donelan M, Graber H, and Haus B (2007) An approach to estimation of near-surface turbulence and CO2 transfer velocity from remote sensing data. Journal of Marine Systems (Elsevier) 66: 182-194
Soloviev A, Donelan M, Graber HC, Haus B, Schlussel P (2007) An approach to estimation of near-surface turbulence and CO2 transfer velocity from remote sensing data. J. Marine Syst 66: 182–194
Soloviev A, Kurata N, Vella K, Tartar A, Matt S, Shivji M, Fujimura A, Perrie W (2012) Effect of surfactants on sea surface temperature and salinity. IEEE Geoscience and Remote Sensing Society Symposium (IGARSS 2012) July 22–27, 2012, Munich, Germany. Abstract only

Soloviev A, Lukas R (2010) Effects of bubbles and spray on air-sea exchange in hurricane conditions. Bound -Lay Meteorol 136:365–376
Soloviev A, Matt S, Gilman M, Hühnerfuss H, Haus B, Jeong D, Savelyev I, Donelan M (2011) Modification of turbulence at the air-sea interface due to the presence of surfactants and implications for gas exchange. Part I: laboratory experiment. In: Gas transfer at water surfaces. Kyoto University Press, pp 245–258
Soloviev A, Schlüssel P (1998) Comments on "air-sea gas transfer: mechanisms and parameterizations." J Phys Oceanogr 28:1643–1645
Soloviev AV, Schlüssel P (1996) Evolution of cool skin and direct air-sea gas transfer coefficient during daytime. Bound Layer Meteor 77:45–68
Soloviev AV, Schlüssel P (1994) Parameterization of the temperature difference across the cool skin of the ocean and of the air-ocean gas transfer on the basis of modelling surface renewal. J Phys Oceanogr 24:1339–1346
Soloviev AV, Vershinsky NV (1982) The vertical structure of the thin surface layer of the ocean under conditions of low wind speed. Deep-Sea Res 29(12A):1437–1449
Spangenberg WG, Rowland WR (1961) Convective circulation in water induced by evaporative cooling. Phys Fluids 4:743–750
Stephen H, Stephen T (eds) (1964) Solubilities of inorganic and organic compounds; 2: Ternary Systems, Part I. Pergamon Press, McMillian Company, NY, pp 944p
Stull RB, Kraus EB (1987) A transilient model of the upper ocean. J Geophys Res-Oceans 92:10,745–10,755
Thorpe SA (1985) Small-scale processes in the upper ocean boundary layer. Nature 318:519–522
Tsai W (2001) On the formation of the streaks on wind-driven water surfaces. Geophys Res Lett 28(20):3959–3962
Tsimplis M (1992) The effect of rain in calming the sea. J Phys Oceanogr 22:404–412
Tsimplis M, Thorpe SA (1989) Wave damping by rain. Nature 342:893–895
Turner JS (1973) Buoyancy effects in fluids. Cambridge Univ. Press, NY
Verdugo P, Alldredge AL, Azam F, Kirchman DL, Passow U, Santschi PH (2004) The oceanic gel phase: a bridge in the DOM-POM continuum. Mar Chem 92:67–85
Vladimirov VS (1976) Equations of mathematical physics. Nauka, Moscow (In Russian) 527 pp
Volkov YA, Soloviev AV (1986) On vertical thermal structure of near-surface layer of atmosphere above the ocean. Izvestiya: Atmos Ocean Phys 22(9):899–903
Volino RJ, Smith GB (1999) Use of simultaneous IR temperature measurements and DPIV to investigate thermal plumes in a thick layer cooled from above. Exp Fluids 27:70–78
Wanninkhof R, McGillis WR (1999) A cubic relationship between air-sea CO2 exchange and wind speed. Geophys Res Lett 26(134):1889–1892 (Check on pg 48)
Wanninkhof R, Hitchcock G, Wiseman W, Vargo G, Ortner P, Asher W, Ho D, Schlosser P, Dickson M-L, Anderson M, Masserini R, Fanning K, Zhang J-Z (1997) Gas exchange, dispersion, and biological productivity on the west Florida shelf: Results from a lagrangian tracer study. Geophys Res Lett 24: 1767-1770
Ward B, Minnett PJ (2001) An autonomous profiler for near surface temperature measurements. Gas transfer at water surfaces. In: Donelan MA, Drennan WM, Saltzmann ES, and Wanninkhof R (eds) American Geophys Union Monogr 127:167–172
Wu J (1975) Wind-induced drift current. J. Fluid Mech 68: 49-70
Woods JD (1980) Diurnal and seasonal variation of convection in the wind-mixed layer of the ocean. Q J Roy Meteor Soc 106:379–394
Woolf DK (1997) Bubbles and their role in air-sea gas exchange. In: The Sea Surface and Global Change. P.S. Liss and R.A. Duce, Eds., Cambridge University Press, UK: 173-205
Wurl O, Holmes M (2008) The gelatinous nature of the sea-surface microlayer. Marine Chem 110:89–97
Yakimov YL (1959) Why waves are extinguished by rain. Izvestiya: Sib. Akad. Nauk SSR 5: 125-126 (in Russian)
Yang Z, Tang S, Wu J (1997) An experimental study of rain effects on fine structures of wind waves, J Phys Oceanogr 27: 419–430

Yeh (1992) Vorticity generation at a fluid interface. In Breaking Waves, edited by M. Banner and R.H.J. Grimshaw, Springer-Verlag, New York: 257-265

Zaitsev YP (1971) Marine neustonology (translated from Russian). National Marine Fisheries Service, NOAA and National Science Foundation, National Technical Information Service, Springfield, Virginia, 207 pp

Zaitsev Y (1997) Neuston of seas and oceans. In: The Sea Surface and Global Change. P.S. Liss and R.A. Duce, Eds., Cambridge University Press, UK: 371-382

Zhang X, Harrison S (2004) A laboratory observation of the surface temperature and velocity distributions on a wavy and windy air-water interface. Physics of Fluids 16: L5-L8

Zhang Y, Zhang X (2012) Ocean haline skin layer and turbulent surface convections. J Geophys Res-Oceans 117, 10.1029/2011jc00746

Zhao D. and Toba Y (2001) Dependence of whitecap coverage on wind and wind-wave properties. J Oceanography 57: 603-616